

**EXPERIMENTAL AND NUMERICAL ANALYSIS OF SEMI-SOLID
CONSTITUTIVE BEHAVIOUR OF B206 AND A356 FOUNDRY ALLOYS**

by

Fariba Sheykhjabeti

M.Sc., Sharif University of Technology, 2009

B.Sc., Sharif University of Technology, 2007

A THESIS SUBMITTED IN PARTIAL FULFILLMENT OF
THE REQUIREMENTS FOR THE DEGREE OF

DOCTOR OF PHILOSOPHY

in

THE FACULTY OF GRADUATE AND POSTDOCTORAL STUDIES

(Materials Engineering)

THE UNIVERSITY OF BRITISH COLUMBIA

(Vancouver)

February 2018

© Fariba Sheykhjabeti, 2018

Abstract

Aluminum foundry alloys are used for a wide range of industrial applications. Hot tearing is often a challenging casting defect in aluminum alloys, occurring in the semi-solid state, which has a substantial impact on the quality of casting products. The constitutive response of the semi-solid material to deformation is crucial for controlling hot tear formation, and thus it is necessary to have a means of assessing a semi-solid's constitutive behaviour, and the role of microstructure in deforming this two-phase medium. The semi-solid tensile behaviour of two commercially used foundry aluminum alloys was experimentally characterized using a Gleeble thermo-mechanical test apparatus and numerically characterized using a multi-physics numerical model. First, thermo-mechanical testing was carried out on samples prepared by chill wedge-shaped casting. The test results indicated that at relatively high fraction solid ($f_s=0.95-1$), B206 has higher yield stress than A356. However, at lower fraction solids ($f_s<0.95$), A356 has been shown to have higher yield stress. The minimum fraction solid when the yield stress reaches very low values (almost zero), known as rigidity point, are shown to be 0.93 and 0.80 for B206 and A356, respectively. Second, the combined effects of deformation, fluid flow, and microstructure were studied using a multi-physics granular microstructure model. Using feedable and unfeedable microstructure models, the effect of feeding of the semi-solid pressure drop was studied. Unfeedable domains with different microstructures including equiaxed globular, equiaxed dendritic, and combined dendritic and eutectic were developed. Considering that lack of liquid feeding and semi-solid deformation are the well-known contributors to the hot tearing formation, the effect of feeding and mechanical deformation were studied and discussed. The model demonstrated that the microstructure type and the eutectic formation

also have a considerable effect on the liquid channels pressure drop and semi-solid bulk stress and strain, and consequently on hot tearing. Then, the obtained experimental and numerical results were used to assess the hot tearing susceptibility of A356 and B206. Both experimental and numerical results showed that B206 is more susceptible to hot tearing. However, hot tearing could occur in A356 as well if feeding is limited.

Lay Summary

Thermal and mechanical stress and solidification shrinkage cause some imperfections in the casting such as hot tearing. In order to predicate the hot tearing formation, the semi-solid behaviors of two commercial alloys were studied using experiments and computer aid simulations. First, metals were melted and poured into a wedge-shaped mold, then Gleeble machine was used to heat the sample up to the semi-solid temperate and pull them apart till the fracture. It was shown that the strength of the material is fraction solid and cooling rate dependent. Second, Abaqus software was used to predict the semi-solid respond to an applied deformation. It was shown that the shape of the solid part and distribution of the liquid part plays an important role in the pressure drop and strength of the semi-solid domain. The results of the project could be used to improve the casting process of the automotive part.

Preface

This dissertation presents original work that I have performed to study the semi-solid constitutive behaviour of aluminum foundry alloys. In performing this project, I was privileged to use a number significant pieces of work performed by others. Others work contribution that I drew on and my involvements include:

- I designed a wedge-shaped casting mould described in detail in *Chapter 4- Development of the Wedge-Shaped Chill Casting*
- I designed a new method for controlling the temperature of thermo-mechanical testing as shown in *Chapter 4 – Thermo-Mechanical Testing*
- A python code introduced by Dr. André Phillion was used and developed to create globular and dendritic and dendritic with eutectic microstructure of aluminum alloys.
- I developed numerical models which couple Abaqus/Standard and Abaqus/CFD to predict semi-solid respond to an applied deformation considering the pressure drop in the liquid channels and bulk semi-solid strain and stress.

Versions of chapters 5 and 6 were prepared in manuscript formats for submission and currently are under review by the co-authors. These manuscripts are listed below

- **F. Sheykhjbaeri**, A. Phillion. S. Cockcroft, “Experimental analysis of semi-solid constitutive behavior of A356 and B206 Aluminum foundry alloys”, Internal review.
- **F. Sheykhjbaeri**, A. Phillion. S. Cockcroft, “Numerical analysis of semi-solid constitutive behavior of A356 and B206 Aluminum foundry alloys”, Internal review.

The following is the list of the conference presentations:

1. **F. Sheykhjbaeri**, A. Phillion. S. Cockcroft, “A Coupled Fluid/Structure Simulation of Semi-Solid Deformation in an A356 Aluminum Alloy”, COM, 53rd Annual Conference of Metallurgists, 2014.
2. **F. Sheykhjbaeri**, A. Phillion. S. Cockcroft, “Multi-physics Meso-scale Modeling of Semi-solid Deformation of Aluminum Alloys”, Auto 21 conference, 2015.
3. A. Phillion, **F. Sheykhjaberi**, H. R. Zareie Rajani, S. L. Cockcroft, D. M. Maijer, “Granular Modelling of Solidification and Semi-solid Defect Formation”, 2016 TMS Annual Meeting & Exhibition

Table of Contents

Abstract.....	ii
Lay Summary	iv
Preface.....	v
Table of Contents	vii
List of Tables	x
List of Figures.....	xii
List of Symbols	xviii
List of Abbreviations	xix
Acknowledgements	xx
Dedication	xxi
Chapter 1: Introduction	1
1.1 Aluminum Casting Alloys	2
1.2 Casting Defects in Aluminum Alloys	3
1.3 Semi-solid Constitutive Behaviour	4
Chapter 2: Literature Review	7
2.1 Aluminum-Copper and Aluminum-Silicon Alloys.....	7
2.2 Mushy Zone Transitions	9
2.3 Hot Tearing	13
2.3.1 Effect of Eutectic Fraction on Hot Tearing.....	15
2.4 Semi-solid Constitutive Behaviour	16
2.4.1 Observed Behaviour	16
2.4.2 Constitutive Laws.....	17

2.4.3	Thermo-Mechanical Tests of Semi-Solid Constitutive Behaviour	19
2.4.4	Numerical Modeling	23
2.5	Summary	26
Chapter 3:	Scope and Objective.....	27
Chapter 4:	Experimental Methods	29
4.1	Development of the Wedge-shaped Chill Casting.....	29
4.2	Sample Preparation	31
4.2.1	Casting.....	31
4.2.2	Hot Isostatic Pressing	31
4.2.3	Sample Machining.....	32
4.3	Thermo-mechanical Testing	32
4.4	Microstructure Characterization	35
4.4.1	Optical Microscopy	35
4.4.2	X-Ray Microtomography	36
4.4.3	Fractography.....	37
4.4.4	Characterization of Micro Segregation	37
Chapter 5:	Description of the Semi-solid Multi-physics Meso-scale Model.....	39
5.1	Description of the Exploratory Model	40
5.2	Description of the Microstructure Model	44
Chapter 6:	Results and Discussion.....	57
6.1	Experimental Results	57
6.1.1	Characterization of the Microstructure Resulting from Directionally Solidifying B206 and A356	57

6.1.2	Characterization of the Semi-solid Constitutive Behavior Resulting from the Thermo-Mechanical Testing of B206 and A356	64
6.1.3	Discussion of Experimental Results and Comparison to Past Work	80
6.1.4	Experimentally-based Assessment of the Hot Tearing Sensitivity	83
6.2	Simulation Results	86
6.2.1	Exploratory Simulation Results	86
6.2.2	Microstructure Model Simulation Results	91
6.2.3	Discussion of the Numerical Results	116
6.2.4	Numerically-based Assessment of the Hot Tearing Sensitivity	127
6.3	Summary	130
Chapter 7: Conclusions and Future Work.....		132
7.1	Conclusions.....	133
7.2	Future Work	134
Bibliography		136
Appendices.....		146
Appendix A		146

List of Tables

Table 2.1 Typical chemical composition of B206 and A356 Al casting alloys [1, 5].....	8
Table 2.2 Typical mechanical properties of B206 and A356 Al casting alloys [1, 5].....	8
Table 4.1 Thermo-mechanical tensile test experimental conditions for B206 and A356 specimens, strain rate = 0.003 s^{-1}	34
Table 5.1 Elastic constants (GPa) and Poisson's ratios used for the exploratory model.....	42
Table 6.1 Yield stress and ductility of B206 samples and A356 samples tested at 570°C and 520°C	77
Table 6.2 HTS_{LG} values for B206 A356 based on Langlais and Gruzleski's theory for samples taken from the bottom, middle, and top of the wedges.....	84
Table 6.3 HTS_{CD} values for B206 A356 based on Clyne and Davies' Criterion for samples taken from the bottom, middle, and top of the wedges.....	85
Table 6.4 Summary of mesh independence study for liquid and solid domains	90
Table 6.5 Different microstructure model domains characteristics	91
Table 6.7 Comparison of the feedable and unfeedable globular B206 microstructure model results	118
Table 6.8 Comparison of the unfeedable globular and dendritic B206 microstructure model results	118
Table 6.9 Comparison of the unfeedable dendritic B206 and A356 microstructure model results	121
Table 6.10 Average liquid channel size and critical liquid pressure drop at different fraction solids	128

Table 6.11 Numerically obtained pressure drop for different microstructure model at different fraction solids.....	128
Table A.1 Gleeble test results of as-cast B206	146
Table A.2 Gleeble test results of as-cast A356	147
Table A.3 Gleeble test results of HIP B206.....	147
Table A.4 Gleeble test results of HIP A356	148

List of Figures

Figure 2.1 Semi-solid feeding mechanisms, along with representative microstructure [4]....	11
Figure 2.2 The effect of the presence of eutectic on interdendritic feeding, a) no eutectic, b) with eutectic [2]	12
Figure 2.3 Variation in the ductility as a function of temperature in the semi-solid regime [38].....	17
Figure 2.4 A comparison between tensile tests of semi-solid Al-2wt.%Cu alloys (continuous curves) and simulation results (dashed lines) from a 3D semi-solid granular model [67]	26
Figure 4.1 (a) Schematic illustration of the gating system and mold cavity and (b) Wedge casting parts and materials	30
Figure 4.2 (a) Wedge casting and the tensile test sample locations, showing the position of the bottom, middle, and top samples (b) Tensile specimen geometry (dim. are in mm).....	32
Figure 4.3 Gleeble testing procedure, consisting of four steps: rapid heating to 400°C, slow heating to the test temperature, holding, and isothermal tensile deformation represented by oscillations in the graph	34
Figure 5.1 Exploratory model domain consisting of two solid grains and one liquid channel. The size of the domain is $600\ \mu\text{m} \times 600\ \mu\text{m} \times 10\ \mu\text{m}$	41
Figure 5.2 Exploratory model meshed domain showing the boundary conditions and loads for (a) liquid channel and (b) solid grains	43
Figure 5.3 Evolution in fraction solid with temperature for B206 [15] & A356 [71]......	45
Figure 5.4 Schematic illustration of the Voronoi algorithm [72]	46
Figure 5.5 Equiaxed globular microstructure representing (a) Fully solid, (b) Semi-solid showing the liquid channels ($f_s=0.90$).....	47

Figure 5.6 Comparison of the cloverleaf grains and a circle having equivalent area. The variables R_d and P_d are indicated	48
Figure 5.7 Equiaxed dendritic microstructure for at (a) low, (b) moderate, and (c) high fraction solid showing the percolation phenomenon and the formation of isolated liquid pockets	48
Figure 5.8 Equiaxed dendritic and spherical eutectic microstructure showing isolated pockets ($f_s=0.90$)	49
Figure 5.9 (a) Temperature dependent and (b) fraction liquid dependent yield stresses for B206 [76], Al-1.6 wt.% Si, Al-12 wt.% Si [43].....	52
Figure 5.10 Feedable globular microstructure domain showing the boundary conditions and loads for (a) liquid channel and (b) solid grains	53
Figure 5.11 Unfeedable globular microstructure domain showing the boundary conditions and loads for (a) liquid channel and (b) solid grains	54
Figure 5.12 Microstructure domains for (a) Feedable globular, (b)Unfeedable globular, (c) Unfeedable dendritic, (d) Unfeedable dendritic and eutectic grains at $f_s=0.95$	55
Figure 6.1 Optical micrographs of B206 taken from the (I) bottom (CR=2.5 °C/s), (II) middle (CR=0.14 °C/s), and (III) top (CR=0.04 °C/s) of the wedge casting	60
Figure 6.2 Optical micrographs of A356 taken from the (I) bottom (CR=1.81°C/s), (II) middle (CR=0.12°C/s), and (III) top (CR=0.08 °C/s) of the wedge castings.....	61
Figure 6.3 Variation in the measured grain size for B206 as a function of distance from the chill	62
Figure 6.4 Variation in the measured SDAS for A356 as a function of distance from the chill	62

Figure 6.5 Transverse sections from the tomographic reconstruction of (a) B206 and (b) A356 specimens taken from the (I) bottom, (II) middle, and (III) top of the wedge castings	63
Figure 6.6 Example of engineering stress-strain curves of as-cast B206 alloy (a) tested at 500°C, 520°C, 540°C, 550°C, and 570°C, and (b) at stress lower than 1 MPa (for the samples taken from the bottom of the wedges)	65
Figure 6.7 Example of engineering stress-strain curves of as-cast A356 alloy (a) tested at 500°C, 520°C, 540°C, 550°C, 560°C, and 570°C, and (b) at stress lower than 3 MPa (for the samples taken from the bottom of the wedges)	66
Figure 6.8 Variation in yield stress with fraction solid for (a) B206 with different grain sizes (GS) and (b) A356 with different SDAS	68
Figure 6.9 Variation in ductility with fraction solid for (a) B206 with different grain sizes (GS) and (b) A356 with different SDAS	72
Figure 6.10 Stress-strain curves HIP and as-cast (a) B206 at 520°C and 540°C, and (a) A356 at 520°C and 560°C	74
Figure 6.11 Solute profiles of Cu in B206 in both as-cast and HIP conditions	76
Figure 6.12 SEM images of the fracture surface of as-cast A356 specimens (a) 500°C, (b) 540°C	78
Figure 6.13 SEM images of the fracture surface of as-cast B206 specimens (a) 540°C, (b) 570°C	79
Figure 6.14 Comparison of semi-solid yield stress for obtained from the Gleeble test and measured by Bolouri [54] and Ludwig [84] for B206	82
Figure 6.15 Comparison of semi-solid yield stress for obtained from the Gleeble test and measured by Nguyen [12] and Benke [85] for A356	82

Figure 6.16 Contour plots of a) the solid grains stress in x-direction in Pa and b) The liquid pressure in Pa, with tensile displacement horizontal and to the right	87
Figure 6.17 Contour plots of a) liquid velocity in the x-direction ($\mu\text{m/s}$), b) liquid velocity in the y-direction in ($\mu\text{m/s}$), c) solid grain shear stress in Pa with tensile displacement horizontal and to the right	88
Figure 6.18 Comparison between simulations results (square data points) and analytical solutions (solid line) for the pressure drop versus the channel width.....	90
Figure 6.19 Sections of the feedable microstructure model domains at (a) $f_s=0.85$, (b) $f_s=0.90$, (c) $f_s=0.95$, and (d) $f_s=0.98$	93
Figure 6.20 Maximum strain variation with the fraction solid in the feedable globular microstructure model	94
Figure 6.21 Contour plots of the liquid velocity in the y-direction in $\mu\text{m/s}$ for tensile deformation of the feedable B206 microstructure model at $f_s=0.95$ at $\epsilon=0$ (overall view of the domain), $\epsilon=\epsilon_{\text{max}}/10$, $\epsilon=\epsilon_{\text{max}}/2$ and the final state $\epsilon=\epsilon_{\text{max}}$. Subsections A, B, C, D, and E are taken from the top, center, bottom, right and left of the domain, respectively.	96
Figure 6.23 Contour plots of the stress in the x-direction in kPa for tensile deformation of the feedable B206 microstructure model at $f_s=0.95$ at $\epsilon=0$, $\epsilon=\epsilon_{\text{max}}/10$, $\epsilon=\epsilon_{\text{max}}/2$ and the final state $\epsilon=\epsilon_{\text{max}}$	98
Figure 6.24 Contour plots of the Von Mises stress in kPa for tensile deformation of the feedable B206 microstructure model at $f_s=0.95$ at $\epsilon=0$, $\epsilon=\epsilon_{\text{max}}/10$, $\epsilon=\epsilon_{\text{max}}/2$ and the final state $\epsilon=\epsilon_{\text{max}}$	99
Figure 6.25 Effect of strain and fraction solid on the pressure drop in the feedable B206 microstructure domains.....	100

Figure 6.26 Sections of the unfeedable granular B206 microstructure model domains at (a) $f_s=0.85$, (b) $f_s=0.90$, (c) $f_s=0.95$, and (d) $f_s=0.98$	103
Figure 6.27 Maximum strain variation with the fraction solid in the unfeedable globular microstructure model	103
Figure 6.28 Contour plots of the solid grains Von Mises stress in MPa for tensile deformation of the unfeedable globular B206 microstructure model at $f_s=0.95$, at $\epsilon=0$, $\epsilon=\epsilon_{max}/10$, $\epsilon=\epsilon_{max}/2$, and ϵ_{max}	105
Figure 6.29 Effect of strain and fraction solid on the average pressure drop in the unfeedable globular microstructure domains	106
Figure 6.30 Effect of strain and fraction solid on the stress-strain curves of the unfeedable globular microstructure domains	106
Figure 6.31 Sections of the unfeedable dendritic B206 microstructure model domains at (a) $f_s=0.85$, (b) $f_s=0.90$, (c) $f_s=0.95$, and (d) $f_s=0.98$	107
Figure 6.32 Maximum strain variation with the fraction solid in the unfeedable dendritic microstructure model	108
Figure 6.33 Contour plots of the solid grain Von Miss in MPa at $f_s=0.95$ of the unfeedable dendritic B206 microstructure model at $f_s=0.95$, at $\epsilon=0$, $\epsilon=\epsilon_{max}/10$, $\epsilon=\epsilon_{max}/2$, and ϵ_{max}	109
Figure 6.34 Effect of strain and fraction solid on the average pressure drop in the unfeedable dendritic microstructure domains	110
Figure 6.35 Effect of strain and fraction solid on the stress-strain curves of the unfeedable dendritic microstructure domains	111
Figure 6.36 Sections of the unfeedable A356 microstructure domains at (a) $f_s=0.85$, (b) $f_s=0.90$, (c) $f_s=0.95$, and (d) $f_s=0.98$	112

Figure 6.37 Maximum strain variation with the fraction solid in the unfeedable A356 microstructure model	112
Figure 6.38 Contour plots of the Von Miss in MPa for tensile deformation of the unfeedable A356 microstructure model at $f_s=0.95$ at $\epsilon=0$, $\epsilon=\epsilon_{max}/10$, $\epsilon=\epsilon_{max}/2$ and the final state $\epsilon=\epsilon_{max}$	114
Figure 6.39 Effect of strain and fraction solid on the average pressure drop in the unfeedable A356 microstructure model domains.....	115
Figure 6.40 Effect of strain and fraction solid on the stress-strain curves of the unfeedable A356 microstructure model domain	116
Figure 6.41 (a) Feedable globular B206 microstructure model and (b) Unfeedable globular B206 microstructure model sensitivity to the input yield stress and viscosity	123
Figure 6.42 Comparison of the model results with experiments for a) B206 and b) A356..	125
Figure 6.43 Comparison of semi-solid yield stress obtained from the unfeedable globular microstructure model and calculated by Sistaninia [66].....	127

List of Symbols

Latin Symbols	Description	Unit
A_0	Initial cross section	m^2
C_{max}	Maximum Cu concentration	-
C_{min}	Minimum Cu concentration	-
C_s	Cu concentration in a standard sample	-
\bar{d}	Average grain size	μm
E	Young's modulus	GPa
f_l	Faction liquid	-
f_p	Fraction porosity	-
f_s	Fraction solid	-
G	Shear modulus	GPa
h	Liquid channel size	μm
l_0	Initial gauge length	m
P_a	Atmospheric pressure	Pa
P_d	Perturbation	μm
Q	Creep activation energy	J/mol
R	Universal gas constant	J/mol. K
R_i	Rank number	-
R_d	Radius of the spherical nuclei	μm
T	Temperature	$^{\circ}C$
$t_{0.90}$	Time when $f_s=0.90$	s
$t_{0.99}$	Time when $f_s=0.99$	s
V	Liquid velocity	$\mu m/s$
Greek Symbols		
ε	Strain	-
$\dot{\varepsilon}$	Strain rate	s^{-1}
ε_{max}	Maximum strain	-
ΔP	Pressure drop	Pa
σ_s	Solid stress	MPa

List of Abbreviations

Symbol	Definition
CAE	Complete Abaqus Environment
CFD	Computational fluid dynamics
EDS	Energy Dispersive Spectroscopy
EDM	Electrical Discharge Machining
FSI	Fluid-Structure Interaction
HIP	Hot Isostatic Pressing
SDAS	Secondary Dendrite Arms Spacing
SEM	Scanning Electron Microscopy
WIRS	Weighed Interval Rank Sorting
XMT	X-ray Micro-Tomography

Acknowledgements

I would like to express my gratitude to the faculty and my fellow students in the department of materials engineering at UBC, who have motivated me to complete this project and demonstrated to me the importance of commitment and passion for my research. I would particularly like to single out my supervisor Dr. André Phillion, for his outstanding guidance, caring, patience, excellent cooperation and for all of the opportunities I was given to conduct my research.

In addition, I would like to thank my co-supervisor, Dr. Steve Cockcroft, for his valuable guidance. He definitely provided me an excellent atmosphere for doing research and tools that I needed to choose the right direction and successfully complete my dissertation. I would also like to thank Dr. Daan Maijer, for his support and encouragement during the past few years as well as his vigilant revision of my thesis and his comments and suggestions.

I would also like to thank my family for their wise counsel. Finally, there are my friends. We were not only able to support each other by deliberating over our problems and findings but also thankfully by talking about things other than just our projects.

Dedication

To the loving memory of my father

*To my mother, for offering the support and helping me to believe in
myself*

To my sister, my brothers, and my beautiful nieces

Chapter 1: Introduction

The automotive and aerospace manufacturers, along with others, are continually looking to increase the substitution of ferrous components with aluminum alloys in order to improve fuel efficiency and reduce emissions [1]. Casting is a widely used method of shaping aluminum alloys into industrial products. Al casting processes are categorized as ingot casting (wrought alloys) or shape casting (foundry alloys). In the first method, Al is cast into rectangular or cylindrical shapes, and then plastically deformed into sheets or extruded products. The forming process refines the alloy microstructure and eliminates casting defects; thus, the mechanical properties of wrought Al parts are enhanced. In the second method, molten Al is directly transformed into final or semi-final product by being cast into a near-net-shaped mould.

Shape casting provides the most cost-effective way for manufacturing aluminum components of complex geometry, however, defects including porosity, hot tearing, segregation, oxide films, and inclusions can reduce product yields and undermine mechanical performance [2]. In particular, the formation of hot tearing or solidification cracking limits the castability of high-strength alloys to simple geometries. Aluminum casting alloys are used in different components of the automotive industry, e.g. wheels, cylinder heads, brake components, suspension components, and engine blocks, amongst others.

Different shape casting methods, including permanent mould casting, sand casting, and foam casting, are used industrially. The wide range of operational conditions existing in casting processes generates, as a direct consequence, a variety of solidification microstructures and defects. Since these microstructural features (grain size, secondary dendrite arm spacing (SDAS), porosity, oxides, inclusions and hot tears) determine the final

mechanical properties of the material, a good understanding of the solidification microstructure evolution and defect formation mechanisms is very important.

1.1 Aluminum Casting Alloys

Al alloys have high strength to weight ratio, good ductility, good corrosion resistance, high electrical and thermal conductivity, and good surface appearance. Aluminum casting alloys are used for the production of a large variety of components in the automotive industry. The two major families of aluminum casting alloys are the 3XX series containing Si as the major alloying element, and the 2XX series containing Cu as the major alloying element. Within these families, noteworthy alloys include 206 and 356, respectively. The alloy 206 is a heat treatable high strength Al-Cu alloy that is difficult to cast due to its long freezing range but maintains high strength even at elevated temperatures. The alloy 356 is a heat treatable Al-Si alloy with good strength and fatigue resistance. It has been used for many years and is the predominant alloy for aluminum structural castings due to its high fluidity and excellent castability.

The majority of high-quality castings for automotive and aerospace applications use advanced versions of the 206 and 356 alloys. B206 is a recently developed [2] 206-variant for specialty aerospace applications with strict limits on Fe and Ti content; A356 is a mature variant of 356 with strict limits on the Fe and Zn content. These two alloys are very different from each other. In terms of microstructure, B206 exhibits a mainly primary phase structure with only ~5% eutectic, while a356 contains approximately 50% primary phase and 50% eutectic. In terms of mechanical properties, B206 has high strength but low corrosion resistance with moderate ductility, while A356 has moderate strength but good fatigue resistance and good ductility.

1.2 Casting Defects in Aluminum Alloys

Industrial Al alloy casting processes are not flawless, and there is always the possibility of imperfections and defects. In Al alloys, porosity and hot tearing are two of the main casting defects. The density of liquid aluminum is around 7% less than the density of the solid aluminum, which results in high solidification shrinkage. Porosity can be caused by the gas formation and solidification shrinkage. Hot tearing forms if the fluid flow is not adequate to compensate the shrinkage and deformation from thermal stresses and mechanical deformation. This phenomenon is explained in more details in this section.

Hot tearing, or solidification cracking, is the name given to a type of defect in castings that appears as cracks that form at temperatures above the solidus [2]. Such defects form near the end of the solidification process, leaving an intergranular fracture profile. Hot tearing is caused by the application of mechanical loading on semi-solid material that exhibits little ductility [3]. It may be exacerbated by a lack of metal flow to feed the shrinkage that is associated with solidification [4]. This defect has also been linked to high casting speeds, high thermal gradients, complex alloy chemistry, and variability in cooling conditions [5]. The alloy B206 is reported to be highly susceptible to hot tearing because of its high strength and long freezing range. In contrast, the alloy A356 is known to have a high resistance against hot tearing because its high eutectic content results in a short freezing range; the Si-rich liquid is also highly fluid and easily flows to counteract tensile deformation of the mushy zone [6].

1.3 Semi-solid Constitutive Behaviour

The occurrence of hot tearing is strongly related to semi-solid constitutive behaviour. The constitutive behaviour of semi-solids is complex since it depends on many factors like fraction solid, microstructure morphology, the viscosity of the liquid, and impurities. At low fraction solid, the material behaves like a fluid with a high viscosity. At high fraction solid, prior to the final solidification, continuous channels of liquid surround the solid grains. Depending on the permeability of the two-phase structure, the apparent ductility will vary considerably.

During casting, semi-solid Al is commonly subjected to tensile stresses due to temperature gradients and/or mechanical constraints that limit thermal contraction/expansion. In order to study the hot tearing phenomena, it is necessary to have a means of assessing semi-solid constitutive behaviour and the role of microstructure in accommodating strain [4]. This goal can be achieved using numerical modeling and/or experimental thermo-mechanical testing. Numerical models can provide much insight into semi-solid constitutive behaviour. At the macro-scale, the semi-solid material can be considered a single medium with average material properties expressed as a function of fraction solid or temperature. Unfortunately, such approaches are unable to describe any feeding or strain localization at the grain level, especially at grain boundaries that are most prone to hot tears formation, because the solid and liquid are treated as a single phase [7]. To focus on localization phenomena within the mushy zone, multi-scale models have been developed to simulate stress and strain at the macro-scale while modeling the grain structure at the micro-scale. In this approach, the semi-solid is modeled using separate solid and liquid elements. Such models have evolved from simple 2D simulations of the grain structure [8] to complex 3D simulations coupling inter-

dendritic liquid flow, solid deformation, and crack propagation [9]. Experiments can also be used to quantify the strength and ductility of semi-solid metallic alloys. There are two basic approaches for conducting semi-solid mechanical tests. The first consists of rapidly reheating standard tensile specimens in the as-cast state to a temperature within the semi-solid phase and then performing the deformation test. The second consists of cooling a small and well-designed casting from the liquid state prior to application of load [5].

The above models and experiments are interconnected. On one hand, the material properties required as input to the models are derived based on the deformation characteristics of semi-solid materials that must be obtained from experiments due to the complex interaction between microstructure constituents. On the other hand, models can be used to gain insight into material behaviour under conditions where experiments are difficult to perform and/or control. Experimental uncertainty can also be quantified based on the model predictions.

The aim of this study is to characterize the semi-solid constitutive behaviour of B206 and A356 alloys with particular emphasis on the effect of microstructure on hot tearing. To achieve the above goal, a two-stage characterization of casting structure and semi-solid constitutive behaviour is presented. The first stage uses a thermo-mechanical testing apparatus to measure semi-solid mechanical properties (yield stress and ductility) of B206 and A356 with different microstructure size. The second stage develops a multi-physics meso-scale model that captures differences in the microstructure between the two alloys in order to predict their semi-solid constitutive behaviour and ultimately to better understand why one is more prone to hot tearing than the other. The model simulates the two different

semi-solid mechanical tests; reheating as-cast samples from room temperature and casting from the liquid state.

This Ph.D. dissertation is structured as follows: Chapter 2 presents the literature review to describe the past experimental and numerical studies carried out to examine semi-solid constitutive behaviour and hot tearing in aluminum alloys with a focus on B206 and A356. Chapter 3 outlines the scope and objectives of this work. Chapter 4 and 5 describe the experimental and numerical methods used in this investigation. In Chapter 6, the results of the microstructure analysis, thermo-mechanical testing, and numerical simulation are presented, as well as a comparison between the experimentally-measured semi-solid mechanical properties and published data. The validation of the multi-physics numerical model using the experimental data also can be found in Chapter 6. Chapter 7 summarizes this study and provides ideas for future work.

Chapter 2: Literature Review

In Al-Cu and Al-Si foundry alloys, it is critical to prevent hot tearing since this defect can lead to component repair or rejection. This chapter provides an overview of previous research on the fundamentals of solidification, semi solid constitutive behaviour, and hot tearing. First, the material properties of B206 and A356 alloys are compared. Second, the transitions occurring within the mushy zone are presented in order to gain insight into the interplay between solid grains and liquid channels with increasing fraction solid. Then, a short introduction to hot tearing theory is provided. Finally, the prior research concerning mathematical models and experimental methods for investigating semi-solid constitutive behaviour is summarized.

2.1 Aluminum-Copper and Aluminum-Silicon Alloys

Al-Cu alloys are used widely in the automotive and aerospace industries. They exhibit a high strength-to-weight ratio [1], and good toughness over a range of temperatures [1]. Al-Cu casting alloys contain between 2-10% Cu, and thus they can be described as hypoeutectic. B206 is a relatively new Al-Cu alloy with chemical composition as shown in Table 2.1, and a microstructure consisting of ~5% eutectic phase [6]. This alloy is heat treatable and is generally treated to an over-aged (T7) condition in order to reduce its susceptibility to atmospheric corrosion [6]. Given the mechanical properties of B206 summarized in Table 2.2, the alloy is suitable for many applications including automotive suspension knuckles, suspension control arms, differential components, and aerospace and military castings [1].

Al-Si alloys are the most extensively used family of aluminum casting alloys, comprising 85-90% of the total aluminum shape cast parts produced for the transportation

industry. They have a good strength-to-weight ratio, superior castability and weldability, moderate corrosion resistance, and in particular, good fatigue and tensile properties, and low cost [1]. The main purpose of the Si addition is to improve the castability and fluidity of the alloy, enabling moulds of complex geometry to be filled during the casting process. A356 is a heat treatable hypoeutectic Al-Si alloy with a chemical composition as shown in Table 2.1, and a microstructure that contains approximately 50% primary phase, surrounded by approximately 50% of eutectic. The relevant mechanical properties are shown in Table 2.2. In both alloys, the mechanical properties depend on the solidification microstructure: grain size, SDAS, and porosity.

Alloy	Cu	Mg	Mn	Fe	Si	Zn	Ti
B206	4.2-5.0	0.15-0.35	0.2-0.5	<0.1	<0.05	<0.1	0.1
A356	<0.1	0.25-0.45	0.05-0.1	<0.2	6.5-7.5	<0.1	0.2

Table 2.1 Typical chemical composition of B206 and A356 Al casting alloys [1, 5]

Alloy	Heat treatment	Ultimate Tensile strength (MPa)	0.2% offset yield strength (MPa)	Elongation %	Fatigue limit (MPa)
B206	T7	445-460	370-390	9	-
A356	T6	262	193	6	60

Table 2.2 Typical mechanical properties of B206 and A356 Al casting alloys [1, 5]

Many studies have been carried out to investigate the solidification microstructure of A356 [10-13] and B206. Nguyen et al. [12] described the relationship between the solidification rates and microstructure characteristics of A356 aluminum alloy. Shao-Chun et al. [13] studied the effects of casting mould parameters such as thickness and preheat temperature on microstructure and mechanical behaviour of A356 aluminum alloy. Both studies showed that by increasing the cooling rate, the SDAS decreases noticeably and the

mechanical properties are improved. The increase in the properties was mainly attributed to the SDAS decrease. Talamantes-Silva et al. [14] studied the microstructure evolution in a directional solidified 206-type alloy, finding grain size and SDAS to decrease in regions that experienced higher cooling rates. Haghdadi et al. [15] studied the solidification kinetics of B206 as a function of the cooling rate in a range of 1 to 15 K/min. They showed that at a given temperature the variation of the fraction solid was affected by the cooling rate such that lower cooling rates were accompanied by larger fraction solid at a given temperature.

2.2 Mushy Zone Transitions

The process of solidification is complex due to the concomitant phenomena of phase stability, alloy constituent solubility, phase nucleation, heat transfer and mass transfer. The initiation and propagation of defects depend on the interplay between these phenomena in the mushy zone.

In the early stages of the solidification process, the solid grains nucleate and grow. Once a critical fraction solid is reached, the grains begin to interact with each other by bridging and then forming a solid skeleton. The “mushy zone” term is commonly applied to the whole transition from liquid to solid or vice-versa. This term is not completely correct, however, as the semi-solid mixture at low fraction solid, with grains freely suspended, is better described as a highly viscous liquid. A real mush will form only after the first contact between dendrites is achieved [16].

The formation of hot tears is closely linked to fluid flow in the interdendritic region. Campbell [2] summarized the four characteristic feeding mechanisms that can occur during solidification based on the permeability of the network. The changes in structure and

behaviour during each of these stages are outlined below and shown schematically in Figure 2.1 for the formation of equiaxed microstructure:

(1) Mass Feeding: At low fraction solid, the nucleated solid crystals float freely in the melt. The macroscopic behaviour is similar to a liquid [16], allowing bulk feeding to occur.

(2) Interdendritic Liquid Feeding: With increasing fraction solid, the grains begin to interact with each other, leading to a sharp decrease in melt flow. At this stage, the configuration of the grains does not allow bulk movement of liquid, yet the fraction solid is still low enough to allow for good feeding. The liquid forms a continuous film around each of the solid particles. Thus, the liquid has to flow through the solid network [16, 17].

(3) Interdendritic Separation: With further increase in fraction solid, the resistance to flow greatly increases - i.e. the permeability greatly decreases as the liquid channels become very small. Thus, no significant liquid can flow through the mush. The structure is sufficiently interlocked to transmit stresses in tension. Solidification defects, such as hot tears and porosity, can be initiated [18]

(4) Solid Feeding: At very high fraction solid, near the end of solidification, considerable dendrite interlocking occurs and the material develops significant strength. Since the grains are strongly interconnected, deformation occurs via high-temperature plasticity and creep. In this stage, liquid only exists in closed pockets [16, 17].

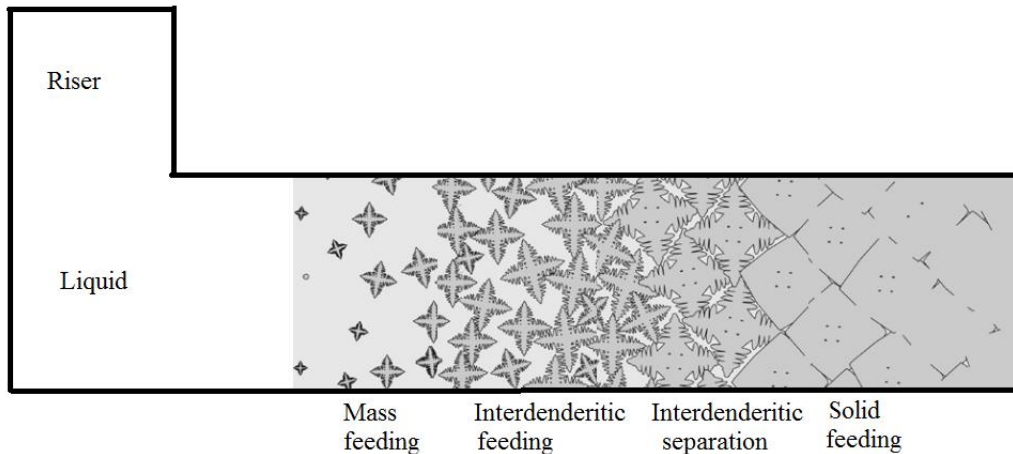


Figure 2.1 Semi-solid feeding mechanisms, along with representative microstructure [4]

From a mechanics approach, two important transitions occur during alloy solidification. The first occurs when the dendrite arms start to impinge on each other. At this *coherency temperature*, the solid grains are in contact but are still able to rotate and rearrange. The semi-solid is thus able to transfer shear stress [4]. The second occurs when the dendrites become interlocked. At this *rigidity temperature*, the solid grains become a dense and compact structure. Below this temperature, narrower liquid channels form and the melt permeability significantly decreases.

Through sustained research (e.g. [2, 19]), it has been demonstrated that microstructural features, and in particular the amount of eutectic, influences interdendritic feeding. During the solidification of alloys with minimal eutectic, like B206, the interdendritic channels become progressively narrower as the dendrites thicken and thus progressively more resistant to the flow of residual liquid.

Figure 2.2 shows schematic drawings of a columnar dendritic structure, without (a) and with (b) eutectic. In (a), it is very difficult for liquid to reach the root of the dendrite since the permeability of the mushy zone is quite low at high fraction solid. The propensity

for defects is thus increased. The presence of eutectic has a significant effect on permeability. In this case, as shown in (b) assuming equilibrium solidification, the eutectic front has moved ahead of the roots of dendrites, so that the interdendritic flow channels no longer gradually narrow but instead are truncated. Thus, the pressure gradient required to feed the solidification shrinkage is reduced. In binary alloys with significant eutectic, the required feeding pressure is even smaller because of the increased channel size at the point of the eutectic transformation. This makes such alloys easy to feed, avoiding the formation of hot tears [3]. In commercial alloys, like A356, the multiple solute additions result in multiple eutectic reactions during the latter stages of solidification. High cooling rates also extend the eutectic reaction temperature. In summary, this discussion has shown that the eutectic constituent morphology and the solidification range of the eutectic can affect feeding, and the occurrence of porosity formation, hot tearing, and segregation.

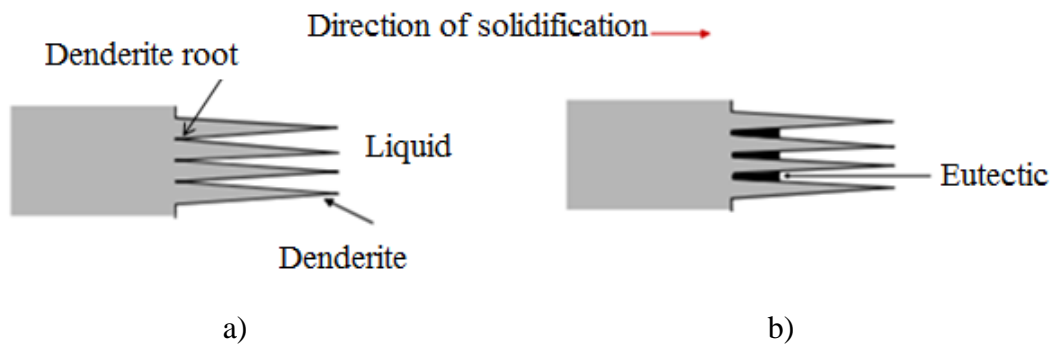


Figure 2.2 The effect of the presence of eutectic on interdendritic feeding, a) no eutectic, b) with eutectic [2]

2.3 Hot Tearing

Hot tearing is caused by a complex combination of thermo-mechanical and solidification phenomena. This defect is mainly related to the presence of tensile strains in conjunction with restricted liquid feeding in the mushy zone at high fraction solids [4]. These phenomena occur on two levels: microscopic (structure coherency and fluid flow) and macroscopic (stress, strain, or strain rate, and lack of mass feeding,).

There have been various theories suggested over the years to describe the occurrence and evolution of hot tears during the casting of aluminum and steels alloys [20-26]. Early studies concluded that hot tearing was related to the freezing range of the alloys. Singer and Jennings proposed that cracking occurs with high thermal contraction [23], while Pellini [24] proposed a strain-controlled mechanism. Based on such research, it was thought that pure metals and alloys of eutectic composition have low vulnerability to hot tearing. It is now known that although the freezing range is important, the microstructure developed during solidification should be considered as well [25]. Guven and Hunt [26] showed that hot tears initiate in the thin films of liquid between grains. The result of these studies indicates that hot tearing is controlled by the semi-solid mechanical properties (ductility and strength), as well as liquid feeding. During tensile deformation, both the solid grains and the liquid move toward areas of reduced pressure. Further deformation is possible if the ductility of the mush and fluid flow are sufficient to counteract tensile deformation. A hot tear will take place if the strain experienced by the semi-solid body is greater than its ductility [4]. Though the basic phenomena involved in hot tearing formation are well understood, there is still no agreement on exactly what controlling factors result in its formation.

Hot tearing criteria have traditionally been divided into two categories: mechanical (critical stress [27], strain [6], or strain rate [22, 28]) and non-mechanical (vulnerable temperature ranges, phase diagrams, and process parameters [4]). Presently, it is understood that both mechanical and non-mechanical effects must be taken into account to predict hot tear formation. Such combined criteria include the effects of solidification interval, feeding, microstructural features, stress, strain, and strain rate. Eskin et al. [5] have presented a comprehensive review on the various hot tearing criteria including the advantages and drawbacks of each. The most famous combination criterion is the one developed by Rappaz, Drezet, and Gremaud [29], based on the fact that the volumetric flow rate of the liquid must compensate not only solidification shrinkage but also deformation of the dendritic network. This criterion predicts the critical strain rate causing hot tearing for a given pressure drop. Monroe and Beckerman [20] modified the RDG criterion to use the critical liquid fraction at the critical pressure drop to determine the onset of hot tearing. This allowed for the separation of the porosity and hot tearing terms. While the combination criteria provide the best scenario for predicting hot tearing, there are still many unanswered questions related to the critical pressures and the link between hot tearing and porosity. A good criterion requires knowledge of both the permeability of the semi-solid for a given microstructure configuration and the semi-solid constitutive behaviour.

2.3.1 Effect of Eutectic Fraction on Hot Tearing

The eutectic phases play an important role in hot tearing. It has often been reported in the literature that a high fraction of eutectic results in a decrease in hot tearing susceptibility. Clyne et al. [30] explained that in alloys with large amounts of eutectic, sufficient liquid is present below the rigidity temperature to assist in the movement of the solid network and heal hot tears. In general, since hot tearing susceptibility is strongly linked to the solidification range, alloys with near-eutectic composition should be largely free of this defect. Bishop [31] demonstrated that the formation of eutectic is beneficial in Si-containing alloys because Si shows a volumetric expansion during solidification. The Si expansion decreases the solidification shrinkage and reduces the amount of stress applied to the solid network [32]. For A356, Li et al. [33] observed that a large amount of eutectic liquid present in the mushy zone prior to the final solidification enables good interdendritic feeding, resulting in a small hot tearing tendency. However, as highlighted by Sutton [34], healing of hot tears occurs only when the permeability is sufficient to enable liquid to flow into a newly formed void, otherwise residual liquid may rupture due to strain accumulation. D'Elia et al. [6] showed that hot tear initiation in B206 occurs prior to the formation of the eutectic. Based on micrographs of the fracture surfaces, it was suggested that the presence of eutectic on the hot tear surface was a result of eutectic-rich liquid drawn into the developing tears [6]. Small levels of impurities, which exist in the melt, can also form low-melting eutectics and increases the tendency of hot tearing. Puncreobutr et al. [35] showed that A319 alloys are susceptible to hot tearing despite having a high eutectic fraction because the Fe-rich intermetallics block the interdendritic channels. Lippold et al. [36] related the hot tearing tendency of Al-Mg alloys to Mg content, showing that high Mg resulted in the formation of a

low-melting eutectic liquid along the grain boundaries that was susceptible to hot tearing. In steel alloys, the formation of a P-rich eutectic along the grain boundaries was found to greatly increase hot tearing [34]. Furthermore, Shankar et al. showed [37] that hot tearing in stainless steel welds is caused by low-melting eutectics containing impurities (S, and P) and alloying elements (Ti, and Nb).

2.4 Semi-solid Constitutive Behaviour

2.4.1 Observed Behaviour

The mechanical behaviour of the mushy zone is complex. Measurements of ductility as a function of temperature in the semi-solid typically indicate a U-shaped curve as shown in Figure 2.3. As can be seen, solidifying alloys pass through a low-ductility range at high fraction solid. This curve can be interpreted by considering the four stages of solidification. During mass feeding, both the liquid and solid are free to move, allowing for much apparent ductility or viscous-like flow. In the interdendritic feeding stage, there is still considerable apparent ductility, which occurs by liquid flow through the solid network. As the permeability of the solid network decreases and the mush transitions to the interdendritic separation stage, the ductility also decreases since there is less liquid flow. When the permeability reaches zero, the ductility must also be close to zero; the solid cannot bear load due to the presence of the liquid films. Once large amounts of dendrite interlocking occur, the material develops considerable ductility.

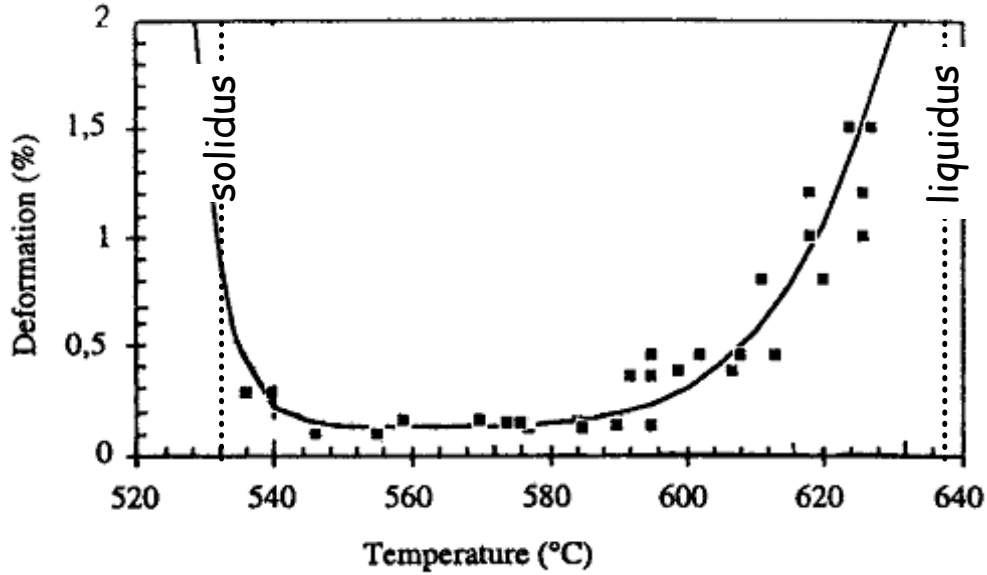


Figure 2.3 Variation in the ductility as a function of temperature in the semi-solid regime [38]

2.4.2 Constitutive Laws

The constitutive behaviour of a semi-solid in response to tensile stresses is crucial for developing predictive models of defect formation. In order to study the constitutive response of semi-solid alloys, it is first necessary to understand the mechanical response of the fully solid material. For aluminum alloys, the effects of strain hardening and strain rate sensitivity are usually included through the use of the extended Ludwik equation,

$$\sigma(T, \varepsilon, \dot{\varepsilon}) = K(T)\varepsilon^{n(T)}\dot{\varepsilon}^{m(T)} \quad (2.1)$$

where σ is the stress, ε is the plastic strain, $\dot{\varepsilon}$ is the strain rate, K is an alloy-dependent constant, T is the temperature, n is the strain hardening parameter and m is the strain rate sensitivity.

As aluminum alloys are known to have strain-rate dependent response at elevated temperatures, an alternative constitutive law can be developed based on an Zener Holloman formulation,

$$\dot{\epsilon} = A(\sigma_0) \exp\left(\frac{-Q}{RT}\right) \quad (2.2)$$

where $\dot{\epsilon}$ is the strain rate, σ_0 is the applied stress, Q is defined as the creep activation energy, A is constant which is material dependent, R is the universal gas constant and T is the temperature.

The approaches described by equations 2.1 and 2.2 have been successfully applied to aluminum alloys in the solid state. For example, Roy et. al [39] have critically reviewed the constitutive behaviour of the A356 alloy in the solid state. However, the mentioned equations have not been effective for predicting the semi-solid materials constitutive behavior. Some approaches for estimating the semi-solid constitutive behaviour have resulted in complex laws based on Equation (2.3) or (2.4), linking stress, strain, strain rate, and solidification microstructure. For example, Phillion [16] proposed a new constitutive expression for semi-solid AA5182 alloys by including microstructural features, such as grain size and porosity fraction to the Ludwik equation,

$$\sigma(f_s, f_p, \bar{d}) = K_p (f_s \sigma_s) (\epsilon)^{n(f_s, \bar{d})} \left(1 - \frac{f_p}{1-f_s}\right) \quad (2.3)$$

where f_s and f_p are the fraction solid and fraction porosity, respectively, K_p is a parameter related to the fraction porosity, σ_s is the solid flow stress, \bar{d} is the average grain size, and n is a temperature-dependent strain hardening parameter. The suggested relationship is valid at high fraction solid and considers the relevant effect of porosity and grain size on strain accumulation. Alternatively, Drezet and Eggeler [40] proposed to modify the exponential creep law through a simple scaling parameter, linked to fraction solid, to describe the semi-solid behaviour of the same alloy

$$\dot{\epsilon} = A\left(\frac{\sigma_0}{f_s(T)}\right) \exp\left(\frac{-Q}{RT}\right) \quad (2.4)$$

The justification behind using this type of creep law was that at high fraction solid the liquid exists as continuous films and isolated pockets between the solid. Any mechanical failure is then almost exclusively dependent on the solid as the liquid cannot bear the load. This law was further refined by Van Haaften et al. [41], who proposed that the load carrying area was proportional to $(1 - f_{LGB})$ in which f_{LGB} is the fraction of grain boundary area covered with liquid. A further refinement by Martin et al. [42] was to introduce an internal function to represent the partial cohesion of the mush. This function related the macroscopic strain rate to the average plastic strain rate of the solid accounting for the increase in dendrite interlocking with fraction solid.

While the above models were able to account for many of the semi-solid deformation phenomena, there show a number of limitations. First, the models are valid only at relatively high fraction solid where it is the liquid channels and not the liquid itself that affects properties. Second, the flow stress is not related to the liquid properties such as viscosity. Third, the effect of the eutectic constituent is ignored. In the case of alloys with significant amount of eutectic, it may be necessary to differentiate between each of the constituents in terms of material constants.

2.4.3 Thermo-Mechanical Tests of Semi-Solid Constitutive Behaviour

Tensile and/or compression tests of mechanical properties can be used to investigate the constitutive behaviour of semi-solid materials. There are two different options available to the researcher for performing semi-solid tensile tests [6]: reheating of as-cast samples to the test temperature (i.e. re-melting tests), and casting of a liquid metal followed by cooling to the test temperature (i.e. solidification tests). Semi-solid tensile tests have been widely used in aluminum alloys, as summarized in [6].

Re-melting tests: This kind of test consists of reheating as-cast test specimens and then applying a tensile or compression load to measure the stress-strain behaviour. Singer and Cottrell [43] designed a reliable apparatus for tensile testing at temperatures above the solidus. They performed a tensile test on the reheated samples inside a furnace and reported rigidity temperatures between 5-60 deg. above the solidus, depending on alloy composition. Recently, Gleeble thermomechanical simulators have been used to establish the semi-solid constitutive behaviour of different alloys [44, 45]. The significant advantage of the Gleeble apparatus is the use of Joule heat for rapid melting of the sample. In combination with modern strain–stress and temperature acquisition and control, this increases the accuracy and reliability of measured results and assures a complete retention of the as-cast structure during the testing. Both Van Haaften et al. [46] and Colley et al. [47] performed tensile tests on an AA5182 alloy at temperatures up to 580°C or 7% liquid and found that strain rate can significantly affect the semi-solid tensile properties. However, the stresses measured by Colley two to three times larger than those measured by Van Haaften. This difference can be related to differences in chemical composition and test sample geometry, as well as the experimental methodology. Phillion et al. [8] developed a two-thermocouple model to measure the tensile constitutive behaviour of semi-solid AA5182 alloy, and found that rigidity occurs at fraction solid of 0.95. They also showed good agreement between their results and Colley's study [47]. Fabrègue et al. [48] investigated the behaviour of semi-solid Al-2wt.%Si and AA6056 aluminum alloys, and found that hot tearing does not occur at fraction solids greater than 0.95. Other uses of the Gleeble for measuring semi-solid constitutive behaviour can be found in [50, 55-56]. The main challenges in using re-melting tests to measure semi-solid constitutive behaviour relate to maintaining the as-cast

microstructure during reheating, and to having accurate knowledge of the fraction liquid during testing. Furthermore, testing is only possible at high fraction solid. In alloys with high eutectic content, there can be large changes in the amount of liquid present with only small variations in temperature, and thus methods should be developed to carry out the test at relatively low fraction solids.

Solidification tests: It is also possible to measure the tensile properties of the semi-solid during solidification. Ackerman et al. [49] devised a system of two water-cooled cylinders that were plunged into a melt to initiate solidification and then separated after a certain shell thickness had formed to apply a tensile load. This apparatus was used to determine properties for both pure Al and Al-Mg alloys. The rigidity point was observed to be at fraction solid of ~ 0.95 . Mathier et al. [49] used an apparatus consisting of two concentric cylinders to solidify an Al-4.5wt.%Cu alloy while concurrently applying strain to the mushy zone. Using a fracture mechanics approach, a rigidity value of 0.96 was reported. Dahle et al. [50] measured the semi-solid strength in Al-4wt.%Cu alloy using a horizontal mold, and reported a rigidity value of 0.90. Mitchell et al. [51] experimentally observed the evolution of strain in several aluminum alloys during solidification in order to measure the strain required for damage localization, and reported values of ~ 0.0069 in AA6111, ~ 0.0123 for AA3104, and ~ 0.0021 for Al-0.5wt.%Cu.

The main challenge in using solidification tests is to measure semi-solid constitutive behaviour while accounting for interaction with the container or mold. This container must be carefully chosen in order to minimize chemical reactions with the liquid metal, and melt-container friction forces. Furthermore, control of heat transfer is critical to ensure that the test is performed either isothermally or at a known cooling rate. Fabrègue et al. [45] showed that,

the maximum stress is always lower in solidification tests as compared to re-melting tests. This difference was attributed to the presence of thicker liquid films in the solidification test.

Analysis of the literature has shown that thermo-mechanical testing has been fairly successful in determining the rigidity point and hot tearing susceptibility of aluminum alloys. However, it can be seen that semi-solid constitutive behaviour is highly dependent on temperature, strain rate, chemical composition and test apparatus [16, 45]. In addition, these experiments are largely limited to wrought alloys that have a low eutectic fraction and/or larger solidification range. On the other hand, for the alloys which have a relatively high eutectic amount, hot tearing defects can also appear in practical industrial production. Until now, there has been only a small amount of research performed on A356 alloys to measure semi-solid constitutive behaviour, and the results are not in a good agreement. A comparison of test results by Nguyen [52] and Benke [53] showed considerably different semi-solid yield stress variations for a given fraction solid. For example, the yield stress at a fraction solid of 0.8 was reported to be 2.1 and 0.1 by Nguyen [52] and Benke [53], respectively. So clearly, more research on semi-solid behaviour is needed for this industrially important Al alloy. Recently, Bolouri et al. [54] studied the semi-solid tensile behaviour of 206 alloys at different temperatures near-solidus, corresponding to the solid fractions between 1 and 0.95. But they mainly focused on the microstructure, fracture surface, and crack propagation mechanisms.

2.4.4 Numerical Modeling

The above phenomenological models treat the semi-solid material as a continuum with properties represented by volume-averaged quantities at the macro-scale [55] with regression-fitting to match experimental data. Modeling the semi-solid constitutive behaviour through this approach has always been a challenge for researchers as the large range of material properties in the mushy zone is problematic. In order to overcome the limits introduced by the volume averaged methods, and based on experiments highlighting the importance of the granular nature of solidifying alloys [56], meso-scale granular models have now been created, where the semi-solid material is modeled using separate solid and liquid elements. These models take into account macroscopic fields (stress and strain), as well as microstructural features (grain size and shape).

The first granular models simulated the behaviour of a large number of solid grains that were spherical and either rigid [57] or deformable [58]. These models considered the interactions between the grains due to solid-solid contact but neglected the influence of the surrounding liquid medium. Subsequent granular-type solidification and/or semi-solid deformation models utilized a “regular grains” arrangement for the modeling of ductility or liquid feeding within semi-solid zones. For example, Dijkstra et al. [59] assumed a regular arrangement of hexagonal solid grains surrounded by a liquid network in order to simulate semi-solid fluid flow. Lahaie et al. [60] considered the semi-solid body to consist of hexagonal solid grains surrounded by liquid films. The strength of the semi-solid was then modeled as a function of strain, solid fraction, and liquid film thickness.

In a regular arrangement of grains, all the solid grains solidify at the same rate, therefore they all coalesce together at the same time. In reality, however, the arrangement of

the grains is random and results in distribution of grain sizes. As first proposed by Mathier et al. [7], a regular arrangement of grains can be substituted by a model where a random set of nuclei created using the Voronoi diagram and polyhedrons represents solid grains.

Solidification within each grain is then simulated by taking into account a coalescence involvement close to the last stage of solidification. This model was improved by Vernède et al. [56, 61] to consider smoothed corners. From these simulations, the rigidity fraction solid of an Al-1wt.%Cu alloy cooled at 1 K/s was reported to be 0.97. Using a similar approach, Phillion et al. [8] predicted the mechanical behaviour of an equiaxed semi-solid Al-Mg alloy, AA5182, by taking into account the effect of microstructural features. This included solid fraction, porosity, and grain size. The liquid was considered as a solid with low elastic modulus, offering little resistance to stress. Because fluid flow was not included, this model was only valid at a high fraction solid. Using an alternative method based on discrete elements, Yuan et al. [62] simulated crystal rearrangement during solidification of Al-7wt.%Si alloy cooled at 0.7 K/s. They ignored the eutectic reaction and provided a physically based definition of dendrite coherency.

Even though the idea of randomly distributed grains provides considerable enhancements to one's capability to utilize a granular approach to model fluid flow, the 2-D geometry has an important restriction considering that the granular microstructures are intrinsically 3-D. In order to create a realistic numerical representation of the semi-solid, some researchers [63, 64] generated geometry for 3-D finite element (FE) simulations from X-ray micro-tomographic images of semi-solid Al-Cu. Zaragoci et al. [65] showed that during the tensile testing a maximum strain rate value of 0.1 s^{-1} is found in the liquid pockets, while stresses are quite heterogeneously distributed in the solid with a maximum value ~ 7

MPa. Most recently, Sistaninia et al. [66] developed a comprehensive 3-D hydro-mechanical granular model that computes the solidification of large mushy zones of Al-1wt.%Cu alloy cooled at a constant cooling rate of 1 K/s. The solidification model was then coupled with an intergranular feeding calculation, a deformation simulation, and a crack formation calculation within the intergranular liquid channels to predict hot tear formations and stress-strain behaviour in metallic alloys during solidification. Figure 2.4 shows a comparison between the simulated stress-strain predictions and the experimental results of Al-2wt.%Cu alloy at fraction solid of 0.92, 0.96 and 0.98. As can be seen, the simulations are a good match to the experimental data. Further increasing the fraction solid, the flow stress increases, however, the tensile elongation decreases significantly.

The above research outlines recent studies that have developed the concept of a granular model of solidification. The past research has focused on the semi-solid behaviour of Al wrought alloys that have low eutectic content and consequently, the eutectic is ignored. These models are clearly useful; comparisons of the modeling results and experimental data indicate that meso-scale granular models are successful in predicting stress and strain development during semi-solid deformation. Such knowledge can be used to determine the rigidity point of aluminum alloys [9]. However, as wrought alloys have a low eutectic fraction, the effect of the eutectic has been ignored.

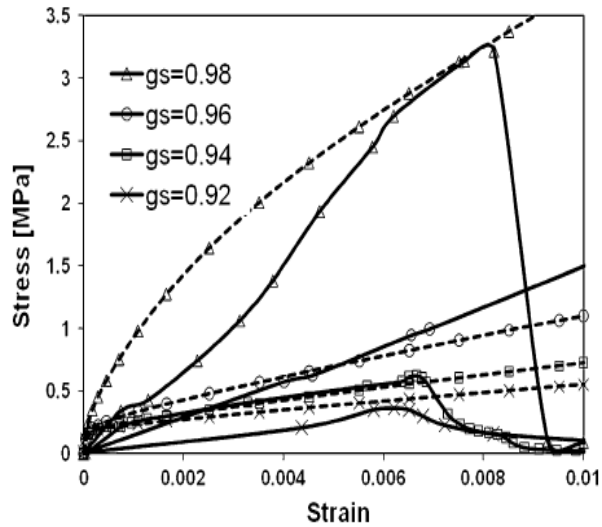


Figure 2.4 A comparison between tensile tests of semi-solid Al-2wt.%Cu alloys (continuous curves) and simulation results (dashed lines) from a 3D semi-solid granular model [67]

2.5 Summary

This chapter started by presenting an overview of the Al-Cu B206 and the Al-Si A356 alloys, and then discussed the stages of solidification in each alloy including the sequence of phase formation. Hot tearing was discussed in detail as an important casting defect, including relevant theories, models, and criteria. Liquid feeding and tensile deformation were shown to be the most important factors in hot tearing formation. The effect of the eutectic constituent on the hot tearing susceptibility of different alloys was reviewed, and it was concluded that there is no general agreement between the various theories available in the literature. Finally, the different methods for assessing the mechanical properties of the semi-solid metal were critically reviewed. It was shown that most of the numerical models and thermo-mechanical experiments have focused on the constitutive behaviour of wrought alloys with low eutectic content. In contrast, the semi-solid deformation behaviour of foundry aluminum alloys with high content of eutectic has not received much attention thus far.

Chapter 3: Scope and Objective

In Chapter 2, the subject of hot tearing was extensively reviewed from various perspectives, both numerically and experimentally. Although complex numerical models and experiments have been developed, there is still discussion in the literature regarding many relevant fundamental mechanisms. In terms of the role of the eutectic and microstructural features such as SDAS and grain size, there has been less definitive work since the experiments and theories produce inconsistent results. Most research has shown that materials with higher eutectic fraction have lower tendency to form hot tears [35, 38], however, some studies have shown that the presence of eutectic results in an increase in hot tearing susceptibility [26-28]. With all of this in mind, the semi-solid constitutive behaviour of Al alloys with different amounts of eutectic and different SDAS needs to be thoroughly investigated.

The first objective is to experimentally characterize the effects of the grain size and SDAS on the semi-solid constitutive behaviour of B206 and A356. The knowledge acquired is used to gain new fundamental insight into the role of microstructure on semi-solid deformation. Semi-solid deformation experiments are inherently difficult due to the existence of the liquid phase, and the dependency on chemical composition and thermal path. A looped thermocouple method is introduced and used to provide better control of the temperature at the center of the semi-solid sample.

The second objective is to develop a multi-physics meso-scale mathematical model based on granular methods for semi-solid B206 and A356. As presented in Chapter 2, the granular method for studying the semi-solid constitutive behaviour of wrought aluminum alloys with globular microstructures is well established. However, this type of modeling has

not yet been applied to foundry alloys, nor has the effect of the microstructure type and the formation of additional constituents including the eutectic has not been previously studied.

In order to achieve the objectives of the thesis, the following tasks were undertaken.

1. An apparatus was developed to cast a wedge geometry, The as-cast material via directional solidification then used as source material for the thermo-mechanical tests samples. Through the use of directional solidification, each sample had a uniform microstructure along its length, which was essential for understanding the effects of microstructure on semi-solid constitutive behaviour.

2. Grain size, SDAS and percentage porosity of B206 and A356 were characterized in the wedge casting. Semi-solid tensile tests were conducted to measure the constitutive behaviour of semi-solid alloys with low and high eutectic fraction. The effect of dendrite arm spacing and grain size on the semi-solid mechanical behaviour was quantified.

4. A multi-physics meso-scale mathematical model coupling fluid and deformation that incorporate semi-solid microstructure without and with significant eutectic fraction was developed for B206 and A356. The effects of microstructure type (globular or dendritic grains; with or without eutectic microconstituent) and liquid feedability on the semi-solid mechanical properties were studied.

5. Hot tearing susceptibility of A356 and B206 was compared from the experimental and numerical points of view.

Chapter 4: Experimental Methods

This chapter presents the experimental methodology used to study the microstructure and semi-solid constitutive behaviour of B206 and A356. First, a wedge-shaped steel mould with a water-cooled copper chill was designed and fabricated to directionally solidify the Al alloys. Subsequently, one-half of the wedges underwent the HIP process, in order to eliminate as-cast porosity. Then, tensile samples were extracted from the wedge castings, and Gleeble thermo-mechanical tests were performed to characterize the semi-solid constitutive behaviour at temperatures between 500°C and 570°C. Concurrently, the grain size, secondary dendrite arm spacing, and as-cast porosity were characterized by metallography, X-ray Microtomography (XMT), and scanning-electron microscopy. Finally, fractography was performed to characterize the fracture surface of the tensile tests.

4.1 Development of the Wedge-shaped Chill Casting

Thermo-mechanical testing of semi-solids requires tensile samples that have uniform microstructure along their length. In order to produce such specimens, a bottom-cooled wedge-shaped mould with directional solidification has been developed. The mould was made of plain carbon steel and housed the basin, sprue, gate, and wedge cavity plates. To create the tapered geometry, the thickness of the wedge was increased gradually from 12 mm at the bottom to 50 mm at the top. A water-cooled copper chill, placed at the bottom of the wedge, acted as the primary sink for removing heat from the liquid metal. A schematic of the gating system and mould cavity is shown in Figure 4.1.

In order to achieve directional solidification, the inner surfaces of the wedge plates were covered with HT-1 millboard¹ insulation having a very low thermal conductivity; the same material was used for the left and right sides of the wedge, as well as the interior surfaces of the gate. Due to the use of a copper chill, at the base, and HT-1 millboard on the sides, the cooling rate was highest at the bottom of the wedge and lowest at the top.

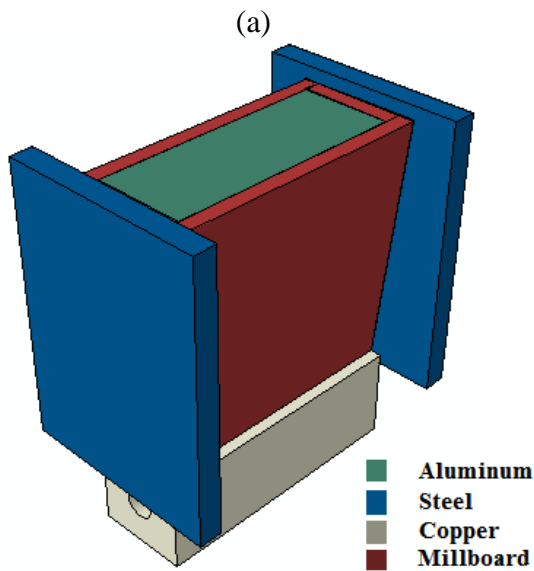
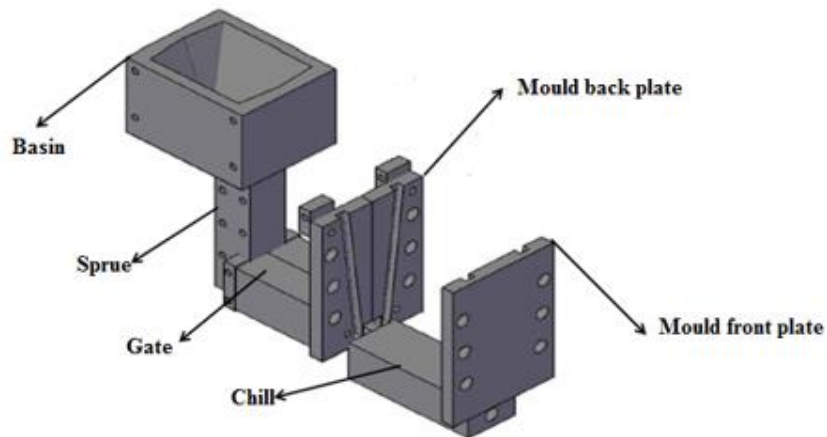


Figure 4.1 (a) Schematic illustration of the gating system and mold cavity and (b) Wedge casting parts and materials

¹ The material is a ceramic free composition of mineral wool and inert fillers which is supplied by Pyrotek [15]

4.2 Sample Preparation

4.2.1 Casting

B206 ingots and A356 wheel sections were used as feedstock to cast the wedges. First, the assembly was preheated to 300°C using embedded cartridge heaters. Concurrently, the millboard plates were baked in an induction furnace at 300°C for 45 minutes in order to reduce the dissolved water content and thus minimize off-gassing during casting. Then, the mould was assembled. Three Type-K thermocouples were placed within the mould cavity, at 5, 70, and 125 mm distances above the chill, to measure the cooling kinetics during casting. The temperatures were recorded every 0.2 seconds. Second, the Al alloys were melted in a graphite crucible using the induction furnace, providing superheat temperatures of 800°C and 700°C for B206 and A356, respectively. The hydrogen level was reduced by bubbling Ar gas through the melt for 5 minutes. However, the final content of hydrogen was not measured. Third, the molten metal was then poured into the basin, water flow started after pouring, and the melt allowed to solidify to form wedge castings. In total four B206 and four A356 wedges were cast.

4.2.2 Hot Isostatic Pressing

After casting, four wedges (2× B206 and 2× A356) were shipped to Bodycote, Inc., in order to undergo Hot Isostatic Pressing. The HIP process consists of a high-temperature cycle that is designed to remove as-cast porosity through the combined application of heat and isostatic pressure over about 3 hours. The exact processing conditions applied to the samples used in this study are proprietary and were not divulged by the supplier. Typical processing conditions for aluminum alloys are ~500°C, 100 MPa, and 3 hours.

4.2.3 Sample Machining

12 cylindrical tensile specimens were machined from each of the wedge-shaped castings, normal to the casting direction, to ensure that each contained identical microstructure in terms of grain size and secondary dendrite arm spacing. Electrical Discharge Machining (EDM) was used to take samples from the bottom, middle, and top of the wedges. Figure 4.2 (a) provides a schematic showing the location of each sample, while Figure 4.2 (b) shows the test specimen geometry with a central gauge region of 10 mm in length and 6 mm in diameter.

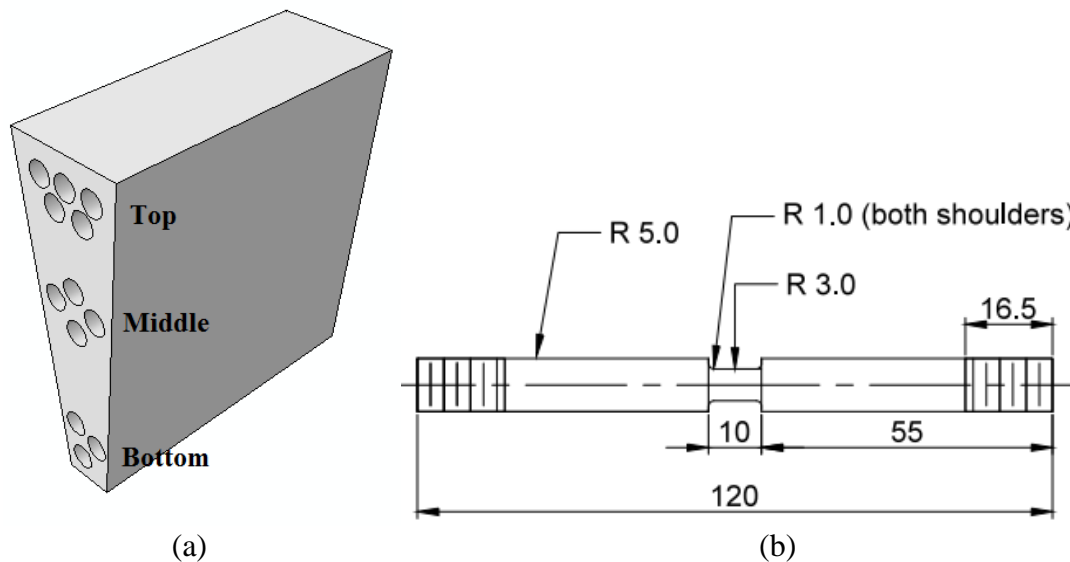


Figure 4.2 (a) Wedge casting and the tensile test sample locations, showing the position of the bottom, middle, and top samples (b) Tensile specimen geometry (dim. are in mm)

4.3 Thermo-mechanical Testing

The semi-solid deformation tests were performed using a Gleeble-3500 thermo-mechanical simulator. A series of experiments, listed in Table 4.1, were conducted between 500°C and 570°C at a strain rate of 0.003s⁻¹ on the as-cast and the HIP samples in order to characterize the semi-solid yield strength and ductility. To prevent oxidation, the Gleeble

chamber was first evacuated to 4e-1 torr and then filled with Ar gas. Within the Gleeble-3500, a current is passing through a specimen to heat it up by Joule effect. In these experiments, this enabled very fast heat rates thus minimizing microstructural changes via coarsening, but requires contact thermocouples welded directly to the sample.

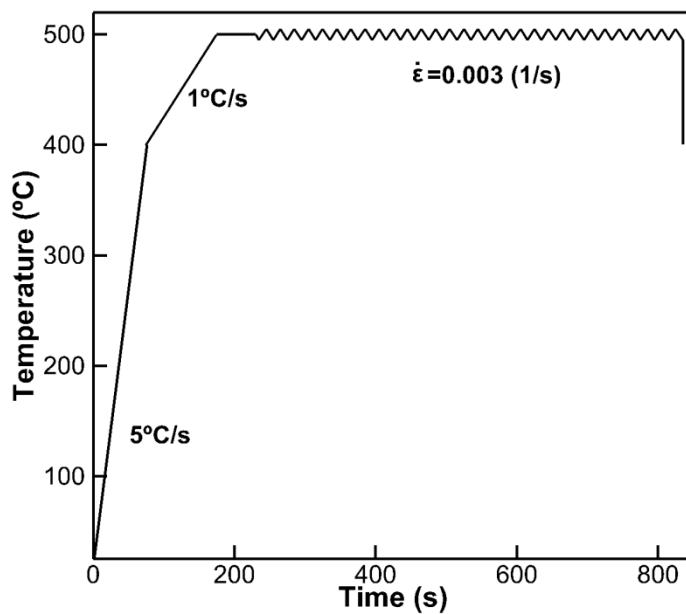
One of the main challenges in such tests conducted at temperatures within the semi-solid regime is weld detachment due to the formation of surface liquid. In this study, looped thermocouples were placed at the center of the gauge length, as shown in Figure 4.3 (a). This eliminated the issue of thermocouple detachment at temperatures within the semi-solid, making it possible to carry out the tests at higher temperatures/lower fraction solid. Additionally, small ceramic tubes were placed over the thermocouples to further protect against contact with hot metal during the semi-solid test (Figure 4.3 (a)). The deformation tests were conducted as follows. First, the samples were rapidly heated up to 400°C at a heating rate of 5°C/s. Second, the samples were slowly heated up to the test temperature at a heating rate of 1°C/s, and then held there for 20 (s). Lastly, the samples were deformed. Figure 4.3 (b) shows the thermal history of one test, where the sample was heated to 500°C/s.

Material	B206		A356	
Location of the samples within the wedge	As-cast and HIP material		As-cast and HIP material	
	Test temperature (°C)	f_s	Test temperature (°C)	f_s
Bottom/Middle/Top	500	1	500	1
	520	0.98	520	1
	540	0.95	540	0.97
			550	0.95
	550	0.93	560	0.90
	570	0.90	570	0.80

Table 4.1 Thermo-mechanical tensile test experimental conditions for B206 and A356 specimens, strain rate = 0.003 s⁻¹



(a)



(b)

Figure 4.3 Gleeble testing procedure, consisting of four steps: rapid heating to 400°C, slow heating to the test temperature, holding, and isothermal tensile deformation represented by oscillations in the graph

At low temperatures, ductility is measured during Gleeble testing by mounting an extensometer directly onto the specimens to measure the instantaneous diameter changes. However, at high temperatures, and especially within the semi-solid state, it is not possible to

use a contact extensometer. This is for two reasons. First, even the small loads applied by the extensometer can change the experimental results because of the low yield strength of semi-solids. Second, such devices are sensitive and could be damaged by liquid metal. Consequently, in this study, engineering stress and strain were reported instead of the real stress and strain values. Engineering stress and strain values were obtained directly from the Gleeble apparatus following Equation 4.1 and 4.2. These values were calculated by converting the measured force, F , and stroke, Δl , to engineering stress and strain by dividing them by the initial cross section area and initial gage length, respectively.

$$\sigma_e = \frac{F}{A_0} \quad (4.1)$$

$$\varepsilon_e = \frac{\Delta l}{l_0} \quad (4.2)$$

4.4 Microstructure Characterization

4.4.1 Optical Microscopy

12 metallographic specimens at distances from 5 to 135 mm from the chill were analyzed for each of B206 and A356 in order to measure and compare the SDAS and grain size, and to derive a mathematical correlation between SDAS and cooling rate. The metallographic samples were polished down to 1 μm using a standardized polishing method. The samples were etched, using 92 ml distilled water + 6 ml nitric acid + 2 ml hydrofluoric acid (commonly known as Kroll's Reagent) for 15 seconds before observation to reveal the microstructure. Metallographic images were then taken with a "Nikon1 EPIPHOT 300" optical microscope equipped with a digital camera. The images were then analyzed using the ImageJ software to measure the SDAS and grain size.

The SDAS was measured for the B206 and A356 alloy samples using the line intercept method. In this method, a line is drawn across the dendrite arms, the number of dendrite intersections counted, and then SDAS is obtained by dividing the line length by the number of intersections. The measurements were taken at different locations, and an average value and standard deviation were calculated. A total measurement area of at least 625 mm² was used for each specimen to ensure that an adequate number of SDAS were identified. Suitable locations were chosen where the secondary dendrite arms were clearly distinguishable. The grain size was measured as a function of the wedge height. This was carried out by counting the number of intercepts on three concentric circles. The average grain size was calculated as follows,

$$\text{Grain size} = \frac{\text{total length of the circles}}{\text{number of intersections}} \quad (4.3)$$

4.4.2 X-Ray Microtomography

In order to characterize porosity formation in the as-cast samples, X-Ray Microtomography (XMT) was used. High-resolution tomographic imaging, at a voxel resolution of ~ 5.9 μm, and scanning volume of 1675×1675×1997 was performed using a Nikon XT H 225 ST apparatus on both B206 and A356 tensile specimens taken from the bottom, middle, and top of the as-cast wedges. In total, 12 tomography scans were performed. The technique allowed for imaging of the internal porosity by first capturing a series of X-ray radiographs on a rotating specimen, and then reconstructing the resulting 3D image. Note that XMT was only carried out on the as-cast samples, since as shown by Phillion [16], the HIP process eliminates as-cast porosity in aluminum alloy samples.

4.4.3 Fractography

Fracture surfaces from the Gleeble test specimens were studied via scanning-electron microscopy (SEM), using a working distance of 27.7 mm and a beam energy of 20 kV. The specimen surfaces were examined at magnifications of 30 X, 80 X, and 200 X to determine the nature of each fracture surface.

4.4.4 Characterization of Micro Segregation

To determine the degree of segregation of Cu in both the as-cast and HIP materials, a scanning-electron microscopy-energy dispersive spectroscopy (SEM-EDS) quantitative compositional method known as weighted interval rank sort (WIRS) was carried out, on one as-cast and one HIP B206 sample, polished and carbon-coated, having similar SDAS. This method is applied in four stages. 1) The X-ray intensities are collected at random data points within B206 samples as well as a reference Cu sample; 2) The actual Cu composition at each data point is calculated, 3) The results are ranked by increasing Cu content, and 4) The corresponding fraction solid is assigned to each data point.

In the first step, EDS was carried out on 100 data points on as-cast and HIP B206 samples, using a sampling time of 50 s, and 50 μm grid spacing and x-ray intensities were measured at each point. In the second step, the NIST-DTSA-II software was used to quantify the EDS spectrums. Then, assuming that the Cu concentration of the standard sample is 100%, the X-ray intensities at each point were translated into Cu concentrations,

$$C_i = \frac{I_i}{I_s} C_s \quad (4.4)$$

where I_i and I_s refer to the measured X-ray intensity of the B206 sample, at location i , and the standard sample, respectively, C_s represents the Cu concentration in a pure Cu standard sample, and C_i represents the calculated Cu concentration at i . In the third step, the minimum Cu composition (C_{MIN}) and maximum Cu composition (C_{MAX}) as well as the uncertainty in Cu concentration (σ) were identified within the measurement data. With this information, a weighted Cu concentration was calculated at each point,

$$\bar{C}_i = \frac{C_i - C_{MIN}}{\sigma} \quad (4.5)$$

Consequently, \bar{C}_i varies between 0 and $\bar{C}_i = \frac{C_{MAX} - C_{MIN}}{\sigma}$. The \bar{C}_i values were then ranked in ascending order and given a rank number, R_i from 1 to the total number of points N , 100, in this case. In the last step, each ranked \bar{C}_i value was transferred to a fraction solid value. A fraction solid at location i , $f_s(i)$, was assigned based on the ratio of the rank number, R_i , to the total number of sampled points, N , as shown in Equation 4.6. Each sampled point was then assigned a corresponding fraction solid between 0 and 1.

$$f_s(i) = R_i / N \quad (4.6)$$

Chapter 5: Description of the Semi-solid Multi-physics Meso-scale Model

The research presented in Chapter 2, and other scholarly work, has provided much insight into the fundamentals of semi-solid constitutive behaviour and hot tearing of wrought Al alloys with globular primary microstructure. The most recent models, termed granular solidification models [56, 68], have been shown to reproduce experimentally-measured semi-solid yield stresses and strains. However, these models have not yet been applied to foundry alloys, which have a more complex solidification microstructure. As a result, for application to shape casting, other relevant features must be included. In this study, the focus is on characterizing the effect of primary grain shape (globular or dendritic) and the presence of the eutectic on the semi-solid constitutive behaviour of aluminum alloys A356 and B206. As many commercially relevant aluminum foundry alloys have a dendritic microstructure and a significant eutectic fraction, it seems essential to introduce this complexity into the simulations in order to improve understanding of semi-solid deformation in foundry alloys. The microstructure morphology and the evolution of the eutectic have a strong effect on solidification defects, especially hot tearing, microporosity, and intermetallics.

Granular solidification models fall into a subset of multi-physics modelling approaches known as fluid/structure interactions (FSI) where fluid flow affects compliant structures, which in turn affect the fluid flow. The commercial software package, Abaqus, allows for FSI using a partitioned approach whereby the structural (Abaqus/Standard) and fluid (Abaqus/Computational Fluid Dynamics (CFD) equations are solved independently, and the interfacial loads and boundary conditions are exchanged after a converged increment is achieved. In this approach, displacements and velocities are transferred to Abaqus/CFD

from Abaqus/Standard, while the pressure is transferred from Abaqus/CFD to Abaqus/Standard. These serve as the necessary boundary conditions at the FSI interface.

Two sets of simulations were developed and studied in this research. The first set – termed the *exploratory* model – is a geometrically simple model that was used to understand fluid/structure interaction within a mathematical model, and to demonstrate the feasibility of semi-solid multi-physics meso-scale simulation within Abaqus. The second set – termed *microstructure* model – simulates directly semi-solid deformation at the scale of the microstructure in aluminum foundry alloys. The microstructure model simulations were performed using two different types of fluid boundary conditions, (i) where flow is allowed, thus simulating the shape casting process and (ii) where flow is restricted, thus simulating Gleeble thermo-mechanical testing.

5.1 Description of the Exploratory Model

A series of simulations on geometrically simple domains was carried out to explore the ability of the FSI implementation within Abaqus to model semi-solid deformations, and to study the effect of liquid channel size on flow behaviour during mechanical deformation of the semi-solid. As can be seen in Figure 5.1 (a), the geometry contains two simple rectangular grains and one liquid channel. Physically, this corresponds to the region between two columnar grains.

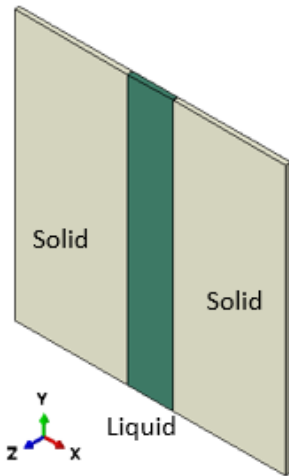


Figure 5.1 Exploratory model domain consisting of two solid grains and one liquid channel. The size of the domain is $600 \mu\text{m} \times 600 \mu\text{m} \times 10 \mu\text{m}$

Model Implementation: The two solid grains and the intergranular liquid channel were created using Abaqus Complete Abaqus Environment (CAE). The mechanical and fluid simulations were performed using Abaqus/Standard and Abaqus/CFD, respectively. Deformation of the solid grains was simulated using the standard non-linear dynamic-implicit integration method assuming an elastic-fully plastic constitutive behaviour. Flow in the liquid was assumed to be laminar and incompressible, with a constant viscosity. Note that although this was a 2D simulation, a 3D geometry was necessary in order to perform CFD simulations within Abaqus. For this reason, the 2D domain was extruded by $10 \mu\text{m}$ in the thickness direction, as can be seen in Figure 5.1.

Material Properties: The input properties required for the liquid phase were density and viscosity; these were assumed to be 2500 kg/m^3 and 0.0014 Pa sec , respectively [69]. The input properties required for the solid phase were the elastic modulus, Poisson's ratio, and yield stress. Although polycrystalline aluminum is known to have isotropic elastic materials constants, anisotropic properties were applied, as shown in Table 5.1. This

formulation was used in order to minimize displacements and strains in the z -direction, making it possible to perform a 2D FSI simulation using 3D geometry. Specifically, the elastic modulus was set to identical (and realistic) values in the x - and y - directions but set to be very large in the z -direction. Concurrently, the corresponding Poisson's ratios were adjusted. Finally, for this exploratory model, the yield stress of the solid grains was set to 8 MPa.

Material	E_x	E_y	E_z	G_{xy}	G_{xz}	G_{yz}	ν_{xy}	ν_{xz}	ν_{yz}
Aluminum	50.0	50.0	5.0×10^5	18.7	2.5×10^5	2.5×10^5	0.33	0.0	0.0

Table 5.1 Elastic constants (GPa) and Poisson's ratios used for the exploratory model

Boundary Conditions: The model boundary conditions were chosen in such a way that the 3D model retains the expected characteristics of a 2D simulation. For the solid grains, the bottom side and the left side were fixed in the y - and x - directions, respectively, while the top side was free to move in all directions. For the liquid, a constant static pressure (zero gage pressure) was imposed on the top surface. Further, the bottom surface was constrained to not move in the y -direction but was allowed to translate freely along the x -direction. The y -component of velocity at the bottom was also set to zero. Finally, in order to keep the out-of-plane stress and strain zero, the velocity of the liquid in the z -direction was also set to zero. The applied boundary conditions on the meshed exploratory model domain are shown in Figure 5.2. The term FSI in this figure identifies the surfaces where the solid displacements and velocities and fluid pressure were exchanged, and vice-versa.

Model Mesh and Mesh Sensitivity: Quadratic hexahedral (C3D20) solid elements and linear hexahedral (FC3D8) fluid elements were used to mesh the solid and liquid domains respectively. Due to the complexity of the simulation, the results will be sensitive to mesh size. A mesh sensitivity test with five cases using elements between 40 and 5 μm in length was conducted. The results will be presented in Chapter 6.

Applied Loads: To deform the model, a velocity boundary condition was applied to the right side of the domain, in the x -direction, at a strain rate of 0.001 s^{-1} . The applied deformation on the solid grain will induce flow in the liquid channel. According to Darcy's law, the fluid flow rate is proportional to a pressure difference resulting from deformation of the domain. In Chapter 6, the predicted flow rates will be compared against the corresponding Darcy's law predictions for different liquid channel thicknesses from 20 to 200 μm .

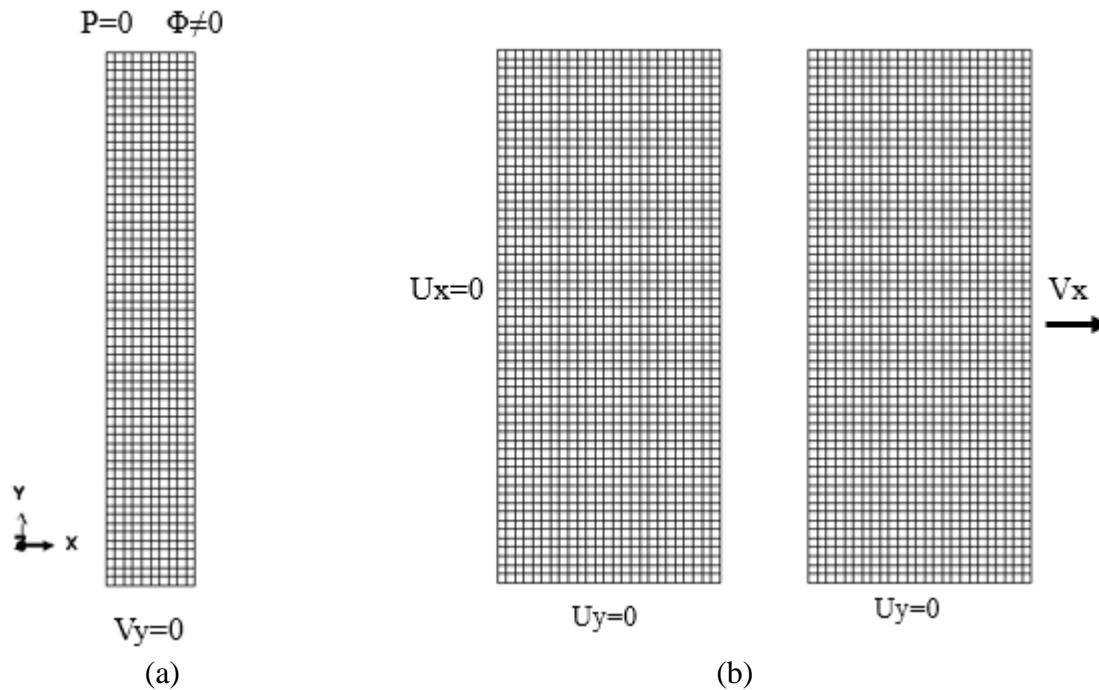


Figure 5.2 Exploratory model meshed domain showing the boundary conditions and loads for (a) liquid channel and (b) solid grains

5.2 Description of the Microstructure Model

The meso-scale model to directly simulate semi-solid deformation at the scale of the microstructure in aluminum foundry alloys was developed to study and predict the semi-solid behaviour of B206 with relatively low eutectic fraction of less than 5%, and A356 with relatively high eutectic value of around 50%. Figure 5.3 shows the evolution of fraction solid versus temperature for both alloys. The liquidus temperatures of B206 and A356 are 616°C and 642°C, respectively. The solidus temperatures of B206 and A356 are 505°C and 533°C, respectively. It can be seen that B206 has large solidification range of more than 100°C, making it greatly susceptible to hot tearing.

The 2D microstructure model that forms the basis for multi-physics simulations of semi-solid deformation in foundry alloys is based on the granular method for semi-solids [61] and extends earlier work [70] to consider different factors which affect pressure drop in liquid channels and to include dendritic microstructure and eutectic grains within an isothermal representative volume element. Thus, various model domains were created including ones consisting of only primary phase with globular and dendritic microstructures, and domains with both primary and eutectic microconstituents. As the focus is on studying hot tearing susceptibility, the simulations focused on the high fraction solid (0.85-0.98) regime.

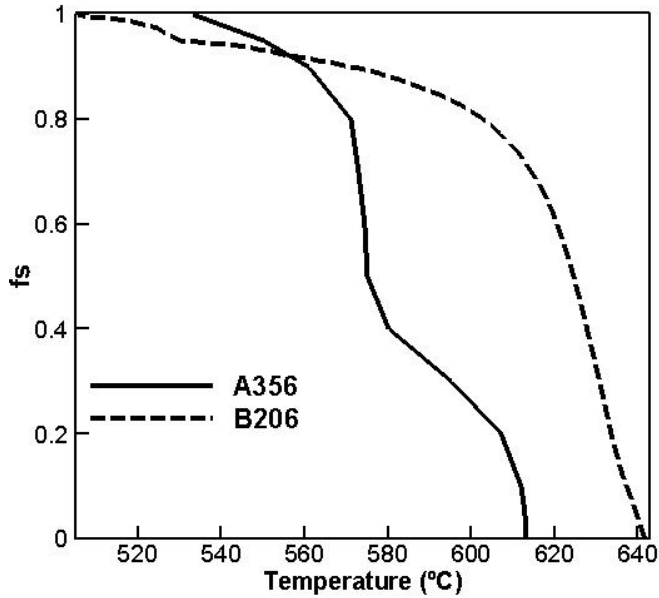


Figure 5.3 Evolution in fraction solid with temperature for B206 [15] & A356 [71].

Globular Microstructure: The numerical algorithm developed by Phillion [16] was used as the basis for creating equiaxed-globular microstructure. This microstructure was generated from a Voronoi tessellation or nearest-neighbour diagram that utilizes a set of randomly distributed points (seeds) to partition a representative volume element (RVE) into regions, i.e., Voronoi cells, one per point [72]. As shown by Vernède et al. [61], such a structure approximates the grain shape of equiaxed-globular grains. Hence, in this microstructure model, polygons represent two-dimensional grains and lines represent grain boundaries as shown by the schematic in Figure 5.4. The number of seed points represents the grain density, N_g . This is a model input, resulting in an average grain size given by

$$\bar{d} = 2(N_g \pi)^{-1/2} \quad (5.1)$$

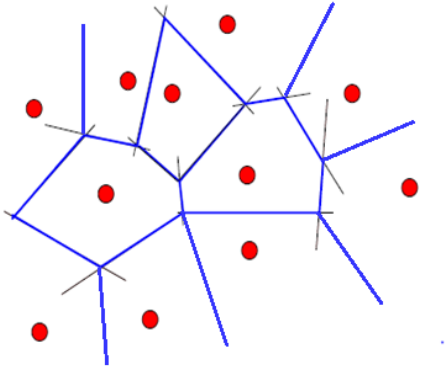


Figure 5.4 Schematic illustration of the Voronoi algorithm [72]

The model geometry, a subset of which is shown in Figure 5.5 (a), represents a fully solidified microstructure based on a Voronoi diagram. To create a semi-solid structure, the Voronoi cells are reduced in size; the resulting additional material is considered to be liquid as shown in Figure 5.5 (b). Each grain is reduced in size independently of the others by moving the coordinates of each vertex towards the nucleation point until the area of this new grain relative to the area of the Voronoi region is equal to the fraction solid of interest. The resulting geometry consists of a random configuration of grains fully surrounded by continuous films of liquid. The channels between the grains vary in thickness depending on the size of the grains, and the distance between the grain nuclei. It should be noted that the corners of grains created by the Voronoi diagram are sharp. Previous studies [16, 56] have introduced a model based on solute flux and Gibbs-Thomson theory to round the sharp corner. However, that proved to be too complex for the microstructure model simulations. In this research, instead, a curve of 5 μm radius was applied to round each corner.

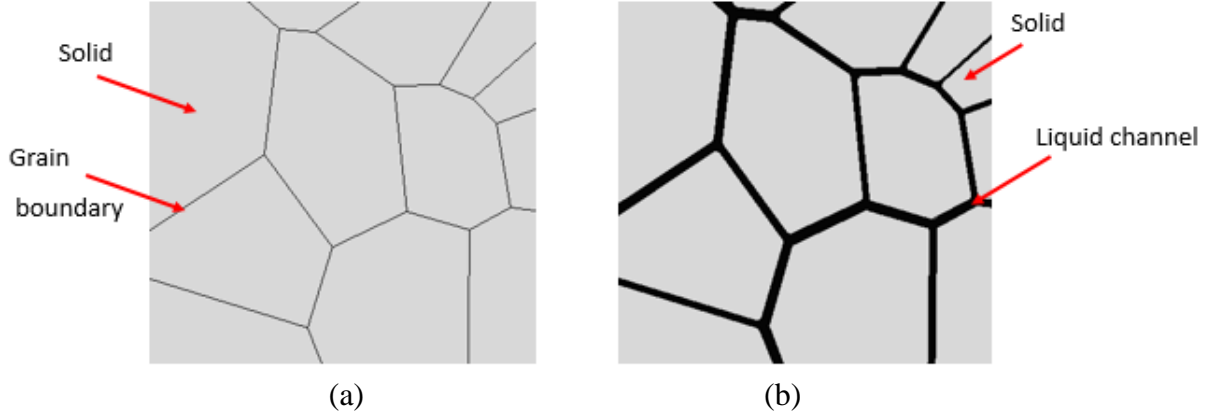


Figure 5.5 Equiaxed globular microstructure representing (a) Fully solid, (b) Semi-solid showing the liquid channels ($f_s=0.90$)

Dendritic microstructure: The equiaxed-dendritic model builds on the globular model by adding grains having four primary arms to mimic the Al FCC crystal structure in 2D. This geometry was created as follows. First, following research by Bayani et al. [73], dendrites were approximated as a cloverleaf shape,

$$r = R_d + P_d \cos(4(\theta + \theta_0)) \quad (5.2)$$

where R_d represents the radius of spherical nuclei, P_d represents a perturbation, and θ_0 represents the angle between the fluid flow and primary arm during the solidification. The shape was created using the Abaqus/Sketcher tool with $R_d=30 \mu\text{m}$, $P_d=10 \mu\text{m}$ and $\theta_0=0^\circ$. Figure 5.6 compares a cloverleaf shape to a circle having equivalent area. Second, a Voronoi diagram was created following the method described in the *globular microstructure* section. Third, each polygonal grain was replaced by the cloverleaf shaped grains. The grains were scaled based on the initial polygonal grains, and θ_0 was given a random value between 0 to 45° at each nucleation site. Finally, the entire set of solid grains was cut from a fully solid rectangular domain; the remaining material represents the liquid phase.

As can be seen in Figure 5.7 (a), when the fraction solid is relatively low, the resulting model geometry consists of solid grains surrounded by continuous liquid channels. As the fraction solid is increased, the dendritic arms first impinge on each other, Figure 5.7 (b), and then finally strongly interact resulting in the formation of many discrete liquid pockets, Figure 5.7 (c). This represents the percolation phenomenon that plays a major role in assessing hot tearing susceptibility [5].

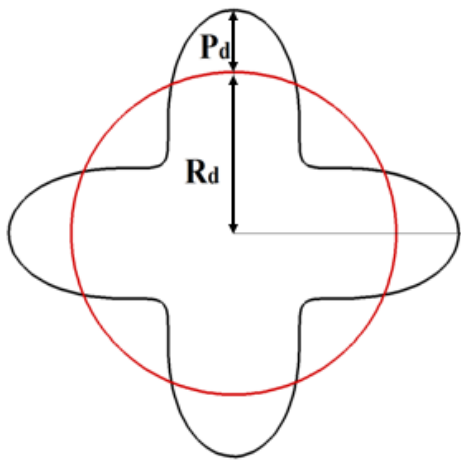


Figure 5.6 Comparison of the cloverleaf grains and a circle having equivalent area. The variables R_d and P_d are indicated

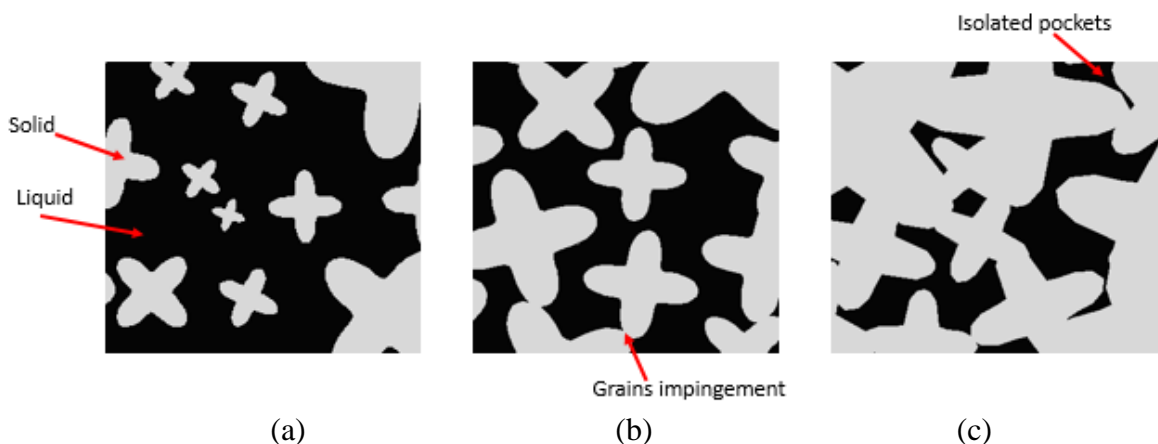


Figure 5.7 Equiaxed dendritic microstructure for at (a) low, (b) moderate, and (c) high fraction solid showing the percolation phenomenon and the formation of isolated liquid pockets

Eutectic microstructure: In the case of A356, eutectic grains were also added in order to properly simulate the observed microstructure. For this geometry, it was assumed that the initial solidification consists of primary grains having a dendritic (cloverleaf) morphology. Above a fraction solid of 0.5, the remaining liquid solidifies as eutectic assuming non-equilibrium solidification [74]. Eutectic is added to the model by adding circular grains to surround each primary grain. Thus, as soon as the temperature reaches the eutectic temperature, the primary phase stops growing and the eutectic grains nucleate. They then grow until the end of solidification. The resulting solid microstructure displays an unevenly distributed structure consisting of primary dendritic grains and eutectic of different sizes. It can be seen in Figure 5.8 that the microstructure consists of primary dendritic grains (light gray), eutectic grains (dark gray), and liquid pockets (black). The use of both primary and eutectic grains allows for different mechanical properties in each region.

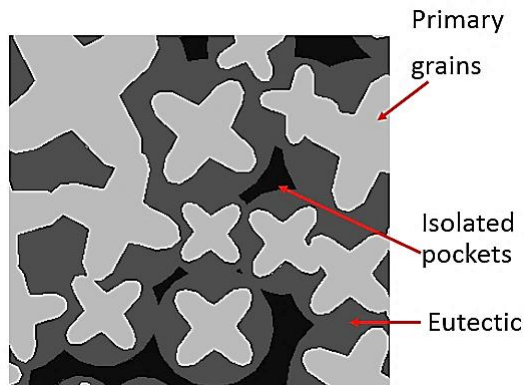


Figure 5.8 Equiaxed dendritic and spherical eutectic microstructure showing isolated pockets ($f_s=0.90$)

Model Implementation: A script file was written in the Python programming language to create and mesh the geometry within the Abaqus framework. The Voronoi diagrams were obtained using the Voro++ computational library [75]. The mechanical model was simulated using Abaqus/Standard while the fluid model utilized Abaqus/CFD. As with the exploratory

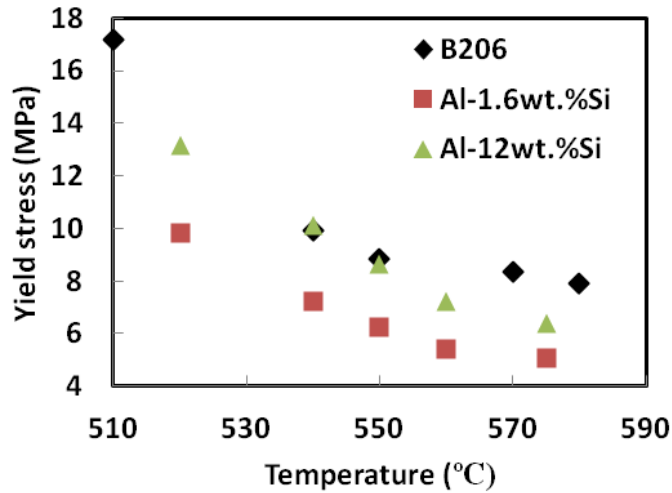
model geometries, the microstructure model geometries were extruded by 10 μm in width, deformation of the solid grains was simulated using the standard non-linear dynamic-implicit integration method provided within Abaqus assuming elastic-fully plastic constitutive behaviour, and liquid flow was assumed to be laminar and incompressible, with a constant viscosity.

Material Properties: With the exception of the yield stress, the material properties matched the ones used in exploratory model simulations presented in section 5.1. The choice of the plastic yield stress is critical for predicting the semi-solid constitutive behaviour. Since material properties depend on the chemical composition, different material properties should be considered for each phase. The B206 microstructure model consists of primary grains having a single temperature-dependent yield strength as strain-rate effects have been ignored. The A356 microstructure model consists of both primary and eutectic grains. The primary phase was assumed to contain 1.6 wt.% Si, i.e. the maximum solid solubility of Si in Al, while Al-Si eutectic occurs at 12 wt.% Si. The variations in yield strength with temperature for the various alloy compositions of interest are given in Figure 5.9 (a) as a function of temperature and Figure 5.9 (b) as a function of fraction liquid. As can be seen in the second plot, B206 has a higher yield strength as compared to either phase of A356 for the range of fraction solid above $f_s=0.85$ [43,76].

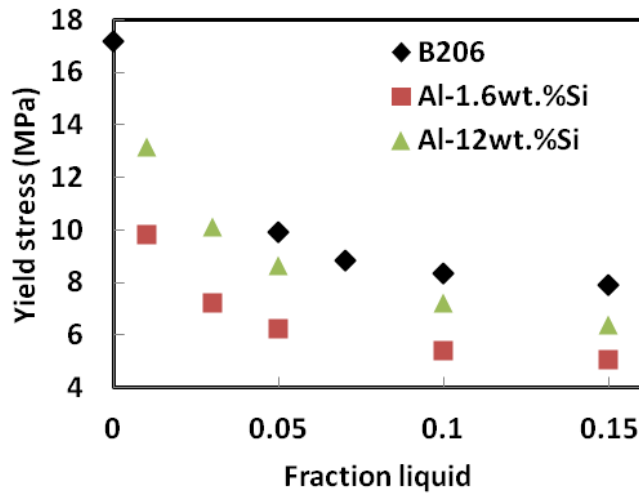
Boundary Conditions: Two different types of simulations were considered for the microstructure model. One is externally feedable (Figure 5.10), to simulate shape castings, while the other is unfeedable (Figure 5.11), to simulate Gleeble thermo-mechanical testing.

The feedable domain represents the case where the metal is cooled from the liquid state and solidified, with the solidification front well fed (having access to liquid to feed the density change associated with the L to S transformation. This would be analogous to the industrial scenario for a shape casting with a well-designed riser and gating system that provides good liquid feeding [2]. In the analysis domain employed in this study, the boundary through which feeding can occur is set at a fixed pressure ($P=0$) and the fluid flux is generally non-zero ($\Phi \neq 0$). As a result, during the semi-solid deformation fluid flow into the domain is possible.

The unfeedable domain represents the case where the material is heated from the solid to the semi-solid state – i.e. the experimental testing scenario employed in the Gleeble. Local melting initiates from the grain boundaries in low melting temperature phases. During semi-solid mechanical testing, the deformation is localized to the hottest part of the sample and flow into the domain is not possible other than associated with local strain accommodation within the microstructure. In the analysis domain employed in this study, the upper boundary is specified as a zero mass flux boundary ($\Phi=0$) and the pressure is free to change with deformation.



(a)



(b)

Figure 5.9 (a) Temperature dependent and (b) fraction liquid dependent yield stresses for B206 [76], Al-1.6 wt.% Si, Al-12 wt.% Si [43]

The applied boundary conditions for the microstructure models were as follows. First, for the solid grains (both feedable and unfeedable), FSI was applied to all surfaces in contact with the liquid phase. The bottom side was fixed in the y -direction. One node at the middle of the bottom side was fixed in the x -direction. The right and left sides were each linked to reference points; these points were then displaced by applying velocity boundary conditions for a fixed time of 10 (s). Unlike the exploratory model, reference points were used in

displacing the microstructure model, instead of directly deforming the right side, in order to acquire the reaction force data needed to calculate the semi-solid engineering stress and strain during the simulation. Velocity boundary conditions were applied to maintain constant deformation rates when simulating geometries with significantly different liquid and solid fractions and hence different fracture (in the model this is equated to a loss of convergence) strains. Velocity boundary conditions corresponding to strain rate of 0.001s^{-1} were then applied to the reference points. The maximum bulk strain at which the model reaches the convergence limit is defined as maximum strain (ϵ_{max}).

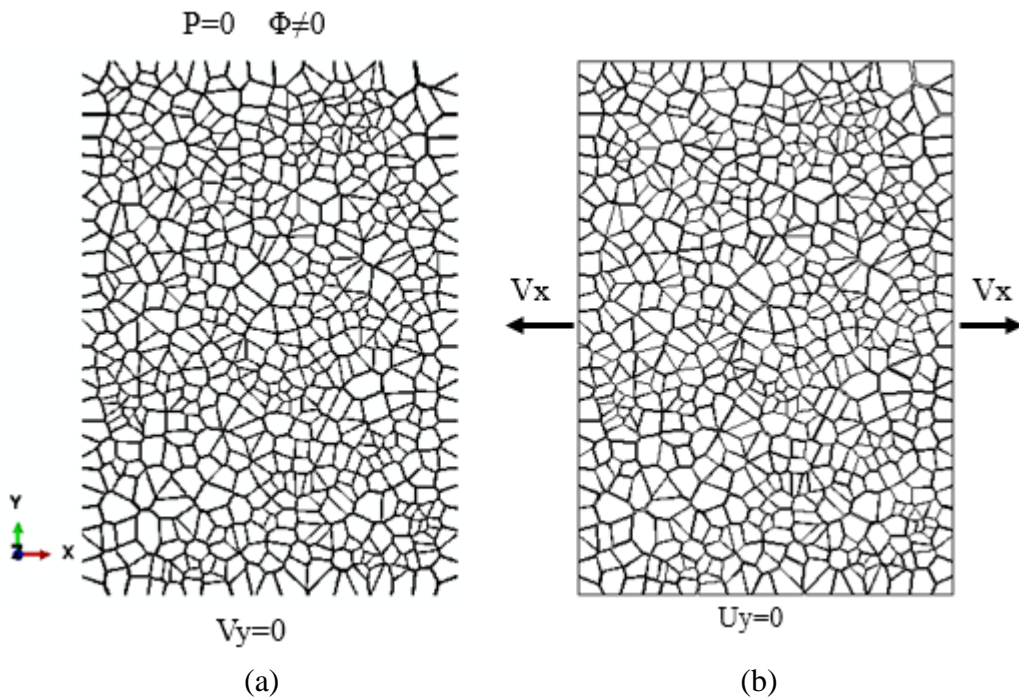


Figure 5.10 Feedable globular microstructure domain showing the boundary conditions and loads for (a) liquid channel and (b) solid grains

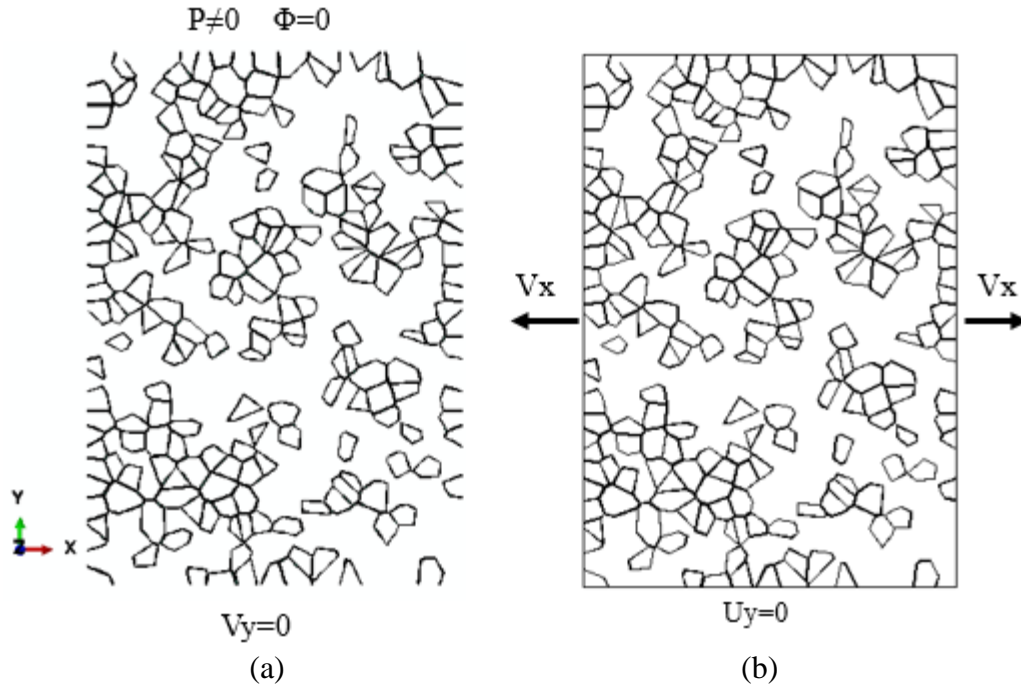


Figure 5.11 Unfeedable globular microstructure domain showing the boundary conditions and loads for (a) liquid channel and (b) solid grains

Domain Size: Microstructure model geometries were created for feedable globular B206 and unfeedable domains with globular, dendritic microstructures and A356 with dendritic primary and globular eutectic, each having 600 grains and assuming an average grain size of 100 μm . The overall domain size was: 2 mm by 3 mm for each case. Four example microstructure model geometries, at $f_s=0.95$, are shown in Figure 5.12. In this figure, the light-gray, black, and dark-gray colours represent primary grains, liquid, and eutectic, respectively. Figure 5.12 highlight and demonstrate the differences between feedable equiaxed-globular, unfeedable equiaxed-globular, unfeedable equiaxed-dendritic, and unfeedable dendritic-eutectic microstructures at a fraction solid of 0.95.

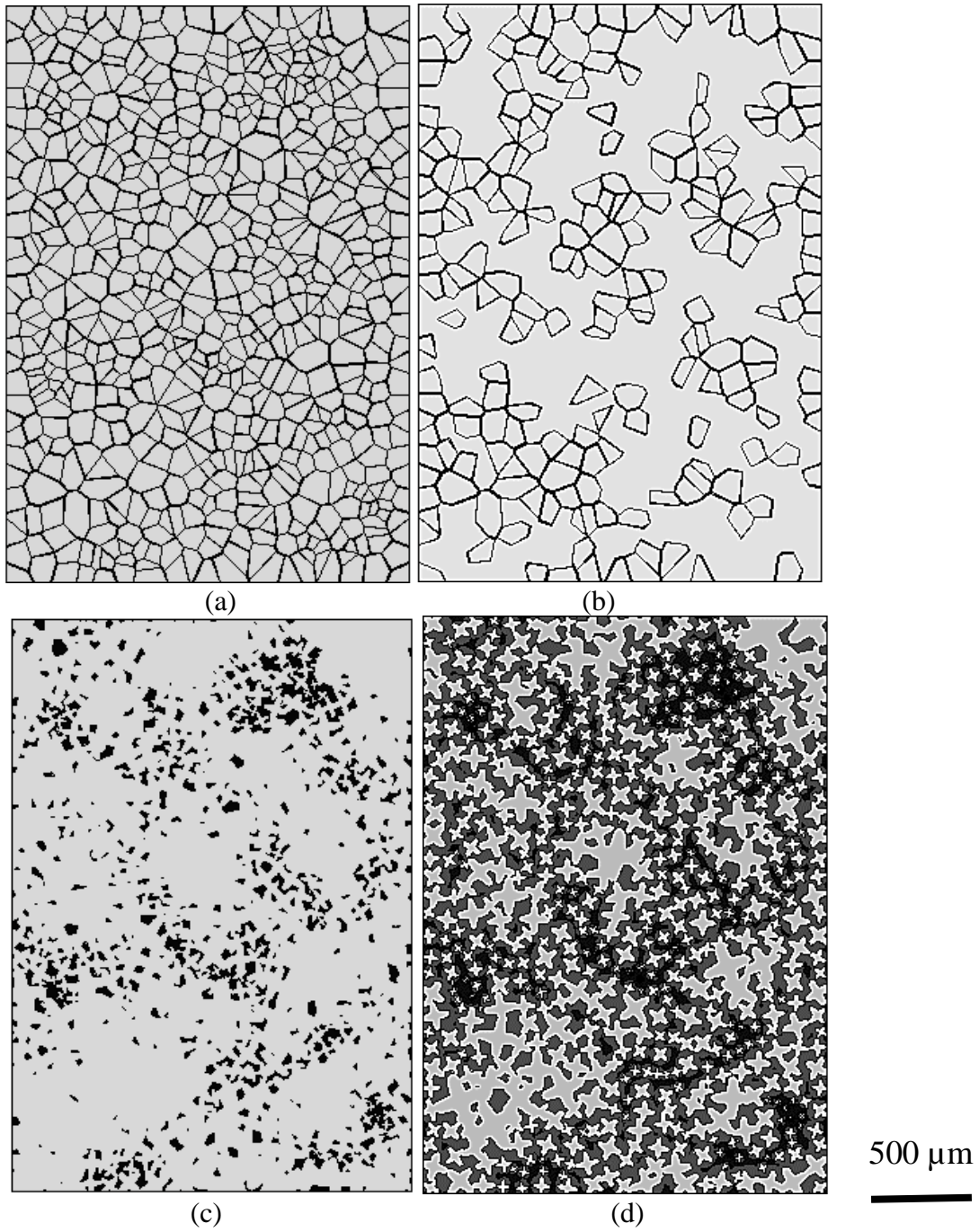


Figure 5.12 Microstructure domains for (a) Feedable globular, (b) Unfeedable globular, (c) Unfeedable dendritic, (d) Unfeedable dendritic and eutectic grains at $f_s=0.95$

In the equiaxed-globular feedable case, the domain consists of solid grains surrounded by continuous liquid channels that decrease in thickness with increasing fraction solid, however, in the equiaxed-globular unfeedable case, the domain consists of disconnected liquid channels and solid grains. In equiaxed-dendritic case, the domain consists of solid grains and small liquid pockets that are partially isolated and partially interconnected. In the dendritic-eutectic case, the liquid pockets are much larger as compared to the liquid channels in the equiaxed-globular case and further connected as compared to the equiaxed-dendritic case. The semi-solid geometry will vary as a function of fraction solid, forming an increasingly large grain network (or cluster) with increased fraction solid. In the model, the occurrence of a continuous solid network results in stress being developed only within the solid grains. This is because of the use of a 2D domain, that does not allow for concurrent percolation (or network-formation) of both the solid and liquid phases. For the case of the feedable domain, it was assumed that all the liquid channels are connected at all fraction solids. For the case of the unfeedable equiaxed-globular domain, which represents Gleeble testing, experimental results (Chapter 6) indicate that the continuous solid network forms at fraction solid greater than 0.93.

Chapter 6: Results and Discussion

In this chapter, the results obtained by applying the experimental and numerical methods introduced in Chapters 4 and 5 are presented and discussed.

6.1 Experimental Results

6.1.1 Characterization of the Microstructure Resulting from Directionally Solidifying B206 and A356

The mould presented in Chapter 4 was used to cast four B206 and four A356 wedge-shaped castings. In this section, the analysis of grain size, SDAS and porosity content is presented based on height from the chill.

Microstructure Analysis: The optical microscopy analysis demonstrates the change in the microstructure of B206 and A356 as a function of cooling rate. Figure 6.1 shows micrographs at the (I) bottom, (II) middle, and (III) top (Figure 4.2) of one as-cast B206 wedge. The microstructure contains globular primary α -Al grains (in light gray), and a eutectic mixture of Al and Cu at the grain boundaries (in dark gray). It has been reported that the eutectic micro-constituent in B206 consists additionally of the Fe/Mn phases and Al_2Cu [77]. In this study, it was assumed that the eutectic is present at the globular grain boundaries. At higher cooling rates, the grain morphology of the B206 casting (Figure 6.1 I) is characterized by a fine globular morphology. By decreasing the cooling rate, the grain size increases. Microstructural images at the (I) bottom, (II) middle, and (III) top of one of the as-cast A356 wedges are shown in Figure 6.2. This microstructure consists of 2 phases, a dendritic primary α -Al solid solution, and the eutectic. The dendrites are depicted as light gray regions in the images, while the dark gray areas show the eutectic. The primary phase

solidified from the liquid with a dendritic structure. Higher cooling rates lead to a finer microstructure with a smaller SDAS [78].

Figure 6.3 reports the grain size variation for the B206 wedge as a function of height at 12 different locations, along with the standard deviation based on 20 measurements per location. As expected, the grain size increased further away from the chill, corresponding to a decrease in the cooling rate. The grain size for B206 was $\sim 160 \mu\text{m}$ at 5 mm from the chill and increased up to $310 \mu\text{m}$ at 135 mm due to a significant reduction in cooling rate. As reported by D'Elia [79], grain size reduction significantly reduces hot tearing in B206. This is because a fine globular grain structure increases the ability of grains to move relative to one another, enabling accommodation of casting contraction and mechanical constraints.

Figure 6.4 plots the average variation in SDAS of A356 with position at 12 different locations within each wedge, along with the standard deviation based on 20 measurements at each location. As can be seen, there was a significant increase in SDAS occurring with increasing distance from the chill. The values ranged from $\sim 25 \mu\text{m}$ spacing at 5 mm up to $\sim 132 \mu\text{m}$ spacing at 130 mm.

Porosity Analysis: Porosity is another important feature of Al foundry alloys. To investigate the effect of cooling rate on porosity formation in B206 and A356, X-ray tomographic microscopy (XMT) was performed on the as-cast materials. 2D cross-section images from the tomography scans are shown in Figure 6.5 (a) and (b) for B206 and A356, respectively. In each figure, caption I refers to the bottom, caption II refers to the middle, and caption III refers to the top of the wedge casting. Porosity in Al alloys is caused by hydrogen gas and solidification shrinkage. Specifically, while hydrogen gas readily dissolves in the molten Al, its solubility is quite low in solid Al and so the gas is rejected from the solid to the

liquid during solidification. Solidification occurring at lower cooling rates generally has a greater porosity content. This is because the hydrogen has more time to diffuse from the solidifying metal to the liquid. The pores also have time to combine while the metal still contains considerable liquid [80]. From the figures, it can be seen that the level of porosity in these B206 samples is nearly zero. In A356, only the samples taken from the middle and the top of the wedge show porosity, but the total porosity fraction remains very low. The very low hydrogen porosity is a result of degassing in Ar, performed prior to casting, and the use of a well-designed moulding system (basin, sprue, and gate). These XMT images thus indicate that the casting was well designed, with little porosity to act as crack initiation sites.



(I)

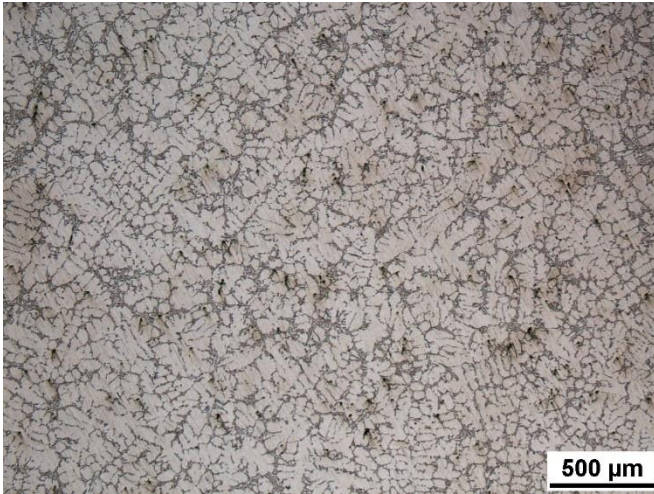


(II)

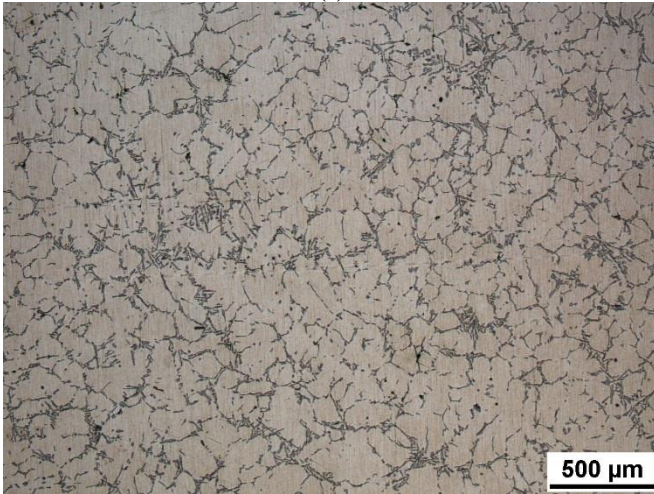


(III)

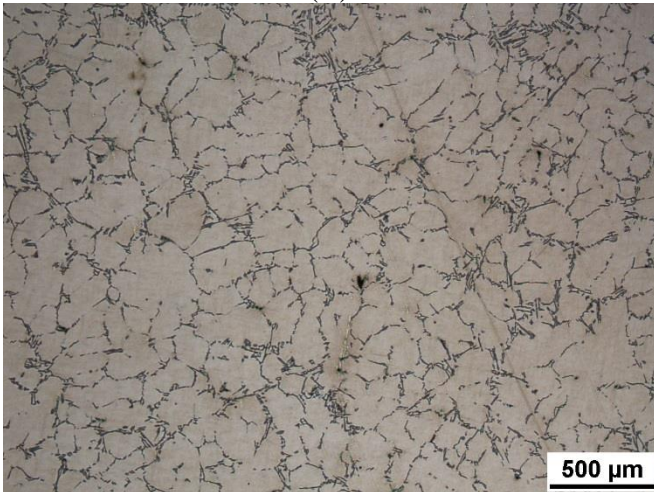
Figure 6.1 Optical micrographs of B206 taken from the (I) bottom (CR=2.5 °C/s), (II) middle (CR=0.14 °C/s), and (III) top (CR=0.04 °C/s) of the wedge casting



(I)



(II)



(III)

Figure 6.2 Optical micrographs of A356 taken from the (I) bottom ($CR=1.81^{\circ}C/s$), (II) middle ($CR=0.12^{\circ}C/s$), and (III) top ($CR=0.08^{\circ}C/s$) of the wedge castings

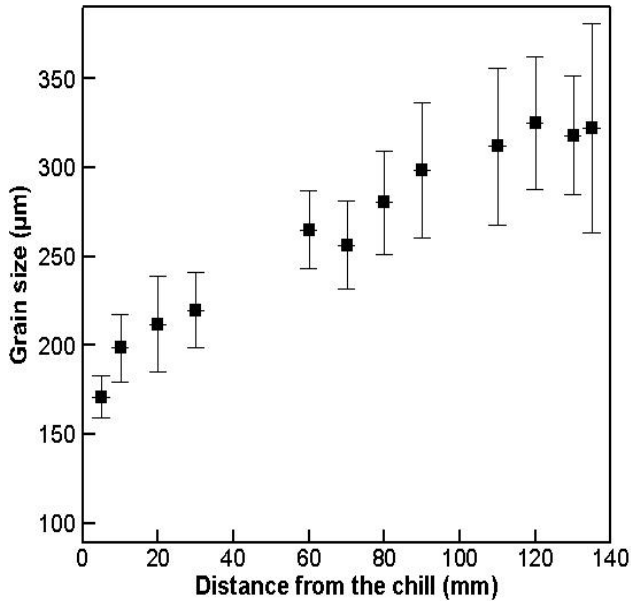


Figure 6.3 Variation in the measured grain size for B206 as a function of distance from the chill

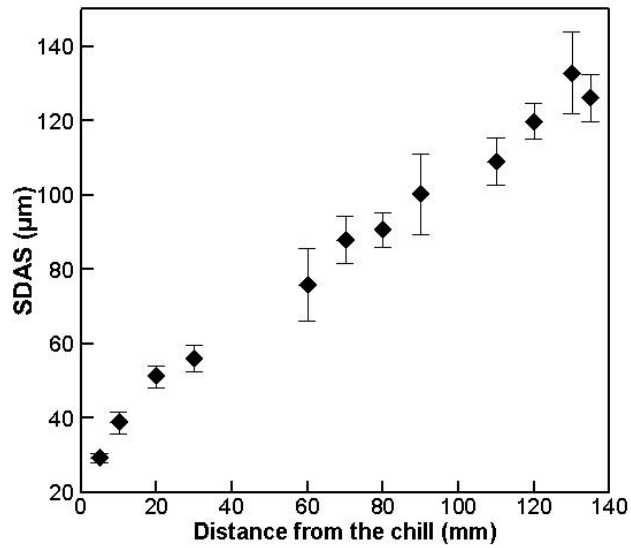
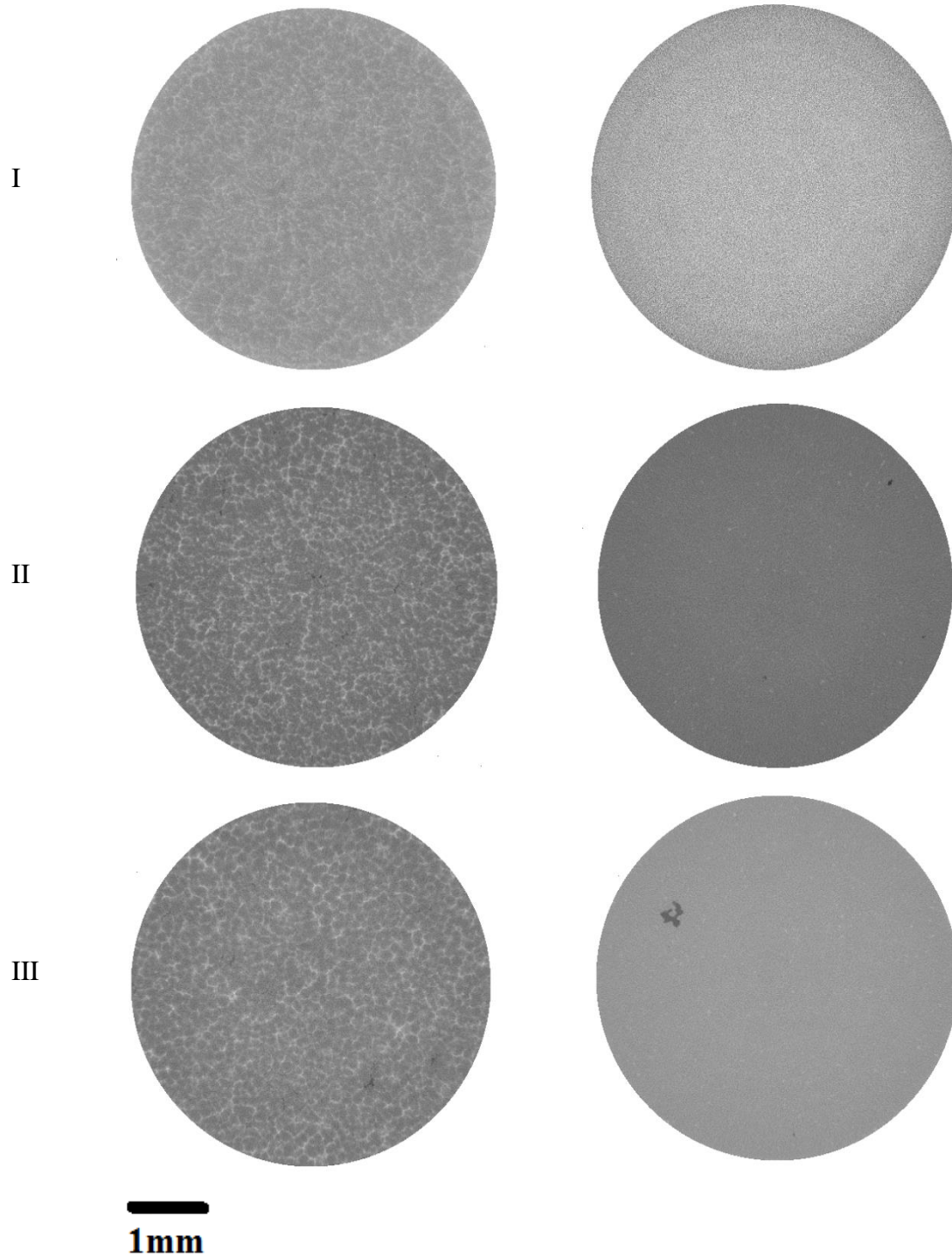


Figure 6.4 Variation in the measured SDAS for A356 as a function of distance from the chill

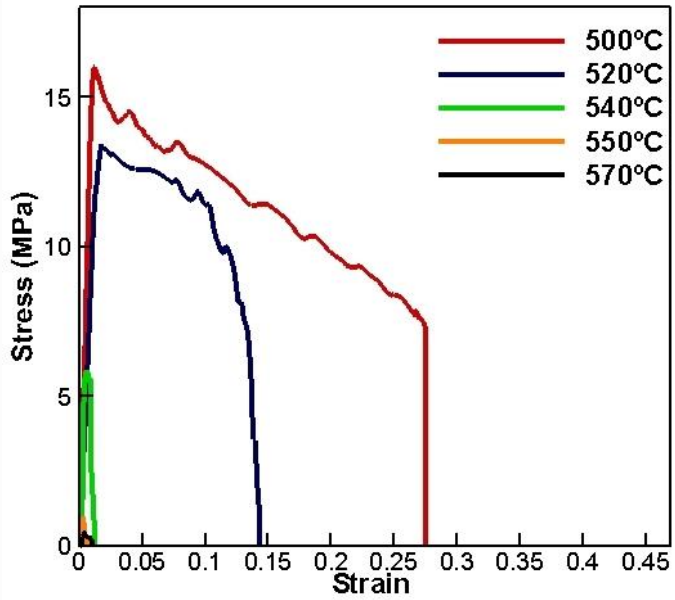


(a) (b)
 Figure 6.5 Transverse sections from the tomographic reconstruction of (a) B206 and (b) A356 specimens taken from the (I) bottom, (II) middle, and (III) top of the wedge castings

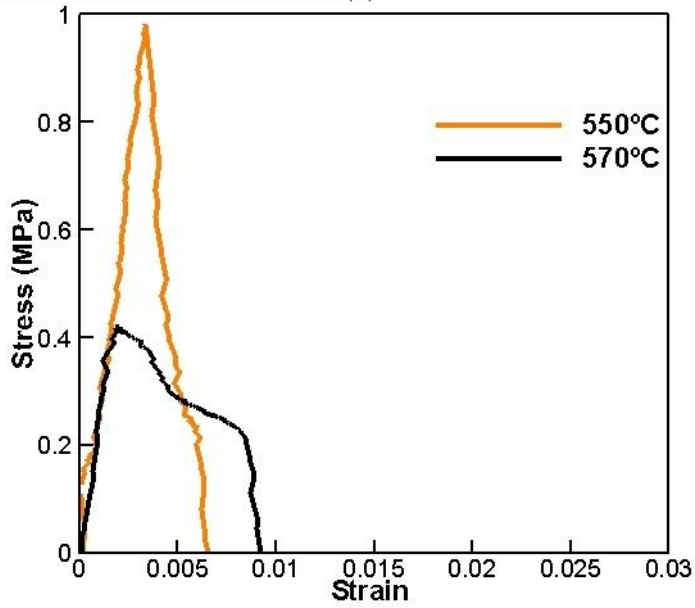
6.1.2 Characterization of the Semi-solid Constitutive Behavior Resulting from the Thermo-Mechanical Testing of B206 and A356

Semi-solid tensile tests were performed on both B206 and A356, in the as-cast and HIP conditions, at temperatures between 500°C to 570°C on samples taken from the bottom, middle, and top of the wedges. The effects of three different factors, temperature, microstructure size (Grain size/SDAS), and HIP processing on the semi-solid behaviour were studied. The results are presented below. First, some examples showing the measured data for as-cast alloys are given to illustrate the wide range in constitutive behaviour that occurs over a small change in test temperature. Then the yield stress and ductility are quantified as a function of fraction solid and grain size/SDAS. This allowed for the study of the effect of cooling rate on the semi-solid yield stress and ductility of B206 and A356. Finally, the effect of the HIP processing is explored.

Example Measured Data: Figure 6.6 (a) shows examples of engineering stress-strain curves of as-cast B206 samples, while Figure 6.7 (a) shows the engineering stress-strain curves of as-cast A356 samples. The stress-strain curves resulting from the tests at high temperatures, having peak stresses below 1 MPa and 3 MPa, respectively, are plotted in separate graphs and shown in Figure 6.6 (b) and 6.7 (b). Note that a moving average statistical method was calculated by taking the arithmetic mean of sets of 20 values and was used to smooth out fluctuations.

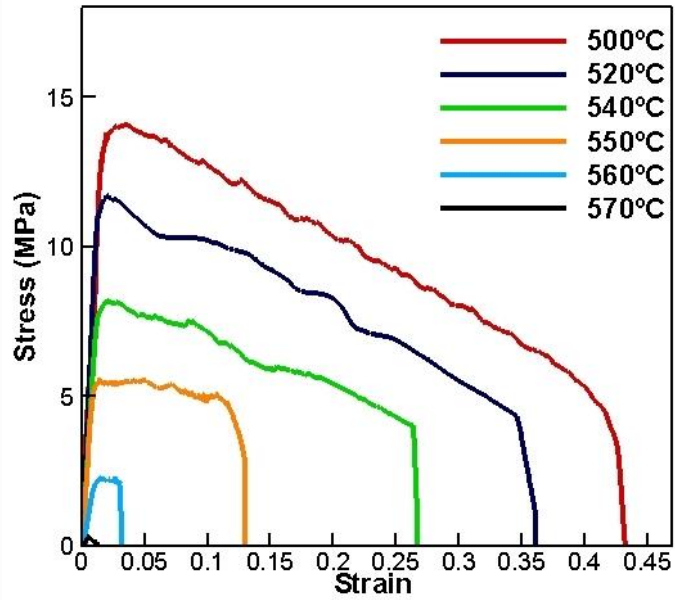


(a)

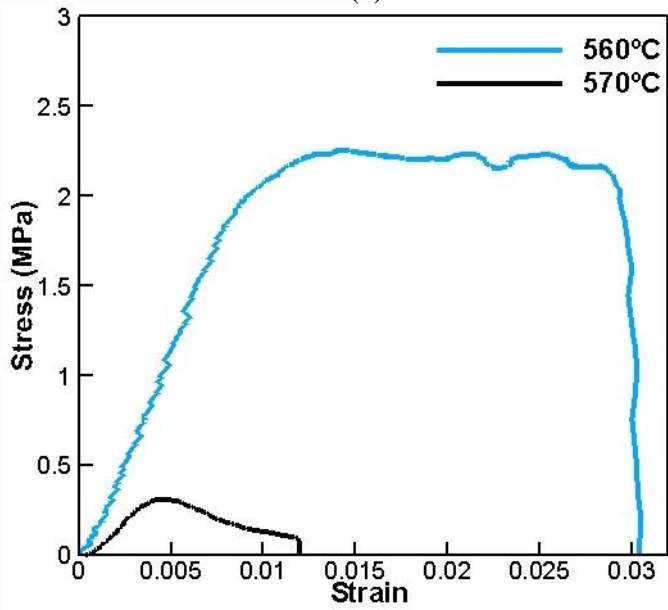


(b)

Figure 6.6 Example of engineering stress-strain curves of as-cast B206 alloy (a) tested at 500°C, 520°C, 540°C, 550°C, and 570°C, and (b) at stress lower than 1 MPa (for the samples taken from the bottom of the wedges)



(a)



(b)

Figure 6.7 Example of engineering stress-strain curves of as-cast A356 alloy (a) tested at 500°C, 520°C, 540°C, 550°C, 560°C, and 570°C, and (b) at stress lower than 3 MPa (for the samples taken from the bottom of the wedges)

Effect of Temperature on Yield Stress and Ductility: Overall, Figures 6.6 and 6.7 give some insight into the semi-solid constitutive behaviour of B206 and A356. For both alloys, it can be seen that the stress linearly increases to a maximum value with increasing strain before then gradually decreasing until the fracture point, when there is a sudden drop in the stress. With increasing temperature, yield stress and ductility decrease significantly. It is interesting to note that the decrease in the yield stress and ductility with increasing temperature is more uniform in the A356 alloy; however, there is a sudden drop of the mechanical properties of B206 samples at 540°C.

A comparison of Figures 6.6 and 6.7 shows that at relatively low temperatures such as 500°C, B206 has higher yield stress than A356, however, A356 appears to have higher yield stress at higher temperatures. At almost all temperatures, A356 was shown to have higher ductility. This can be explained by considering the effect of the eutectic, which plays an important role in semi-solid deformation. It has often been reported in the literature that a high fraction of eutectic results in an increase in semi-solid ductility as reviewed in Section 2.3.1. It was reported that in alloys with large amounts of eutectic, sufficient liquid is present below the rigidity temperature to assist in the movement of the solid network [30].

Due to the differences in the phase diagram of these alloys, it is more reasonable to consider the variation of mechanical properties as a function of fraction solid since the temperatures of interest are so similar. For example, at 570°C the corresponding fraction solid of B206 and A356 are 0.90 and 0.80. So, it is not easy to compare the effect of temperature on two materials due to differences in fraction solid. Furthermore, since the tests in the current study were carried out by re-melting the specimens under non-equilibrium conditions, the actual fraction solid at given temperatures is not easy to obtain. In order to

correlate the semi-solid tensile properties with fraction solid, a number of assumptions were made. First, it was assumed that the evolution in fraction solid with temperature is cooling rate-independent. Second, it was assumed that the evolution in fraction solid with temperature is the same during re-melting or solidification. Third, it was assumed that the gauge length region of the tensile test samples is isothermal during Gleeble thermo-mechanical testing. The variation in yield stress and ductility as a function of fraction solid was specified using the fraction solid/temperature relationships shown in Figure 5.3.

Effect of Fraction Solid and Microstructure Size on Yield Stress: The measured engineering yield stress for the B206 and A356 samples in the as-cast condition, as a function of fraction solid in the ranges from 0.90 to 1 for B206 and 0.8 to 1 for A356, are shown in Figure 6.8 (a) and (b). For the most part, the classical 0.2% offset method was used to define the yield stress. For samples with very low ductility, if the failure strain was smaller than 0.2%, the highest stress was reported as the yield stress.

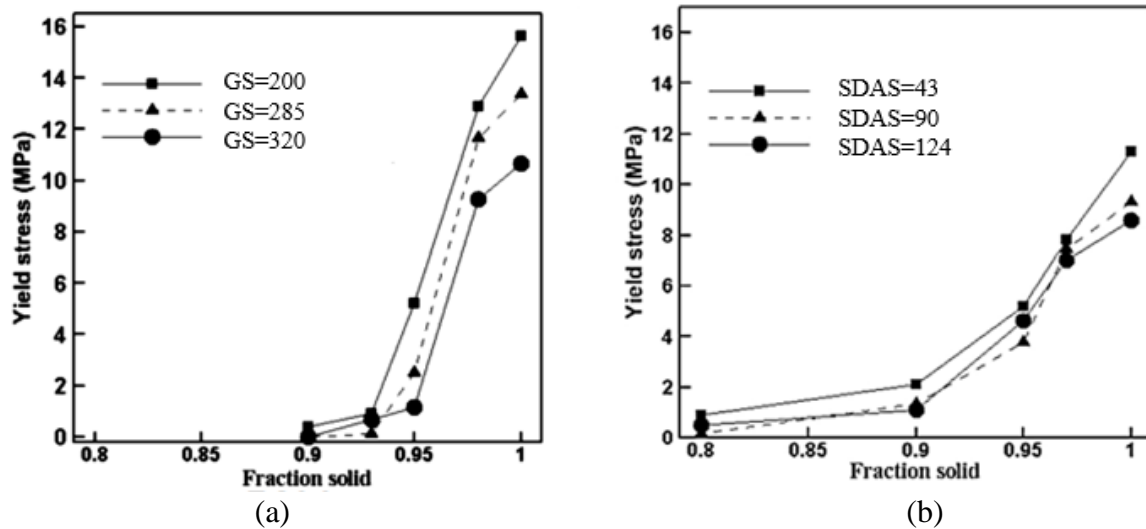


Figure 6.8 Variation in yield stress with fraction solid for (a) B206 with different grain sizes (GS) and (b) A356 with different SDAS

Effect of Fraction Solid: As can be seen in Figure 6.8, the yield stress decreases with decreasing fraction solid for both B206 and A356, as expected. This is because, by decreasing the fraction solid, the liquid films around grains become thicker, and the grains themselves become more ellipsoidal and spherical, enabling rotation and sliding between solid grains [6]. Chen et al. [81] additionally reported a strong lubricating effect by the liquid during semi-solid deformation, significantly decreasing yield stress.

Figure 6.8 (a) shows that for all B206 samples, with different grain sizes, decreasing the fraction solid from 1 to 0.95 sharply decreases the yield stress. Specifically, the yield stress decreases from values greater than 10 MPa to less than 1 MPa. With a further decrease in fraction solid to 0.95, the yield stress gradually decreases to values close to zero. During the re-melting process at fraction solid near 0.95, the solid grains start losing coalescence and the semi-solid undergoes a transition from a dense and compact structure to separated grains that are surrounded by the liquid channels.

Figure 6.8 (b) shows that for all A356 samples, with different SDAS, a decrease in the fraction solid from 1 to 0.80 also causes the yield stress to decrease but in a more gradual way as compared to B206. The yield stress reached very low values at fraction solid of 0.80. Nguyen et al. [12] also examined semi-solid deformation in A356, by performing compression tests. Their results show that specimens with fraction solid smaller than about 0.85 have very low yield stress.

In the case of B206, the grains are almost round, as shown in Figure 6.1, which allows them to rearrange easily by sliding in relation to each other during straining, and thus strength develops more slowly [21]. For A356, however, the dendritic grains are highly branched and are quite entangled with each other, as shown in Figure 6.2, and the structure

cannot accommodate strain by rearrangement of the grains. Instead, the strain must be accommodated by the deformation of the dendrites themselves, and extensive dendrite fragmentation occurs as reported by Eskin et. al [5], Strength, therefore, increases rapidly.

Effect of Microstructure Size (Grain Size/SDAS): In order to study the effect of microstructure size on the semi-solid yield stress, tensile tests were carried out on samples taken from the bottom, middle and top of the wedges. In the case of B206, it can be seen that for fraction solids greater than 0.95, the yield stress decreases with increasing the grain size. However, at lower fraction solids, grain size does not have a significant effect on yield stress.

For A356, as shown in Figure 6.8 (b), it appears that by increasing the SDAS, yield stress decreases; however, changing the SDAS from a moderate value $\sim 90 \mu\text{m}$ to a large value of $\sim 125 \mu\text{m}$ doesn't seem to have a significant effect on yield stress. Larger microstructure features deteriorate the semi-solid tensile properties since they lead to wider liquid channels for a given fraction solid, as a consequence, strain accumulation in the liquid increases during the deformation. However, due to large eutectic fraction in A356, the liquid channels are quite large as compared to B206. This decreases the effect of SDAS on the semi-solid tensile behaviour.

Effect of Fraction Solid and Microstructure Size on Ductility: Although the strength of a semi-solid alloy is an important property for modelling casting processes, semi-solid ductility is considered by many to be the key property of interest for predicting hot tearing susceptibility [5, 17, 79]. This is because the ductility characterizes the capability of the mush to accommodate the semi-solid deformation resulting from thermal contraction and thermal gradients [2]. The engineering fracture strain or ductility of B206 tested at fraction solids from 0.90 to 1, and A356 as-cast specimens tested at fraction solids from 0.8 to 1 are

shown in Figure 6.9 (a) and (b) for the positions bottom, middle, and top. The ductility was measured based on the movement of the cross-head up to the point of fracture.

Effect of Fraction Solid: For B206 the ductility results for the samples taken from the bottom and middle of the wedges show typical behaviour and qualitatively match those for yield stress, Figure 6.8 (a) and (b). At very high fraction solids (0.98-1), the semi-solid ductility is quite high but decreases with decreasing fraction solid. At fraction solids lower than 0.95 the semi-solid ductility is very small (almost zero). The semi-solid ductility of A356 shows similar trends, with the ductility being very low at fraction solids smaller than 0.90.

Effect of Microstructure Size (Grain Size/SDAS): For B206, by increasing the grain size from $\sim 200 \mu\text{m}$ to $\sim 285 \mu\text{m}$, and then to $\sim 320 \mu\text{m}$, the ductility of the semi-solid material decreases, but only at very high fraction solid. At lower fraction solid, a change in the grain size is seen to have very little effect. For A356, by increasing the SDAS from $\sim 43 \mu\text{m}$ to $\sim 90 \mu\text{m}$, the ductility of the semi-solid material decreases. However, by further increasing the SDAS to $\sim 124 \mu\text{m}$, there is only a slight variation in the ductility. The effect of microstructure size on the semi-solid ductility is complex. At lower fraction solids, the grains are less entangled and thus changes in SDAS or grain size appear to have a negligible effect on the semi-solid tensile properties. At high fraction solid, as microstructure size is a function of cooling rate, the resulting difference in micro-segregation may depress the solidus temperature, and the distribution of eutectic particles, thereby changing the apparent tensile properties [2].

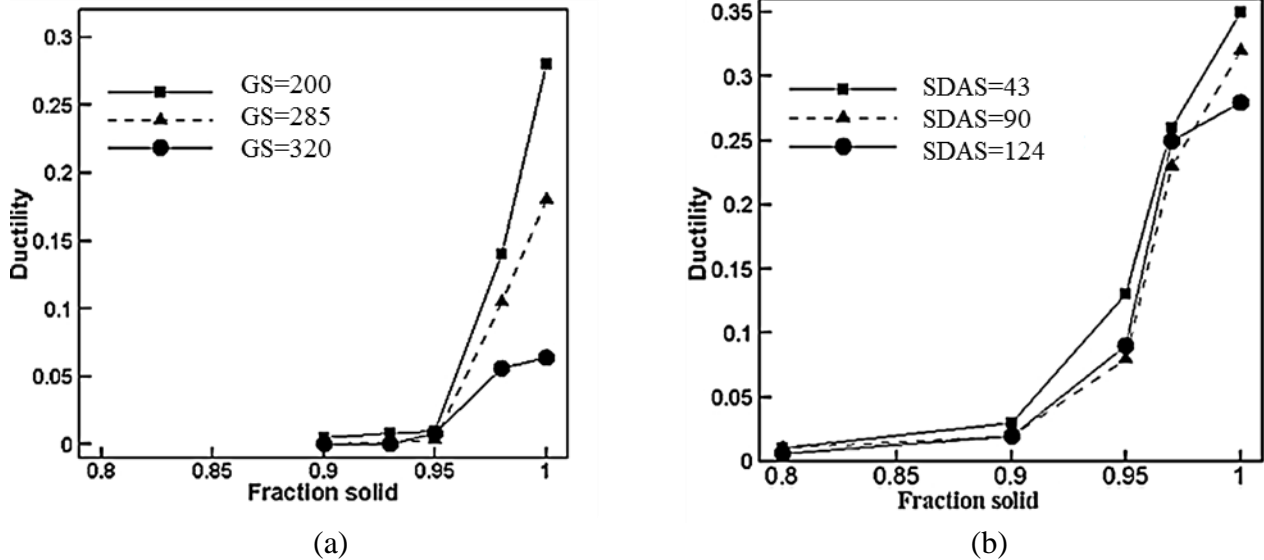


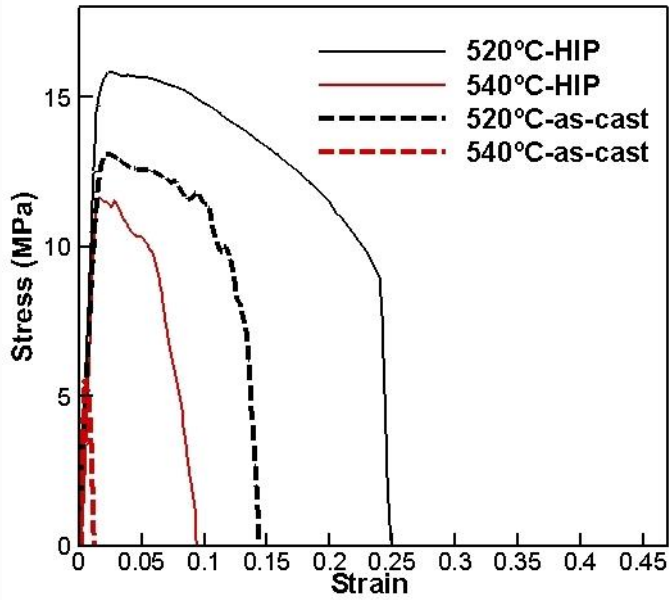
Figure 6.9 Variation in ductility with fraction solid for (a) B206 with different grain sizes (GS) and (b) A356 with different SDAS

Effect of HIP Process on Yield Stress and Ductility: In order to study the effect of HIP on the semi-solid tensile properties, stress-strain curves of HIP and as-cast samples tested at the same temperatures were compared. Example stress/strain curves, for B206 at 520°C and 540°C, and A356 at 520°C and 560°C are shown in Figure 6.10 (a) and (b). As can be seen, both yield stress and ductility of B206 and A356 increase because of the HIP. It seems that at 520°C there is a greater difference between the ductility of as-cast and HIP B206 samples than the A356 samples. For example, HIP increases the ductility of B206 samples, tested at 520°C, from 0.15 to 0.35. However, the increase in A356 is only from 0.36 to 0.40. The semi-solid yield stress and ductility of all the as-cast and HIP samples are summarized in Appendix A.

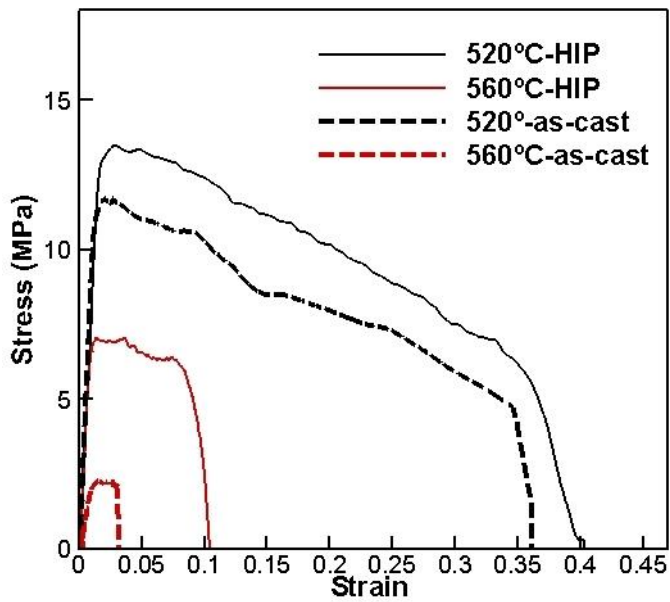
It has been shown previously that HIP has a positive effect on room temperature ductility, while there is not an obvious improvement in yield stress [92-94]. It has also been shown that the HIP process improves semi-solid mechanical properties. Removing the as-

cast porosity has been stated to be the key factor of HIP [8]. Since in this study the amount of as-cast porosity was found to be very low, as a result of degassing, it was expected that HIP and as-cast samples would show similar ductility and yield stress. As shown in Figure 6.10, however, HIP samples have significantly higher ductility as well as higher yield stress for a given test temperature. Thus, it appears that HIP processing has another dominant effect.

Other researchers [82] have studied the effect of micro-segregation on tensile properties of aluminum alloys. They showed that micro-segregation has a deleterious effect, resulting in reduced ductility of the samples tested at room temperature. Since the HIP process applies pressure at high temperature for extended periods of time, it is expected to reduce the amount of micro-segregation. A homogenized alloy will have a higher solidus temperature and subsequently higher semi-solid tensile properties (yield stress and ductility) as compared to non-homogenized samples tested at the same temperatures.



(a)



(b)

Figure 6.10 Stress-strain curves HIP and as-cast (a) B206 at 520°C and 540°C, and (a) A356 at 520°C and 560°C

To investigate the extent of homogenization resulting from the HIP process on the as-cast B206, an SEM-EDX analysis method known as WIRS [83] was applied. Figure 6.11 shows the resulting variation in Cu content as a function of fraction solid based on

measurements at 100 different locations within the microstructure for as-cast and HIP material B206. This figure provides an estimate of Cu segregation during solidification by assuming that the location with the lowest Cu content is the dendritic core and thus $f_s=0$ and that the location with the highest Cu content is the last liquid to solidify in the interdendritic region and thus $f_s=1$

It can be seen that the HIP material is basically homogenized, while the as-cast material shows considerable segregation. As explained in this section, HIP materials have higher tensile properties compared to the as-cast ones. It has been shown in this study that HIP process improves yield stress and ductility of the semi-solid samples by reduction of the micro-segregation and eliminating low melting point phases. It can be concluded that corresponding fraction solid of HIP samples is expected to be higher than as-cast samples. As a result, the HIP samples have greater properties in comparison to the as-cast samples tested at the same temperature, because of higher fraction solid. It can be concluded that the dominant effect of HIP on tensile properties is the homogenization of the material, and not removing the as-cast porosities. Because of this, HIP samples should not be used to characterize the semi-solid constitutive behaviour of as-cast engineering alloys.

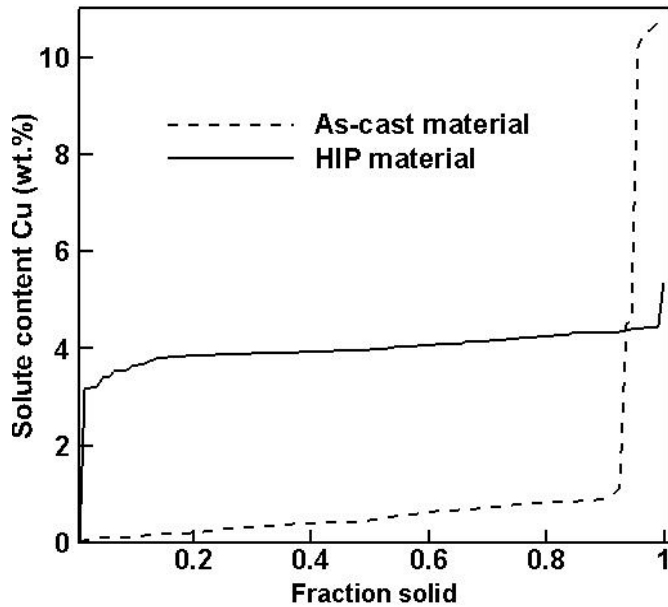


Figure 6.11 Solute profiles of Cu in B206 in both as-cast and HIP conditions

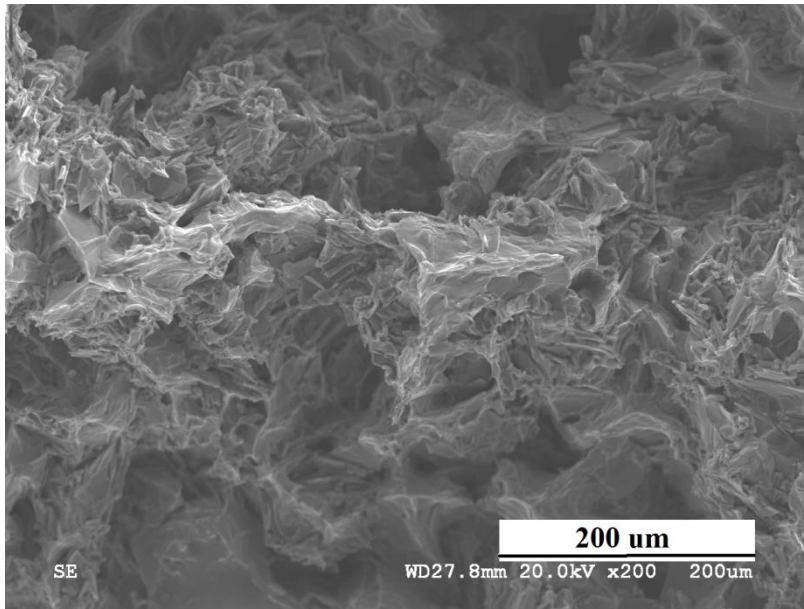
Repeatability Analysis: In order to investigate the repeatability of the Gleeble semi-solid tensile testing experimental procedure, three A356 samples at 520°C and three B206 samples at 570°C were tested. Due to the limited number of available samples, the repeatability tests were performed only on as-cast A356 samples with small SDAS and tested at 520°C and HIP B206 samples with small SDAS tested at 570°C. Table 6.1 shows the resulting yield stress and ductility measurements. It can be seen that the variation in the yield stress and ductility between the three tests for both B206 at high temperatures and A356 at low temperatures is very minimal. The measured yield stress standard deviations for each experimental group were reported to be 0.03 and 0.6, respectively. The measured data shows a high repeatability which is required to know whether the experimental results are reliable.

Sample	Temperature (°C)	Yield stress (MPa)	SD	Ductility	SD
B206	570	1.27	0.03	0.01	0.01
		1.25		0.01	
		1.20		0.03	
A356	520	12.2	0.6	0.38	0.025
		11.3		0.33	
		10.9		0.35	

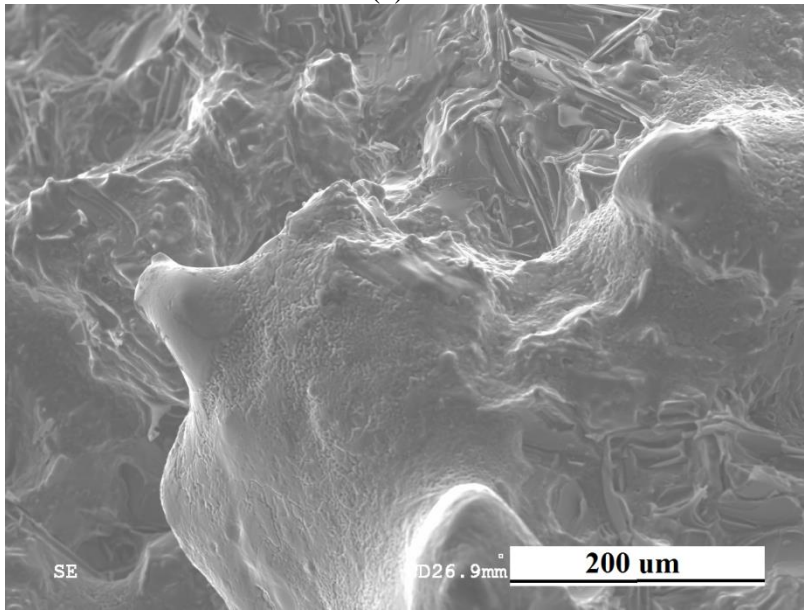
Table 6.1 Yield stress and ductility of B206 samples and A356 samples tested at 570°C and 520°C

Fractography: SEM analysis was carried out on the as-cast samples taken from the bottom of the chill. Some examples of the fracture surface are given in this section to discuss the effect of the liquid phase on the failure mechanism of the alloys. SEM images of fracture surfaces taken from as-cast B206 and A356 specimens at 200X magnification are shown in Figure 6.12 and Figure 6.13.

Figure 6.12 (a) shows the SEM image of A356 samples tested at 500°C. As can be seen, there is no liquid present on the fracture surface, indicating that the sample was tested at fully solid state. The fracture surface shows a dendritic network that is highly entangled. Micro-voids confirm the ductile behaviour of the material. By increasing the test temperature to 540°C, Figure 6.12 (b), it can be seen that most of the fracture surface is covered by the liquid. It confirms that the dominant fracture mode is the liquid film rupture. Figure 6.13 (a) shows the SEM image of B206 samples tested at 540°C. As can be seen in the figure, the globular microstructure is significantly bridged and mostly covered by the liquid phase. There is some evidence of porosity formation at the triple junctions, as shown by the arrows. At a higher test temperature of 570°C, Figure 6.13 (b), the fraction solid is clearly much lower, although there are still dry grain boundaries that could have acted as crack nucleation sites.



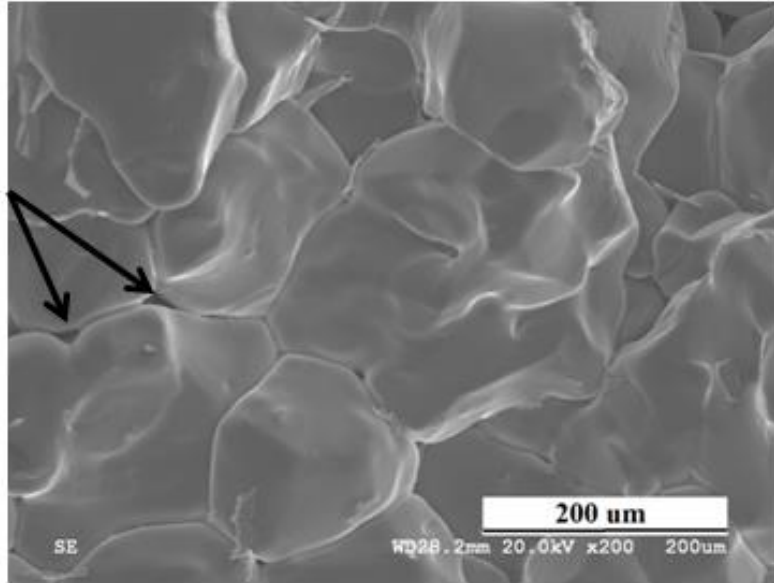
(a)



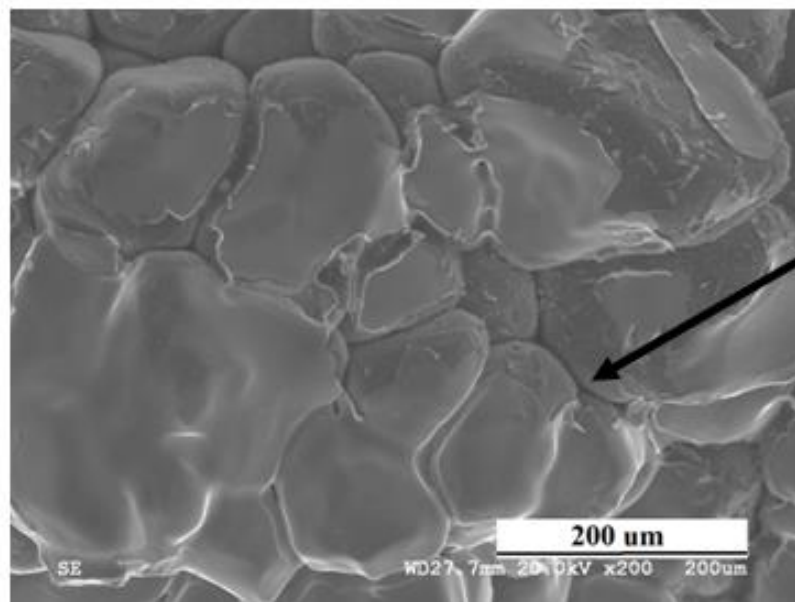
(b)

Figure 6.12 SEM images of the fracture surface of as-cast A356 specimens (a) 500°C, (b) 540°C

Porosity at
triple
junction of
the grains



(a)



Dry grain
boundaries

(b)

Figure 6.13 SEM images of the fracture surface of as-cast B206 specimens (a) 540°C, (b) 570°C

6.1.3 Discussion of Experimental Results and Comparison to Past Work

In this section, the major findings of the experimental section are summarized and compared with the published data. Many researchers have studied the semi-solid behavior of Al alloys (e.g. [5, 8, 81]). Although there is similar work, the effects of microstructure size on tensile properties of commercial foundry alloys have not been previously studied. One of the main challenges in determining semi-solid constitutive behaviour is the reproducibility of the test results since multiple experiments with the same conditions can lead to different results depending on the testing method.

A few studies have been carried out to characterize the semi-solid constitutive behaviour of B206 under compression [76] and tensile load [54]. However, several researchers have studied and reported the semi-solid tensile behaviour of a similar alloy, Al-(1-5) wt.%Cu [5, 84]. In research presented by Bolouri et. al [54], semi-solid Gleeble tensile tests were carried out on materials at strain rates of 0.001. Ludwig et. al [84] used a solidifying sample to measure shear yield stress at a strain rate of 0.0001 s^{-1} . In Figure 6.14, the experimental results for B206 samples having small SDAS and tested at a strain rate of 0.003 s^{-1} are compared with the results from [54] and [84]. As can be seen, the newly-collected data is quite similar to the prior results. The yield stress values at fraction solids higher than 0.95 are in good agreement with those measured by Bolouri, while the measured yield stresses at $f_s=0.90$ and $f_s=0.93$ more closely match the Ludwig data. The results in this thesis extend these prior experiments by additionally examining the role of microstructure morphology as well as micro-segregation. The rigidity point was shown to be 0.93 for B206 which is similar to Ludwig's work. The difference between the current work and Bolouri's research is that the test temperatures in the current study are extended to higher temperature

which results in a wider fraction solid range (0.90 – 1) in comparison with Bolouri's research fraction solid range (0.96 – 1). Comparison of the current work and Ludwig's research shows that at fraction solids smaller than the rigidity point, $f_s=0.93$ in this case, tensile and shear semi-solid testing methods results are very close. This may mean that shear tests can be used instead of tensile tests in this range of fraction solid; more work is needed to verify this finding. At fraction solid higher than the rigidity point a tensile test should be carried out.

In contrast to B206, a number of studies have been carried out to characterize the semi-solid constitutive behaviour of A356. In research by Nguyen et al. [12] and Benke et al. [85], semi-solid tensile tests were carried out on this material at strain rates of 0.008 and 0.005 s⁻¹, respectively. In Figure 6.15, the experimental results for A356 samples having small SDAS and tested at a strain rate of 0.003 s⁻¹, are compared with the results from [12] and [85]. As can be seen, the newly-collected data is quite similar to the prior results. The yield stress values at fraction solids higher than 0.80 are in good agreement with those measured by Nguyen, while the measured yield stresses at $f_s=0.80$ more closely match the Benke data. The results in this thesis extend these prior experiments by additionally examining the role of microstructure morphology as well as micro-segregation. The rigidity point was shown to be 0.80 for A356 which is similar to Benke's work.

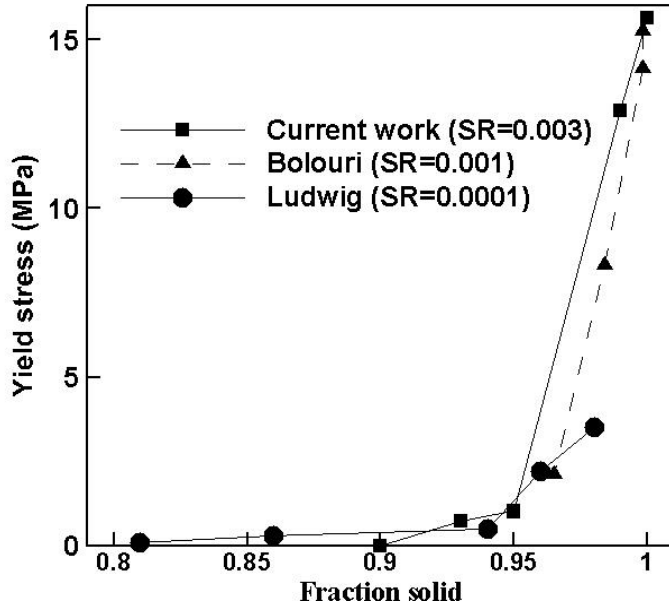


Figure 6.14 Comparison of semi-solid yield stress for obtained from the Gleeble test and measured by Bolouri [54] and Ludwig [84] for B206

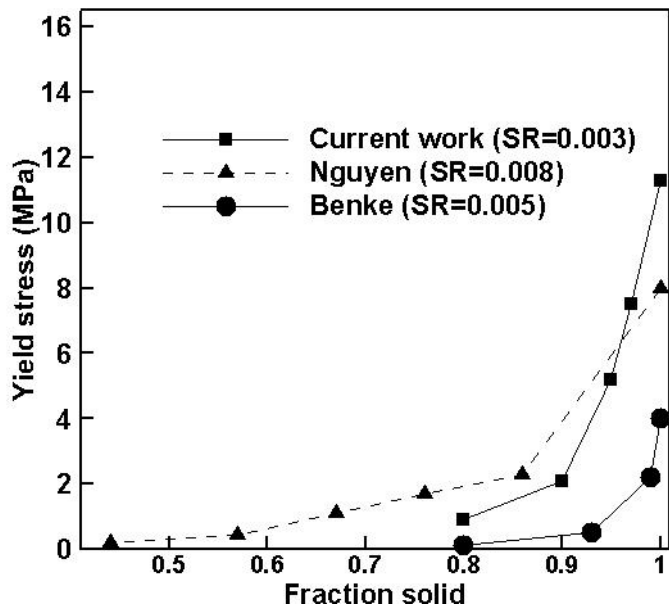


Figure 6.15 Comparison of semi-solid yield stress for obtained from the Gleeble test and measured by Nguyen [12] and Benke [85] for A356

6.1.4 Experimentally-based Assessment of the Hot Tearing Sensitivity

Since the primary goal of this study was to compare and contrast the hot tearing tendency of two commercial foundry alloys, the new experimental results are used in this section to predict the hot tearing tendency of the mentioned alloys. As mentioned in the literature review, Chapter 2, the mechanism of hot tearing is complex because it involves both macro-scale phenomena (stresses/strains and thermal variations) and microstructural phenomena (fluid flow and microstructure). Existing hot tearing criteria are based on mechanical phenomena (stress and strain) and physical phenomena (microstructure size, geometry, and permeability) [21]. A mechanical (stress-based) and a non-mechanical (liquid feeding based) hot tearing criteria are applied below using the findings of the current study to compare B206 and A356 hot tearing susceptibility.

Langlais and Gruzleski's Criterion: Langlais and Gruzleski [86] defined a stress-based criterion for hot tearing susceptibility of material based on the maximum tensile strength at $f_s=0.95$, $\sigma_{0.95}$, as shown in Equation 6.4.

$$HTS_{LG} = \frac{1}{\sigma_{0.95}} \quad (6.4)$$

The Gleeble results were implemented in this stress-based criterion to find the HTS_{LG} values and hence compare B206 and A356. The results, given in Table 6.2, indicate that B206 is more susceptible to hot tearing than A356, and furthermore is sensitive to variations in SDAS. In contrast, in A356, changing the SDAS does not seem to have a great effect on the HTS_{LG} value.

Materials	Location	Stress at $f_s=0.95$	HTS_{LG}
B206	Bottom	5.2	0.19
	Middle	2.5	0.40
	Top	1.1	0.90
A356	Bottom	5.0	0.20
	Middle	3.7	0.27
	Top	4.6	0.21

Table 6.2 HTS_{LG} values for B206 A356 based on Langlais and Gruzleski's theory for samples taken from the bottom, middle, and top of the wedges

Clyne and Davies' Criterion: The hot tearing criterion proposed by Clyne and Davies [3] is based on the assumption that it is difficult for the liquid to move freely in the last stage of freezing so that the strains developed during this stage cannot be accommodated by the liquid feeding. They consider this last stage as the most susceptible to hot tearing. The cracking susceptibility coefficient is thus defined by:

$$HTS_{CD} = \frac{t_{0.99} - t_{0.9}}{t_{0.9} - t_{0.4}} \quad (6.5)$$

where $t_{0.99}$, $t_{0.9}$, and $t_{0.4}$ are the times when $f_s=0.99$, 0.90 and 0.40 respectively. Using the thermocouple data and fraction solid variation with temperature (Figure 5.3), the HTS_{CD} was calculated for A356 and B206 samples with different cooling rates. It was assumed that the fraction solid evolution with fraction solid is cooling rate independent. Table 6.3 shows the calculations for HTS_{LG} of B206 and A356 samples based on thermocouples data located at 5, 70, and 120 mm from the chill.

Materials	Thermocouple location (mm)	$t_{0.99}$ (s)	$t_{0.9}$ (s)	$t_{0.4}$ (s)	HTS_{CD}
B206	5	331.314	55.173	7.173	5.75
	70	540.76	369.56	128.40	0.70
	120	575.76	422.56	257.36	0.92
A356	5	39.40	36.72	28.01	0.30
	70	198.80	181.00	126.61	0.32
	120	408.42	368.03	214.40	0.26

Table 6.3 HTS_{CD} values for B206 A356 based on Clyne and Davies' Criterion for samples taken from the bottom, middle, and top of the wedges

It can be seen that HCS_{CD} values for B206 are much higher than A356. Since the time interval when hot tearing may develop is greater than the time available for the stress-relief process where liquid feeding occurs, hot tearing in B206 will be much more prevalent.

In this section, two hot tearing criteria have been used to compare the hot tearing susceptibility of B206 and A356 based on the experimentally obtained results. Both of them indicate that the B206 alloy is significantly more susceptible to hot tearing, whether the effects of mechanical phenomena or liquid feeding are considered.

The criteria by Langlais and Gruzleski, and Clyne and Davies were selected for analysis since they directly apply the experimental results. The results are assumed to be intuitive of other hot tearing criteria. Most of other ones also include a requirement to calculate the pressure drop occurring during semi-solid deformation or solidification shrinkage [5, 9]. In order to calculate the pressure drop in semi-solid materials, a numerical meso-scale model must be used. With the purpose of predicting the pressure drop as a result of deformation in semi-solid domains, and studying the effect of microstructure on hot tearing, a numerical multi-physics model is proposed. The results of the numerical simulations are presented and discussed in the next section.

6.2 Simulation Results

Multi-physics meso-scale simulations were performed on both the exploratory and microstructure models in order to investigate semi-solid deformation in a multi-physics context. The results of each model are shown and discussed in this section.

6.2.1 Exploratory Simulation Results

The purpose of the exploratory simulation was to better understand and determine the ability of the FSI implementation within Abaqus to model semi-solid deformations. The effect of liquid channel size on the flow behaviour during the deformation was studied as well. The results of the multi-physics simulation corresponding to a strain rate of 0.001s^{-1} applied to the semi-solid are shown in figures 6.16 and 6.17 to provide insight into the deformation behaviour when both the solid deformation and the liquid flow are coupled. Figure 6.16 (a) illustrates the contour plots of tensile stress (S_{xx}), i.e. the x -direction, in the solid. As the velocity is applied on this right side, the response to the load must be found within the liquid channels.

The simultaneous pressure distribution along the liquid channels is shown in Figure 6.16 (b). As portrayed, the liquid has moved to compensate for the applied solid deformation. This leads to a reduced pressure at the bottom of the domain. To maintain continuity, the variation in liquid pressure influences the stresses within the solid. Near the top side, the solid phase exhibits relatively low normal stresses, indicating a low traction force from the liquid, while the stress increases towards the bottom to compensate for the high negative liquid pressure.

Due to the variation in pressure within the liquid channel, the velocity components will also vary with spatial coordinates. As can be seen in Figure 6.18 (b), the velocity in the

y -direction (V_y) has a parabolic distribution in which the flow varies from zero at the fluid-solid boundaries to a maximum along the centerline of the channel. In addition, the velocity of the fluid boundary has to match the change in the structure displacement as a function of time.

Figure 6.17 (a) shows a linear gradient of velocity in the x -direction (V_x) moving from the left (stationary grain side) to the right (moving grain side). Figure 6.17 (c) shows the corresponding shear stress in the solid. As can be seen, there is a variation in shear stress from top to the bottom of the solid domain, which is a result of the variation in the slope of the V_y profile with distance. The existence of shear proves that the stress state is not uniaxial but has a combination of tensile and shear stresses in the x - y plane, which is the result of fluid flow in the liquid channel.

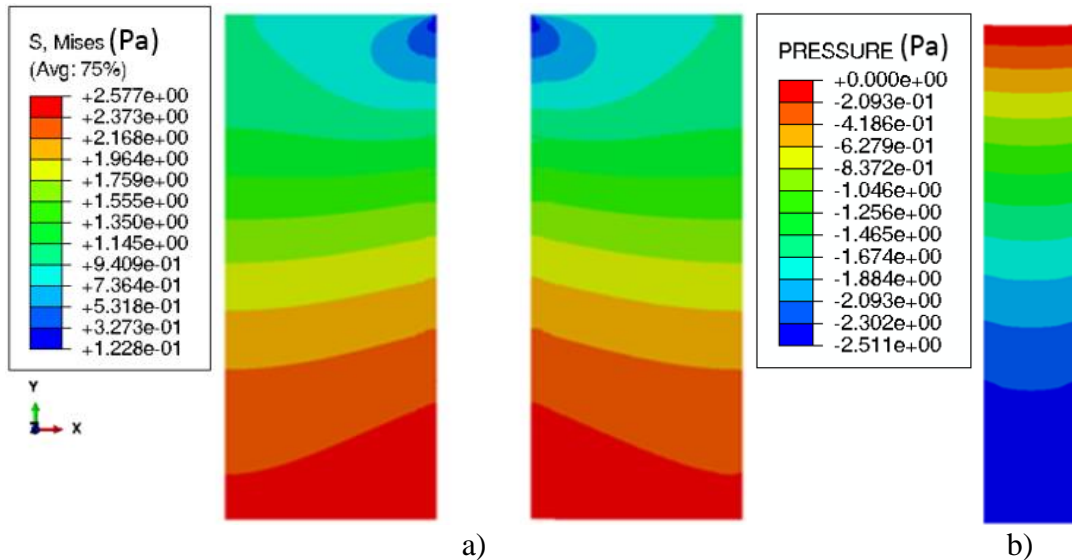


Figure 6.16 Contour plots of a) the solid grains stress in x -direction in Pa and b) The liquid pressure in Pa, with tensile displacement horizontal and to the right

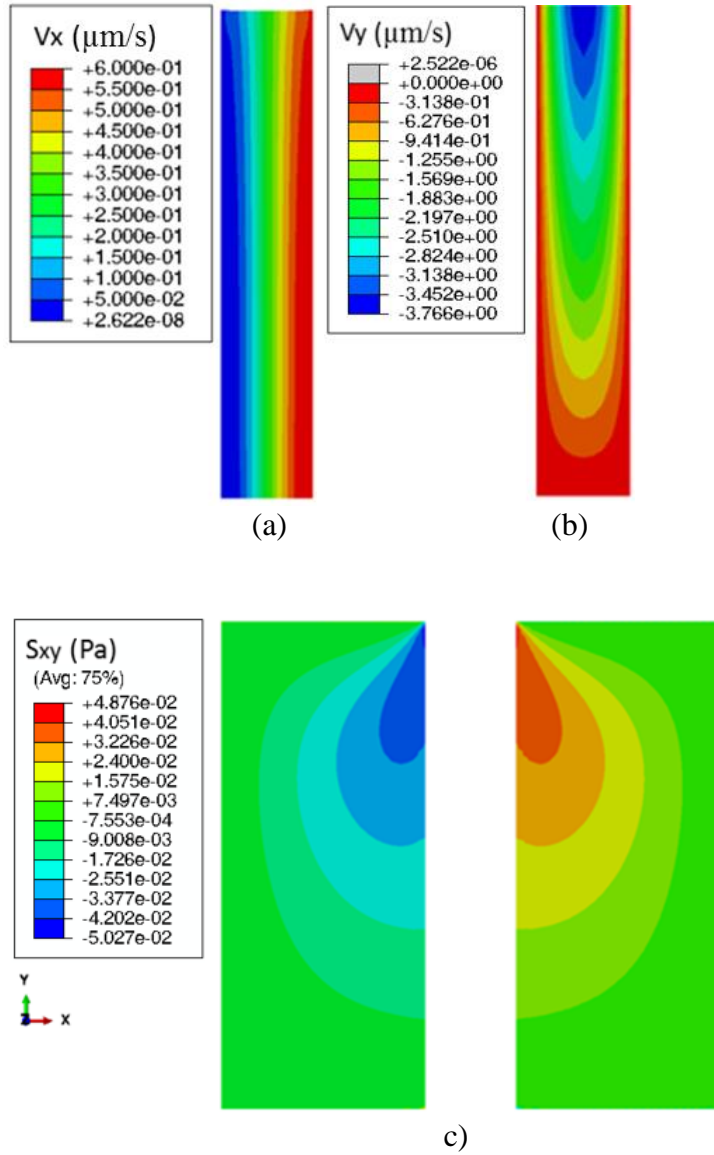


Figure 6.17 Contour plots of a) liquid velocity in the x-direction ($\mu\text{m/s}$), b) liquid velocity in the y-direction in ($\mu\text{m/s}$), c) solid grain shear stress in Pa with tensile displacement horizontal and to the right

A mesh sensitivity analysis was performed to study the effect of mesh size on the simulation results. Table 6.4 shows the liquid pressure drop based on the mesh size in both liquid and solid domains. The pressure drop over the length of the liquid channel from case 5 with the finest mesh was used as the characteristic value to assess mesh independence. As can be seen cases 4 and 5 result in similar liquid pressure drops, and thus a mesh size of 10 μm was determined to be adequate for the simulations.

The size of the liquid channel also plays a significant role in the magnitude of the pressure drop during deformation of the semi-solid domain. To study the effect of the liquid channel width on pressure drop, six models having increasing liquid channel width from 20 to 200 μm were created. The predicted gradient in pressure in the liquid channel for these six cases is shown in Figure 6.18 (black squares). As can be seen, when the channel is wider it is much easier for the liquid to flow to compensate the deformation. Thus, the pressure is closer to the gage pressure, with a value of zero. When the channel is small, larger pressure gradients form.

Model Validation: The six cases shown in Figure 6.18 also provide a metric for validating the simulations. Analytically, the resistance of a rectangular channel is determined using the Hagen–Poiseuille equation, in which for pressure-driven flow the relationship between the pressure drop ΔP and width of channel w can be approximated as

$$\Delta P = \frac{12L\mu Q}{h^3 w} \quad (6.1)$$

where Q is the flow rate in the channel, h is the thickness, L is the length, and μ is the viscosity of the channel liquid [59] Although the two-dimensional fluid flow in the simulations is driven by the applied deformation and the Hagen-Poiseuille equation provides

the resistance to flow, which results in a one directional fluid flow, it can be seen in Figure 6.18 that there is a good agreement between the simulation and analytical results

The next step is to simulate semi-solid deformation in B206 and A356 using the semi-solid microstructure model presented in Chapter 5.

Case	1	2	3	4	5
Elements size (μm)	40	30	20	10	5
Pressure drop (Pa)	1.36	1.70	2.07	2.51	2.55
Deviation from case 5 (%)	46.66	33.33	18.82	1.56	0

Table 6.4 Summary of mesh independence study for liquid and solid domains

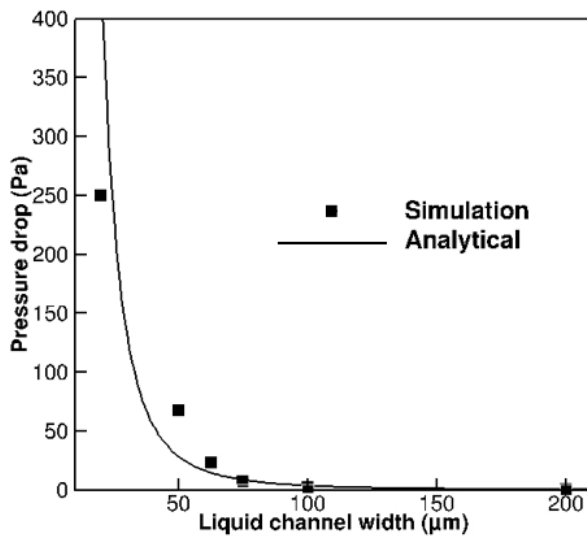


Figure 6.18 Comparison between simulations results (square data points) and analytical solutions (solid line) for the pressure drop versus the channel width

6.2.2 Microstructure Model Simulation Results

As explained in chapter 5, two different sets of microstructure model simulations were performed. The first was to study the effect of microstructure parameters on fluid flow and pressure drop in an isothermal and externally feedable microstructure domain. The second was to study the effectiveness of the FSI modules in predicting Gleeble test results, where the microstructure domain is not feedable. All the simulations carried out are summarized in Table 6.5.

Feeding State	Material	Grains Morphology	Fraction Solid
Feedable	B206	Globular	0.85
			0.90
			0.95
			0.98
Unfeedable	B206	Globular	0.85
			0.90
			0.95
			0.98
		Dendritic	0.85
			0.90
			0.95
			0.98
	A356	Dendritic primary +Eutectic	0.85
			0.90
			0.95
			0.98

Table 6.5 Different microstructure model domains characteristics

Feedable Globular Domain: As explained in Chapter 5, microstructure models approximating a feedable domain, where all the liquid channels are connected and flow occurs from a region having lower fraction solid, were developed. Four fraction solids between 0.85 and 0.98 were created and are shown in Figure 6.19. Solid grains and liquid channels are shown in gray and black, respectively. As can be seen, all the solid grains are surrounded by the liquid. By increasing the fraction solid, the size of liquid channels gets smaller. However, it should be noted that in the feedable domain, even at very high fraction solid, such as 0.98, there is a connected liquid path from the top to the bottom of the domain.

The FSI model outputs the stress in the solid as well as pressure distribution in the liquid. The model is able to show stress concentration sites, fluid flow and localization and liquid channels opening. For each microstructure model, the maximum strain (ϵ_{max}) is assumed to occur at the point when the model convergence limit was reached. Figure 6.20 shows the variation in the maximum strain with fraction solid for the feedable globular microstructure model. As can be seen, by increasing the fraction solid, the maximum strain decreases. In the feedable domain, the deformation is predominantly accommodated in the liquid phase, resulting in a decrease in ϵ_{max} with increasing the fraction solid - i.e. at higher solid fractions, the liquid channels are narrower which limits their ability to accommodate the strain.

Figures 6.21 to 6.24 show an example result from a microstructure model simulation, for a feedable case at fraction solid of 0.95 and a grain size of 100 μm . The model predicts the stress in the solid grains as well as the liquid pressure for three different levels of bulk strain ($\epsilon = \epsilon_{max}/10$, $\epsilon = \epsilon_{max}/2$, and $\epsilon = \epsilon_{max}$). The applied velocity boundary conditions on the

solid grains deform the domain in tension on both the left and right sides. This deformation is transferred to the liquid phase, changing the pressure within the liquid channels.

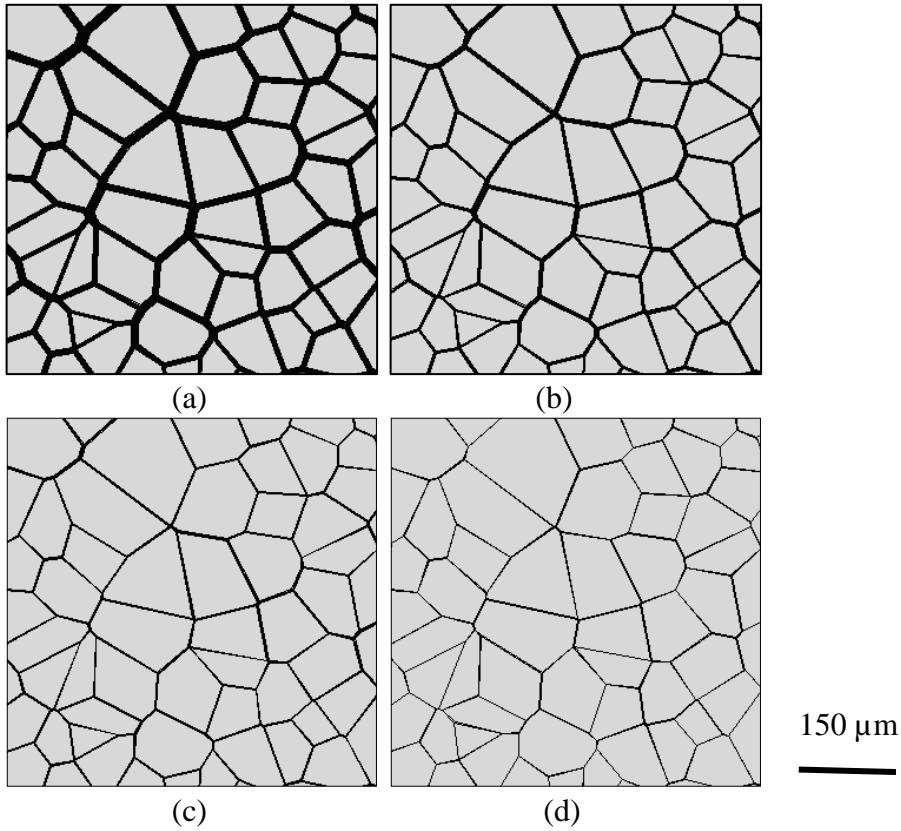


Figure 6.19 Sections of the feedable microstructure model domains at (a) $f_s=0.85$, (b) $f_s=0.90$, (c) $f_s=0.95$, and (d) $f_s=0.98$

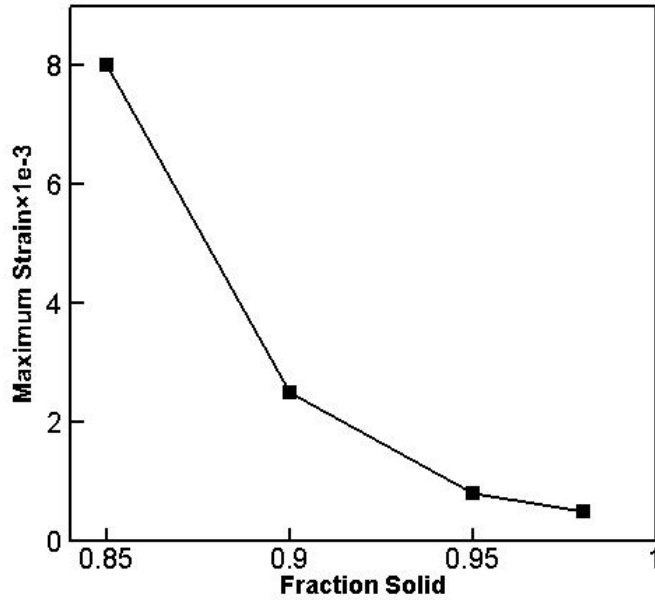


Figure 6.20 Maximum strain variation with the fraction solid in the feedable globular microstructure model

Considering that there is no continuous solid network from one side to the other side of the domain, stress in the solid grains develops as a result of the liquid pressure. During the deformation, the solid grains and the liquid channels move and interact with each other.

Contour plots of the velocity in the y -direction and the pressure within the liquid channels are shown in Figures 6.21 and 6.22 for each of the three different levels of bulk strain. Since the liquid channels are very fine, different subsections of the liquid are selected and magnified. These subsections are taken from the top, center, bottom, right, and left of the domain, and as shown in the overall view are named A, B, C, D, and E. Contour plots showing the x -direction component of stress on the solid grains and the Von Mises stress for each of the three different levels of bulk strain as well as the $\varepsilon=0$ state are given in Figures 6.23 and 6.24.

The initial state ($\varepsilon=0$) of the liquid velocity, liquid pressure, and solid grain stress is of course zero. With an increase in the bulk strain, all of the quantities increase. During the

deformation, first, when the strains are small, the liquid pressure is very small as well. As long as the pressure drop in the liquid is not in the range of the solid grains yield stress (7-15 MPa), the liquid pressure cannot plastically deform the solid grains. At small semi-solid bulk strains ($\varepsilon = \varepsilon_{\max}/10$), it can be seen that the fluid velocity increases on both sides of the liquid domain (D and E, Figure 6.21), which results in a pressure drop in the same regions (D and E, Figure 6.22) and subsequently stress development in the solid grains (Figures, 6.23 and 6.24). By increasing the strain to $\varepsilon = \varepsilon_{\max}/2$, and then finally to $\varepsilon = \varepsilon_{\max}$, larger regions of the domain are subjected to a pressure drop (Figure 6.22) and stress variation (Figure 6.23 and 6.24). Overall, fluid flow in the feedable domain is affected by the level of strain, the liquid channel size and the distance from the liquid source. Consequently, the pressure drop is smallest at the top (A, Figure 6.22) and largest at the base (C, Figure 6.22) of the domain, and the stresses are largest and smallest in these regions as well. It is also interesting to note the motion of the regions of highest stress, from the left and right surfaces at low strain to the center at high strain. This also shows the effect of feeding and the reduction in feeding with increased strain.

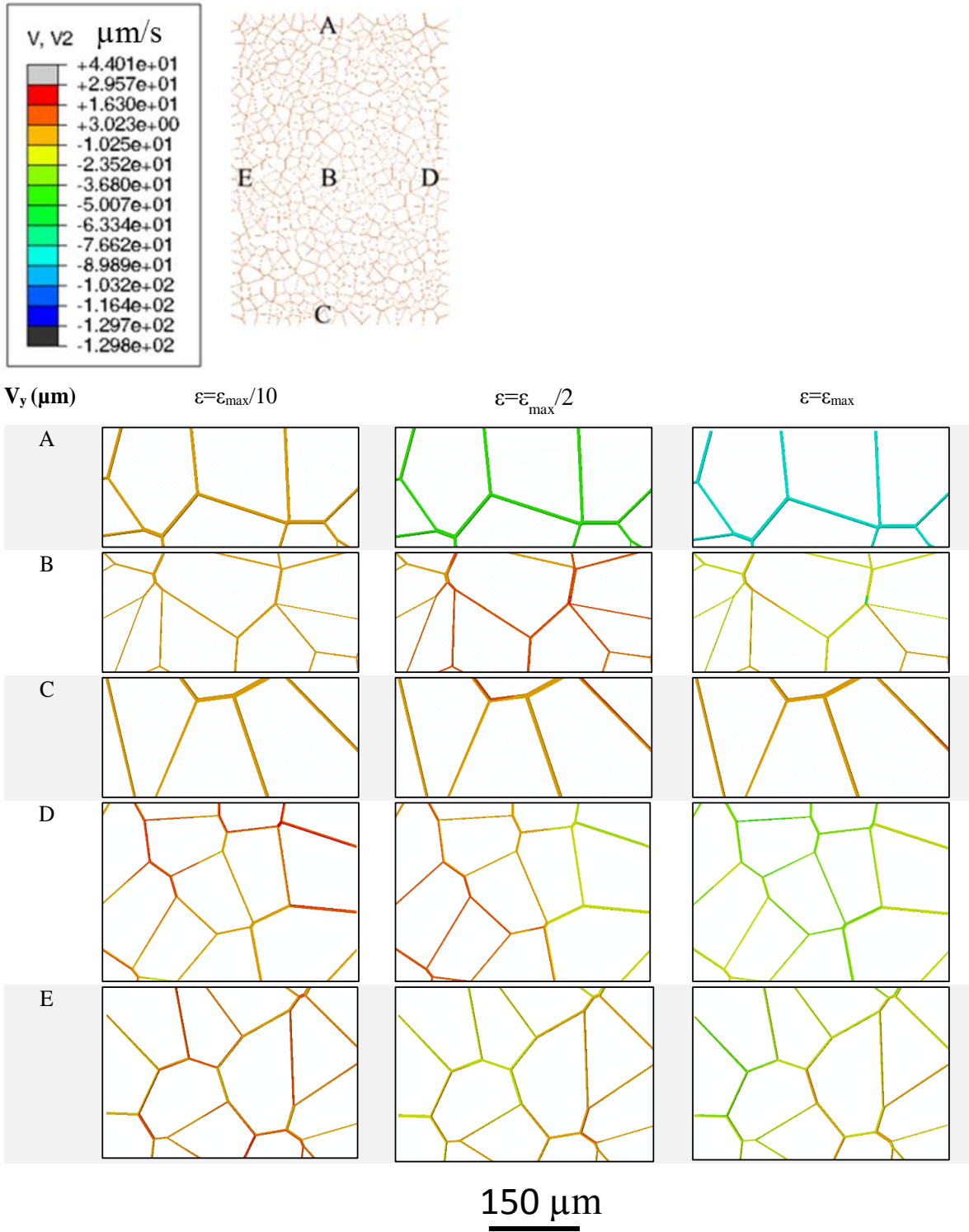


Figure 6.21 Contour plots of the liquid velocity in the y-direction in $\mu\text{m/s}$ for tensile deformation of the feedable B206 microstructure model at $f_s=0.95$ at $\epsilon=0$ (overall view of the domain), $\epsilon=\epsilon_{\text{max}}/10$, $\epsilon=\epsilon_{\text{max}}/2$ and the final state $\epsilon=\epsilon_{\text{max}}$. Subsections A, B, C, D, and E are taken from the top, center, bottom, right and left of the domain, respectively.

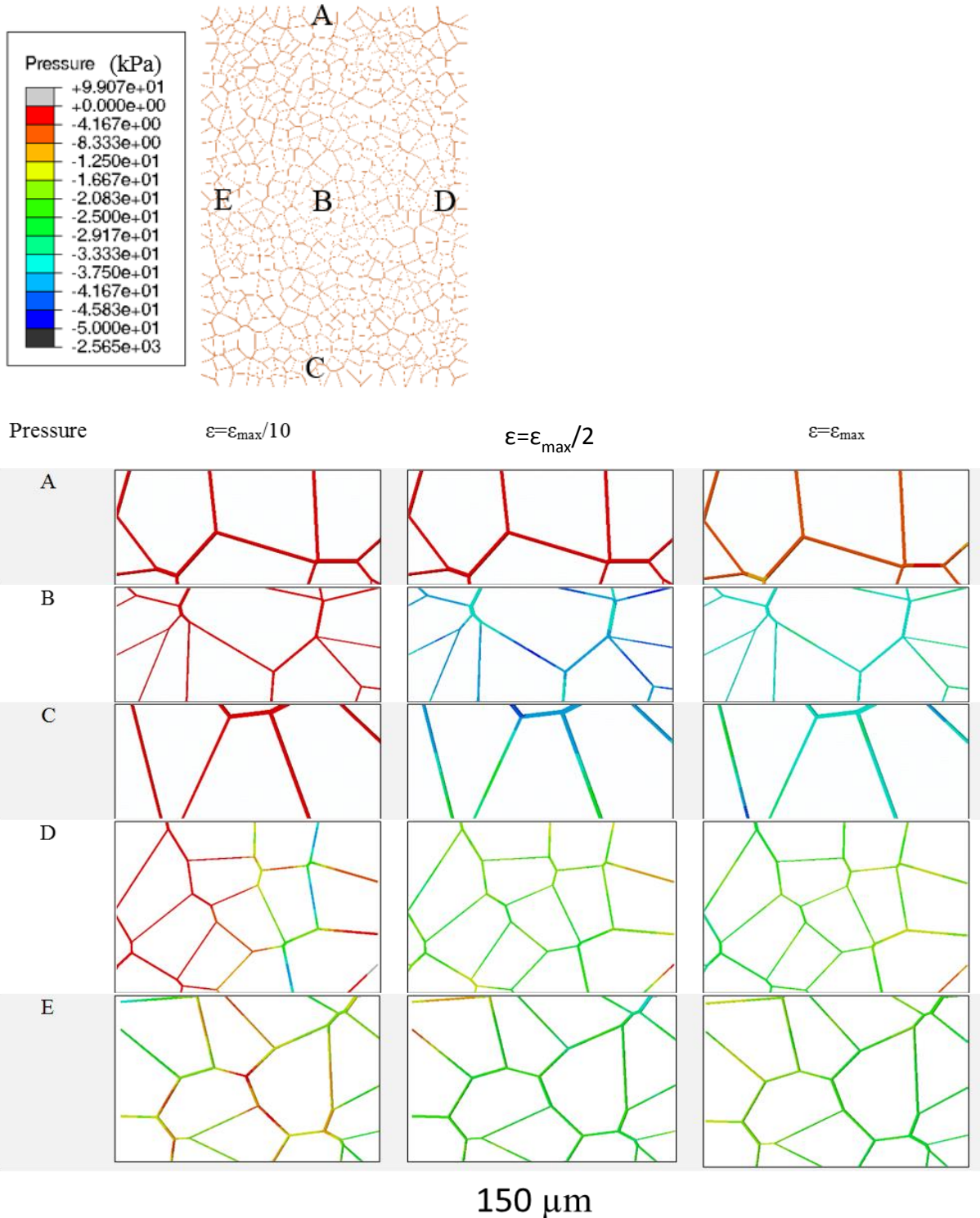


Figure 6.22 Contour plots of the liquid pressure in kPa for tensile deformation of the feedable B206 microstructure model at $f_s=0.95$ at $\varepsilon=0$ (overall view of the domain), $\varepsilon=\varepsilon_{\max}/10$, $\varepsilon=\varepsilon_{\max}/2$ and the final state $\varepsilon=\varepsilon_{\max}$. Subsections A, B, C, D, and E are taken from the top, center, bottom, right and left of the domain, respectively.

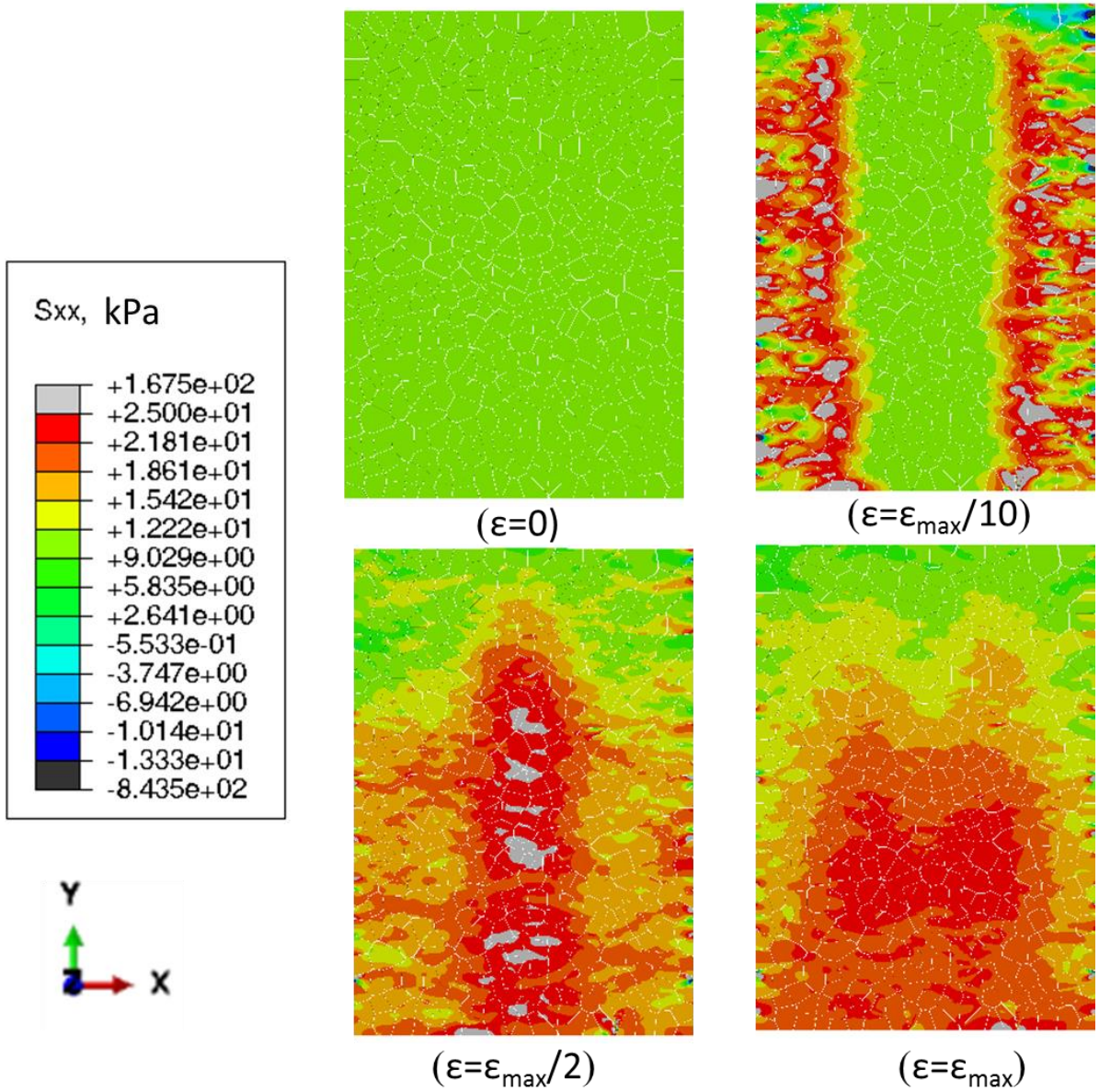


Figure 6.23 Contour plots of the stress in the x -direction in kPa for tensile deformation of the feedable B206 microstructure model at $f_s=0.95$ at $\epsilon=0$, $\epsilon=\epsilon_{\max}/10$, $\epsilon=\epsilon_{\max}/2$ and the final state $\epsilon=\epsilon_{\max}$

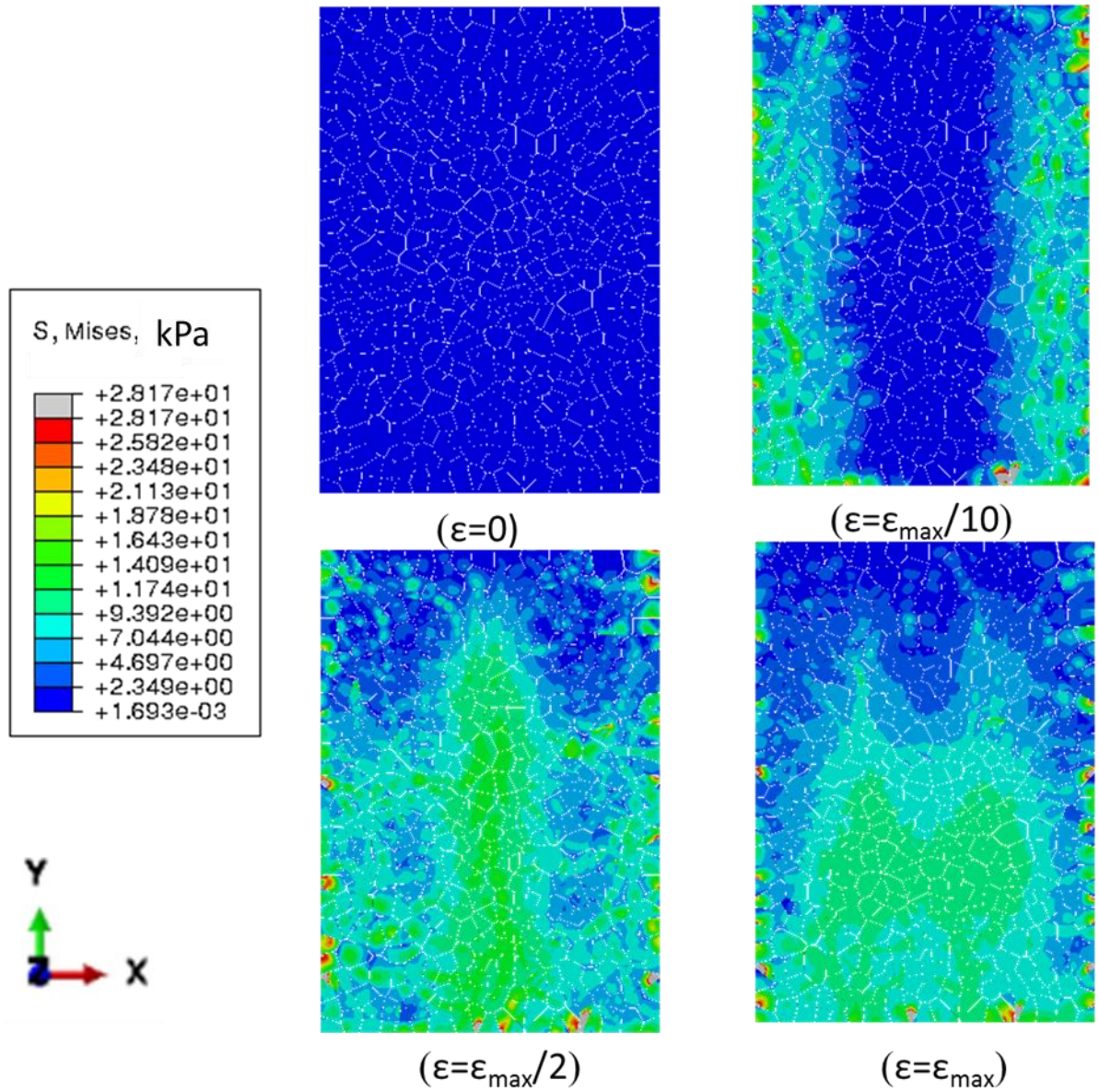


Figure 6.24 Contour plots of the Von Mises stress in kPa for tensile deformation of the feedable B206 microstructure model at $f_s=0.95$ at $\epsilon=0$, $\epsilon=\epsilon_{\max}/10$, $\epsilon=\epsilon_{\max}/2$ and the final state $\epsilon=\epsilon_{\max}$

Since the deformation velocity remains constant, during the simulation, the overall strain increases linearly with time. The average pressure drop at each time step was calculated and plotted versus strain for different fraction solids as shown in Figure 6.25. By increasing the strain from its initial state ($\varepsilon = 0$), first the pressure drops sharply because of high applied momentum, and then by increasing the strain, at relatively high fraction solids such as 0.95 and 0.98, the pressure slowly increases with strain till the maximum strain point at which the liquid elements get too distorted and the fluid model diverges. However, at relatively low fraction solids such as 0.85 and 0.90 after the initial pressure drop, the pressure gradually increases as a result of feeding. This is more obvious at $f_s=0.85$ where good feeding increases the pressure to values near zero. As can be seen, the pressure drop in the liquid is highly fraction solid dependent. By increasing the fraction solid from 0.85 to 0.98, the average pressure drop increases from 0.07 to 1.8 kPa.

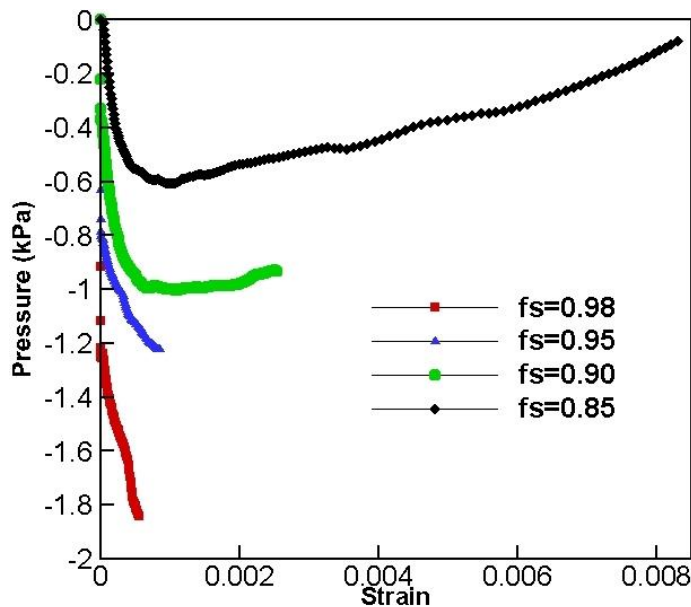


Figure 6.25 Effect of strain and fraction solid on the pressure drop in the feedable B206 microstructure domains

Unfeedable Domain: As shown in Table 6.6, unfeedable microstructure models approximating globular and dendritic B206 were created, as well as domains for A356 with the primary and eutectic constituent, for the range of fraction solid of between 0.85 and 0.98. The overall semi-solid deformation behaviour and pressure drop in the liquid channel at each fraction solid greatly depend on both the structure of the solid grains and the size and morphology of the liquid channels.

Globular B206: The globular microstructure consists of primary B206 grains that are surrounded by the liquid channels. As explained in Chapter 5, for the unfeedable microstructure domain, when the width of the liquid channel is smaller than 3 μm , solid grains were assumed to coalesce *i.e.* the liquid channel was eliminated. Figure 6.26 shows sections of the unfeedable globular B206 domain, at fraction solids between 0.85 and 0.98. It can be seen that a few grains are connected at a fraction solid of 0.85 and by increasing the fraction solid the number of connected grains and isolated pockets increase. At $f_s=0.85$ most of the grains are surrounded by the liquid channels however at $f_s=0.98$ there is a large number of connected grains and some liquid channels which are surrounding only a few grains.

Figure 6.27 shows the variation of the maximum strain with the fraction solid for the unfeedable globular microstructure model. As can be seen, by increasing the fraction solid, from 0.85 to 0.90 the maximum strain decreases, with a further increase in the fraction solid, the maximum strain increases. In the unfeedable domains, since there are percolated solid grains, the deformation is accommodated more evenly by both the liquid phase and solid grains. At relatively low fraction solids, (0.85-0.90), the fluid flow effect is more dominant, limiting ε_{max} . At solid fractions greater than 0.90, the solid grains become percolated and a larger number of grains accommodate the strain which result in an increase in ε_{max} .

Figure 6.28 shows contour plots of the Von Mises stress in solid grains of globular B206 at fraction solids of 0.95, for different strains from 0 to the maximum strain, (ϵ_{max}). As can be seen, in the initial state ($\epsilon = 0$), stress is zero in the whole domain, however, by increasing the strain from 0 to $\epsilon_{max}/10$ and then to $\epsilon_{max}/2$, stress develops due to the applied displacement, fluid flow, and the grains deformation. The maximum Von Mises stress is seen to increase to the input plastic yield stress value. In the regions where stress reaches the maximum stress, the solid grains start to deform plastically. As can be seen, the stress in the percolated grains is significantly higher than its value in the other grains. The percolated grains transmit the load from the sides to the center of the domain, which causes the grains yielding. However, the stress values are very low in the grains surrounded by liquid which do not result in yielding of these grains. The reason is that the liquid phase can flow easily, so, during semi-solid deformation, the liquid phase compensates the deformation.

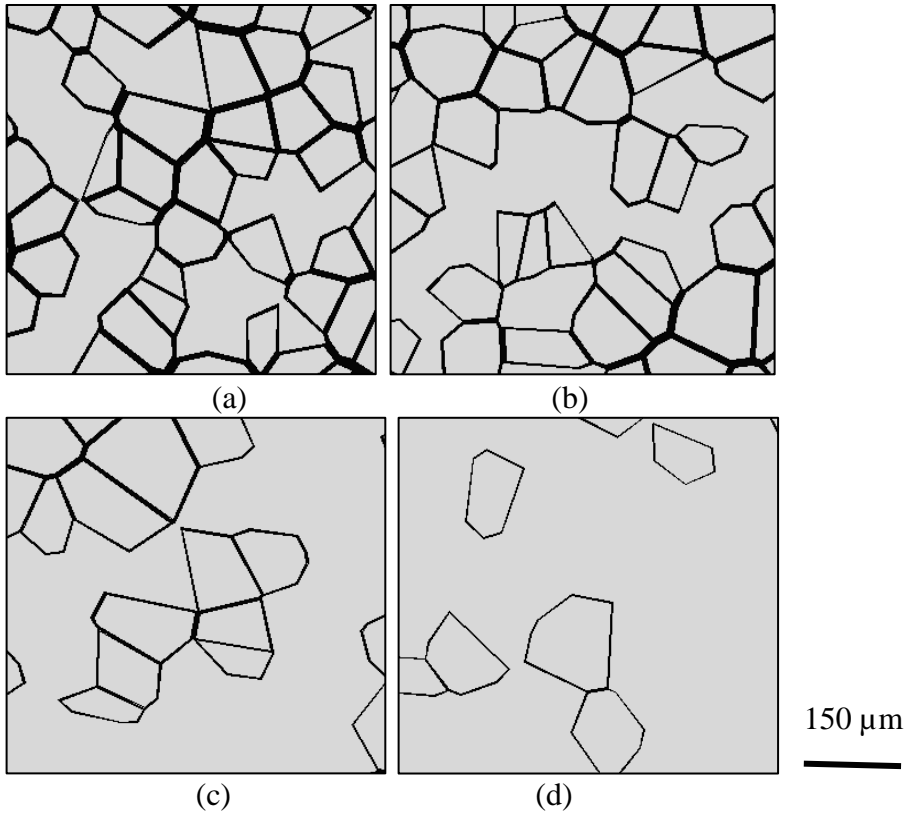


Figure 6.26 Sections of the unfeedable granular B206 microstructure model domains at (a) $f_s=0.85$, (b) $f_s=0.90$, (c) $f_s=0.95$, and (d) $f_s=0.98$

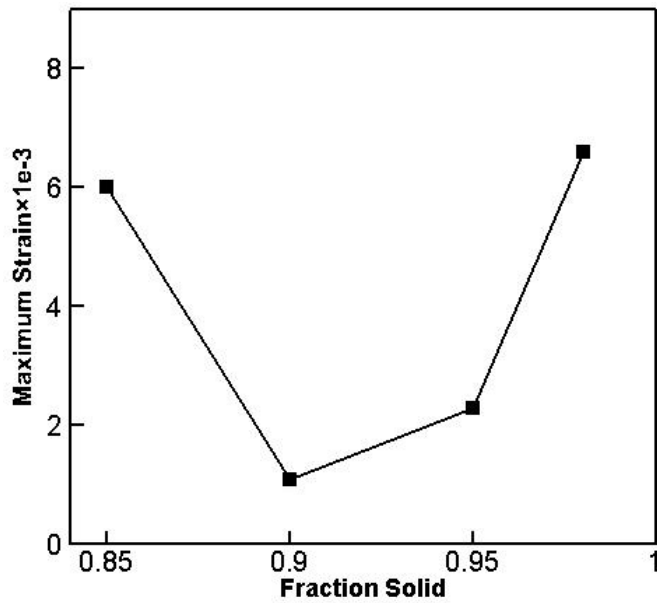


Figure 6.27 Maximum strain variation with the fraction solid in the unfeedable globular microstructure model

As shown in the feedable domain, the stress developing within the solid grains is very low, as a result of the liquid channel and high permeability of the domain. In contrast, in the unfeedable domains, where solid grains have percolated, the permeability is very limited which results in high pressure drop as well as high stress values in the solid grains.

As in the feedable domain cases, the applied deformation velocity was constant in the unfeedable domain simulations. Figure 6.29 plots the average pressure drop at each time step as a function of total strain for different fraction solids. As can be seen, the liquid pressure drop is highly fraction solid dependent. At fraction solids of 0.85 and 0.98, the amount of pressure drop is small, which results in large maximum strains (ϵ_{\max}). However, ϵ_{\max} values are quite a bit lower for fraction solids of 0.90 and 0.95. The unfeedable B206 microstructure domain has higher pressure drop than the feedable B206 microstructure domain, for example, the unfeedable case has the highest pressure drop (around 260 kPa) at a fraction solid of 0.95. The pressure drop for the feedable case at fraction solid of 0.95 is shown to be 1.22 kPa.

Figure 6.30 shows the overall stress-strain curve of the semi-solid for unfeedable B206. As can be seen, at all fraction solids, the stress first increases quickly, then reaches a maximum value which can be termed the semi-solid yield stress, then increases gradually as a result of geometric strain hardening [87]. As expected, by increasing the fraction solid, the semi-solid yield stress increases. For example, by increasing the fraction solid from 0.85 to 0.98, the calculated yield stress increases from 0.35 to 10.2 MPa.

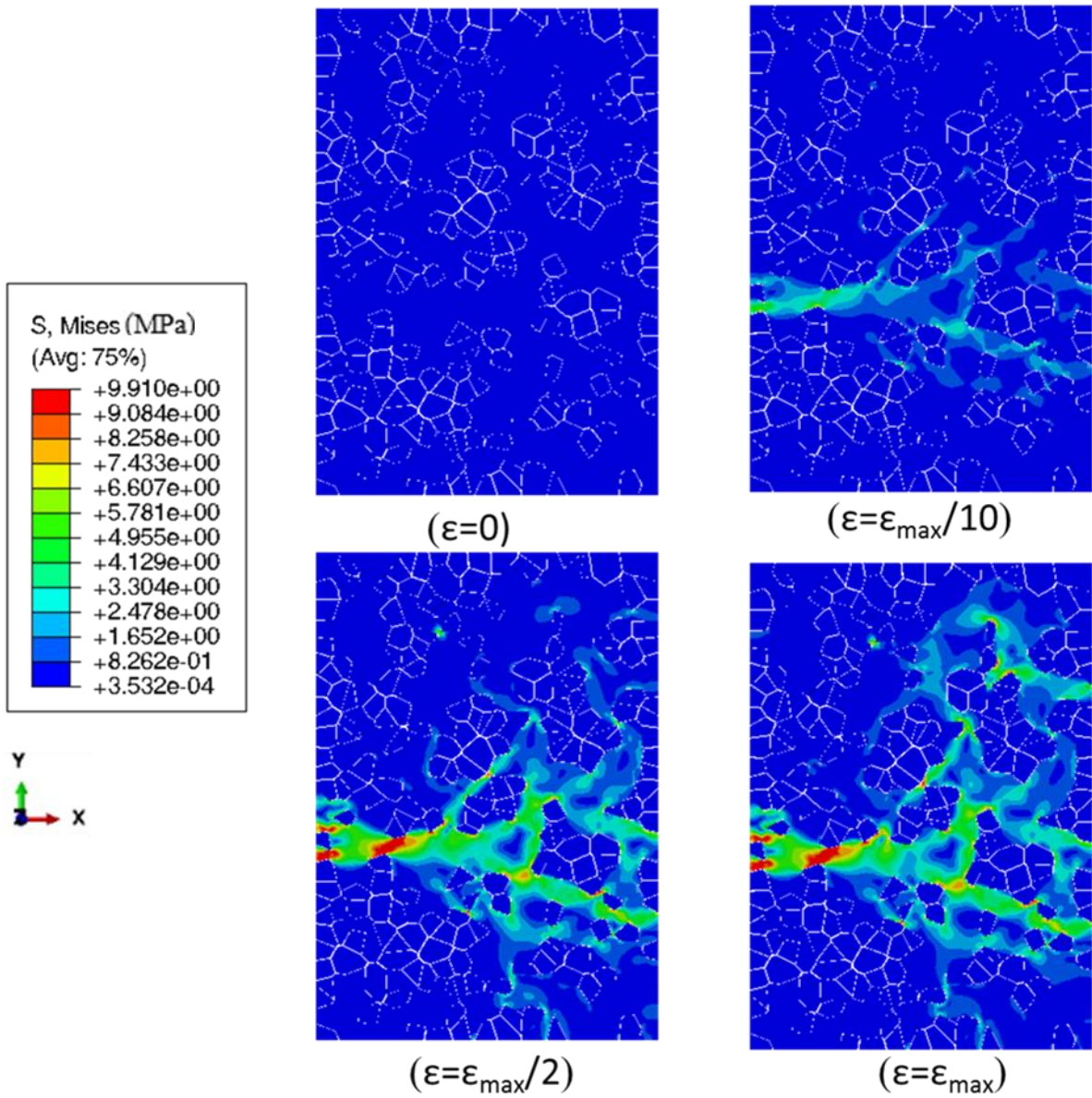


Figure 6.28 Contour plots of the solid grains Von Mises stress in MPa for tensile deformation of the unfeedable globular B206 microstructure model at $f_s=0.95$, at $\epsilon=0$, $\epsilon=\epsilon_{max}/10$, $\epsilon=\epsilon_{max}/2$, and ϵ_{max}

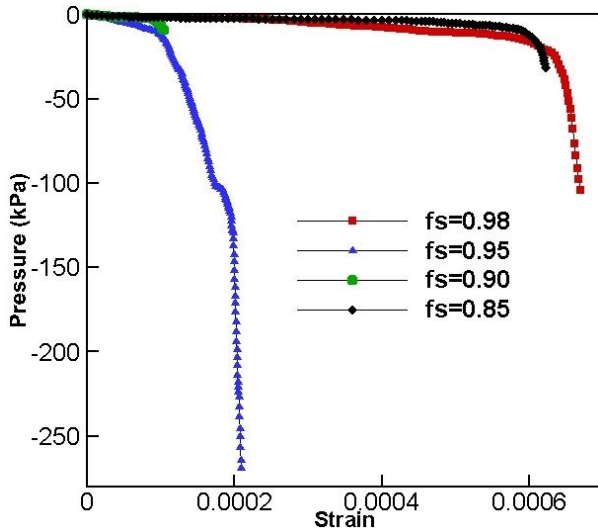


Figure 6.29 Effect of strain and fraction solid on the average pressure drop in the unfeedable globular microstructure domains

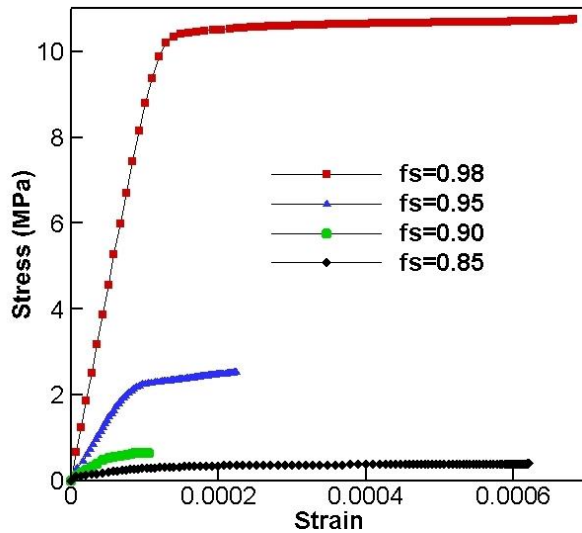


Figure 6.30 Effect of strain and fraction solid on the stress-strain curves of the unfeedable globular microstructure domains

Dendritic B206: The dendritic microstructure consists of clover-leaf shaped primary B206 phases which are surrounded by the liquid channels. In contrast to the globular grains, the dendritic morphology results in a solid network with less elongated isolated liquid pockets for the same fraction solids. Figure 6.31 shows sections of the unfeedable dendritic domain at fraction solids between 0.85-0.98. It can be seen that, at all fraction solids, the

liquid channels are isolated and present as liquid pockets. By increasing the fraction solid from 0.85 to 0.98, the size and number of the liquid pockets decrease. For each microstructure model, the maximum strain (ϵ_{max}) is assumed to occur at the point when the model reaches the convergence limit. Figure 6.32 shows the variation of the maximum strain with the fraction solid for the unfeedable dendritic microstructure model.

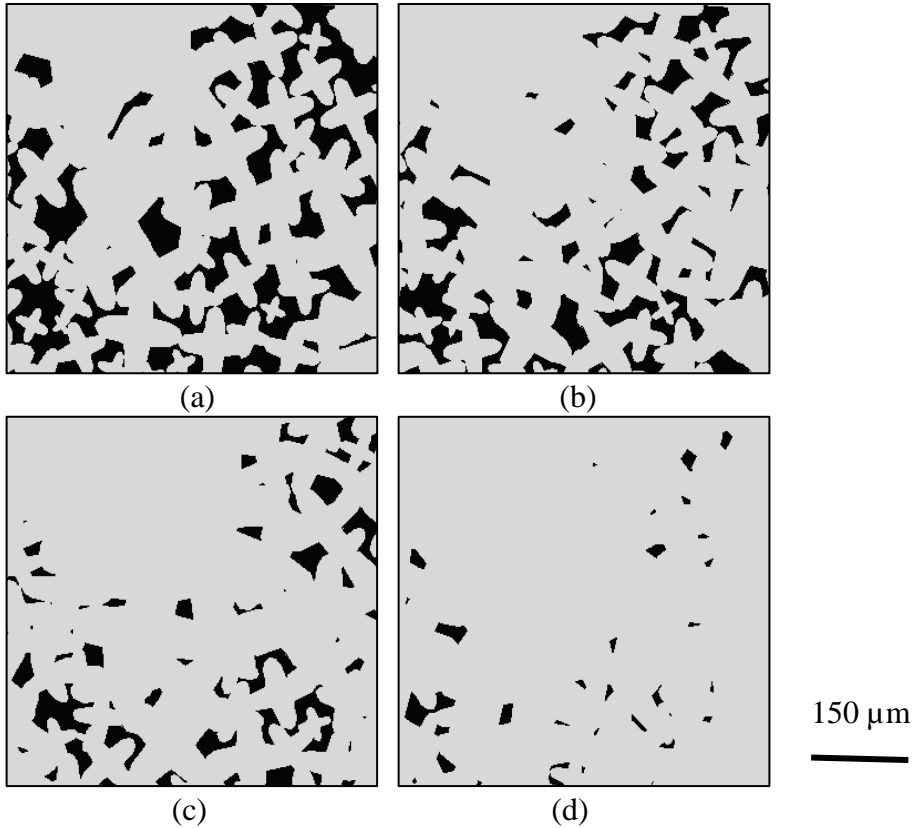


Figure 6.31 Sections of the unfeedable dendritic B206 microstructure model domains at (a) $f_s=0.85$, (b) $f_s=0.90$, (c) $f_s=0.95$, and (d) $f_s=0.98$

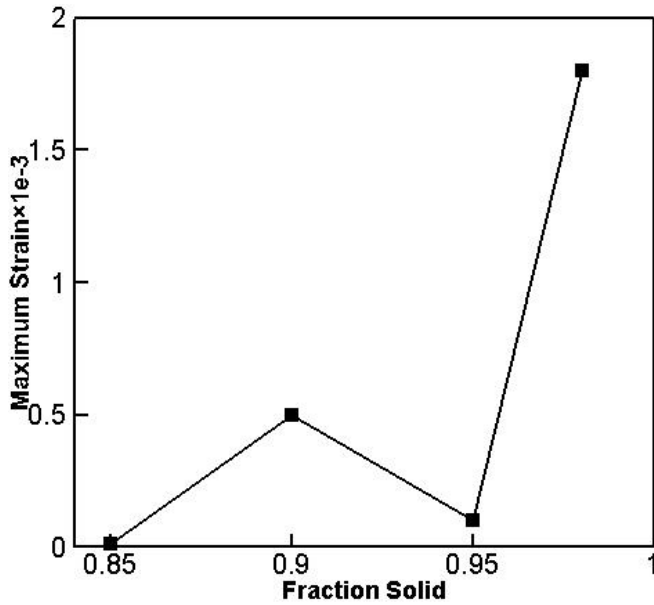


Figure 6.32 Maximum strain variation with the fraction solid in the unfeedable dendritic microstructure model

Figure 6.33 shows the Von Mises stress in the solid grains for dendritic B206 at fraction solids of 0.95. As can be seen, in the initial state ($\varepsilon = 0$), the stress is zero in the whole domain, however, as shown in $\varepsilon = \varepsilon_{\max}/10$, $\varepsilon = \varepsilon_{\max}/2$, and the final state ($\varepsilon = \varepsilon_{\max}$), there is considerable stress in-homogeneity and localization. In the dendritic solid grains, the maximum Von Mises stress increases to the input plastic yield stress value, similar to what was seen in the globular microstructure (Figure 6.28). In the regions where stress reaches the maximum value, the solid grains start to deform plastically. It can be seen that the Von Mises stress values are very small in the areas that undergo large deformation in the grain boundaries/liquid section. In comparison with the globular B206 microstructure model, the results of the dendritic simulations show that stress is developed over a greater area of the dendritic domain and the areas where the deformation in the solid is compensated with the fluid flow are smaller. In the dendritic domain with small liquid pockets that are isolated, the liquid pressure drops to very low values.

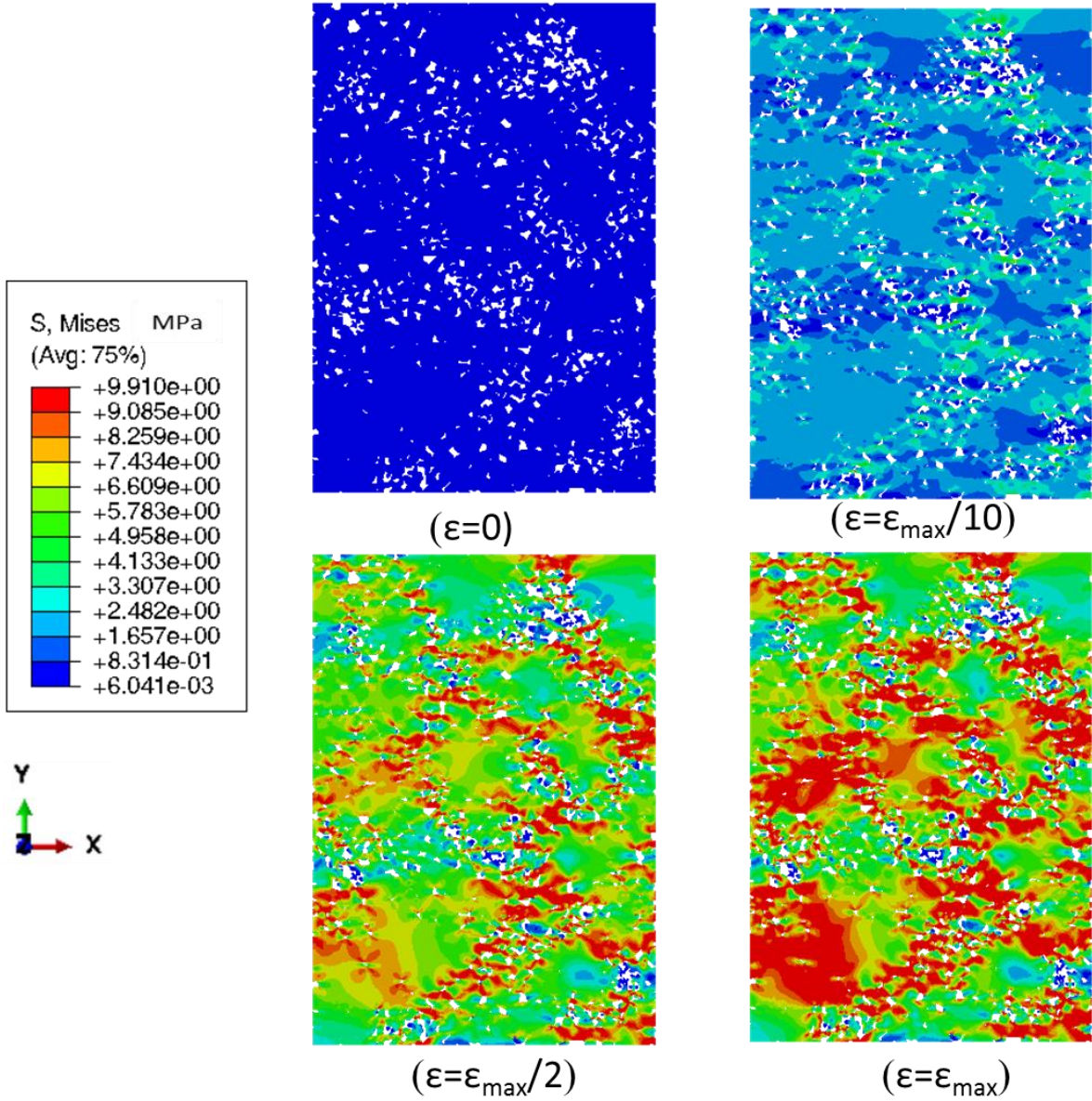


Figure 6.33 Contour plots of the solid grain Von Miss in MPa at $f_s=0.95$ of the unfeedable dendritic B206 microstructure model at $f_s=0.95$, at $\epsilon=0$, $\epsilon=\epsilon_{\max}/10$, $\epsilon=\epsilon_{\max}/2$, and ϵ_{\max}

The average pressure drop at each time step was calculated and plotted versus strain for different fraction solids of dendritic microstructure domains, as shown in Figure 6.34. It also shows that the amount of liquid pressure drop is highly fraction solid dependent. At fraction solids of 0.90 and 0.98, the pressure drop is smaller than the pressure drop at fraction solids of 0.85 and 0.95 which results in relatively large maximum strains (ϵ_{max}). ϵ_{max} values are very small for fraction solids of 0.85 and 0.95. The unfeedable dendritic microstructure domain has the highest pressure drop (around 1200 kPa) at a fraction solid of 0.85. However, in the globular microstructure domain, the highest pressure drop was reported to be ~ 260 kPa at a fraction solid of 0.95. The comparison of the globular and dendritic microstructure is discussed later in this chapter.

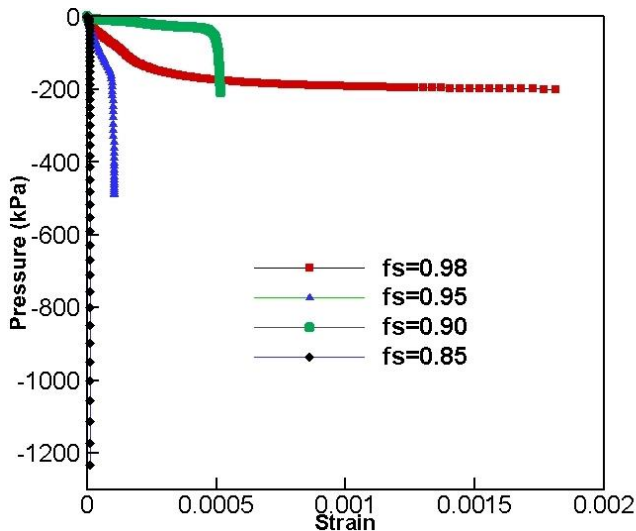


Figure 6.34 Effect of strain and fraction solid on the average pressure drop in the unfeedable dendritic microstructure domains

Figure 6.35 shows the effect of the applied strain on the semi-solid bulk stress values for unfeedable B206. As can be seen, at all fraction solids by increasing the strain, the stress increases and after reaching a maximum value (semi-solid yield stress), increases gradually as a result of geometric strain hardening. As expected, by increasing the fraction solid, the

semi-solid yield stress increases. For example, by increasing the fraction solid from 0.85 to 0.98, the calculated yield stress increases from 0.79 to 15.6 MPa.

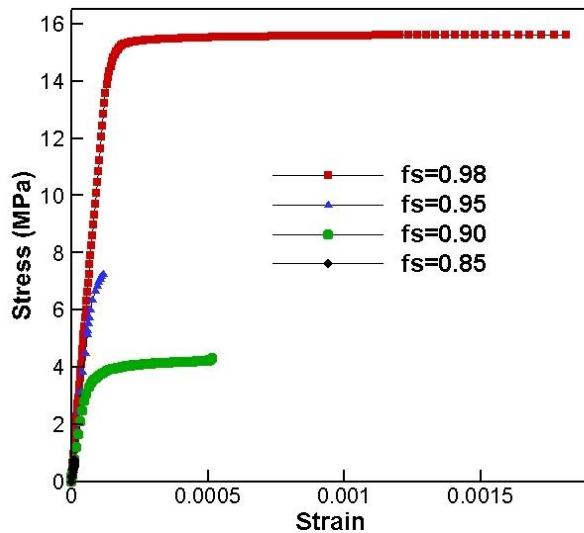


Figure 6.35 Effect of strain and fraction solid on the stress-strain curves of the unfeedable dendritic microstructure domains

A356: The semi-solid deformation of A356 as an alloy with a large amount of eutectic is described in this section. For these simulations, microstructure model domains containing clover-leaf shaped primary and circular eutectic components, as explained in Chapter 5, were created. Figure 6.36 shows sections of the A356 domain at fraction solids between 0.85 and 0.98. It can be seen that by increasing the fraction solid from 0.85 to 0.99, the primary phase fraction solid remains constant and only the eutectic constituent fraction increases which lead to narrower liquid channels. For each microstructure model, the maximum strain (ϵ_{max}) is measured when the model reaches the convergence limit. Figure 6.37 shows the variation of the maximum strain with the fraction solid for the unfeedable A356 microstructure model. Primary grains, eutectic and liquid are shown in light gray, dark gray, and black, respectively.

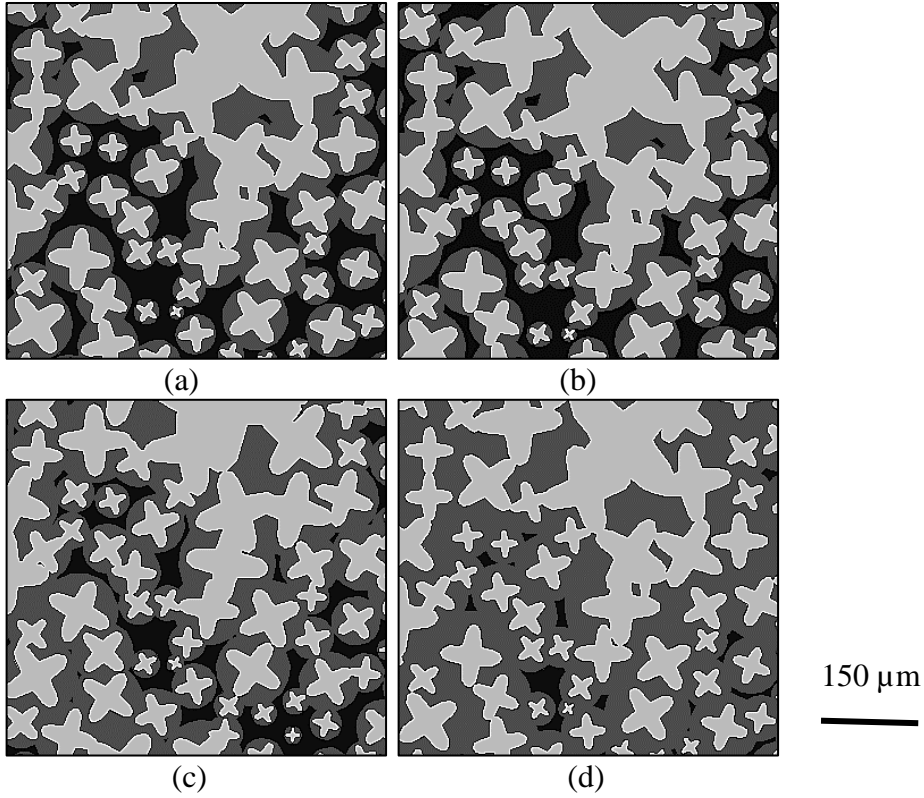


Figure 6.36 Sections of the unfeedable A356 microstructure domains at (a) $f_s=0.85$, (b) $f_s=0.90$, (c) $f_s=0.95$, and (d) $f_s=0.98$

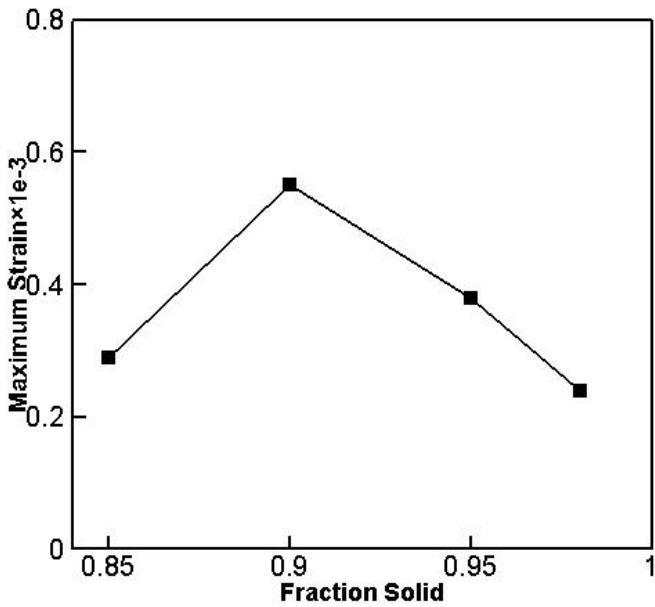


Figure 6.37 Maximum strain variation with the fraction solid in the unfeedable A356 microstructure model

Figure 6.38 shows the Von Mises stress in solid grains for A356 at a solid fraction of 0.95. As can be seen, in the initial state ($\varepsilon = 0$), stress is zero in the whole domain, however, as shown in $\varepsilon = \varepsilon_{\max}/10$, $\varepsilon = \varepsilon_{\max}/2$, and the final state ($\varepsilon = \varepsilon_{\max}$), there is considerable stress inhomogeneity and localization. Due to the existence of the eutectic, similar to the dendrite structure, almost all of the liquid channels are isolated; however, because of the smooth surface of the eutectic part, the isolated pockets are larger and more elongated than in the dendritic microstructure domain.

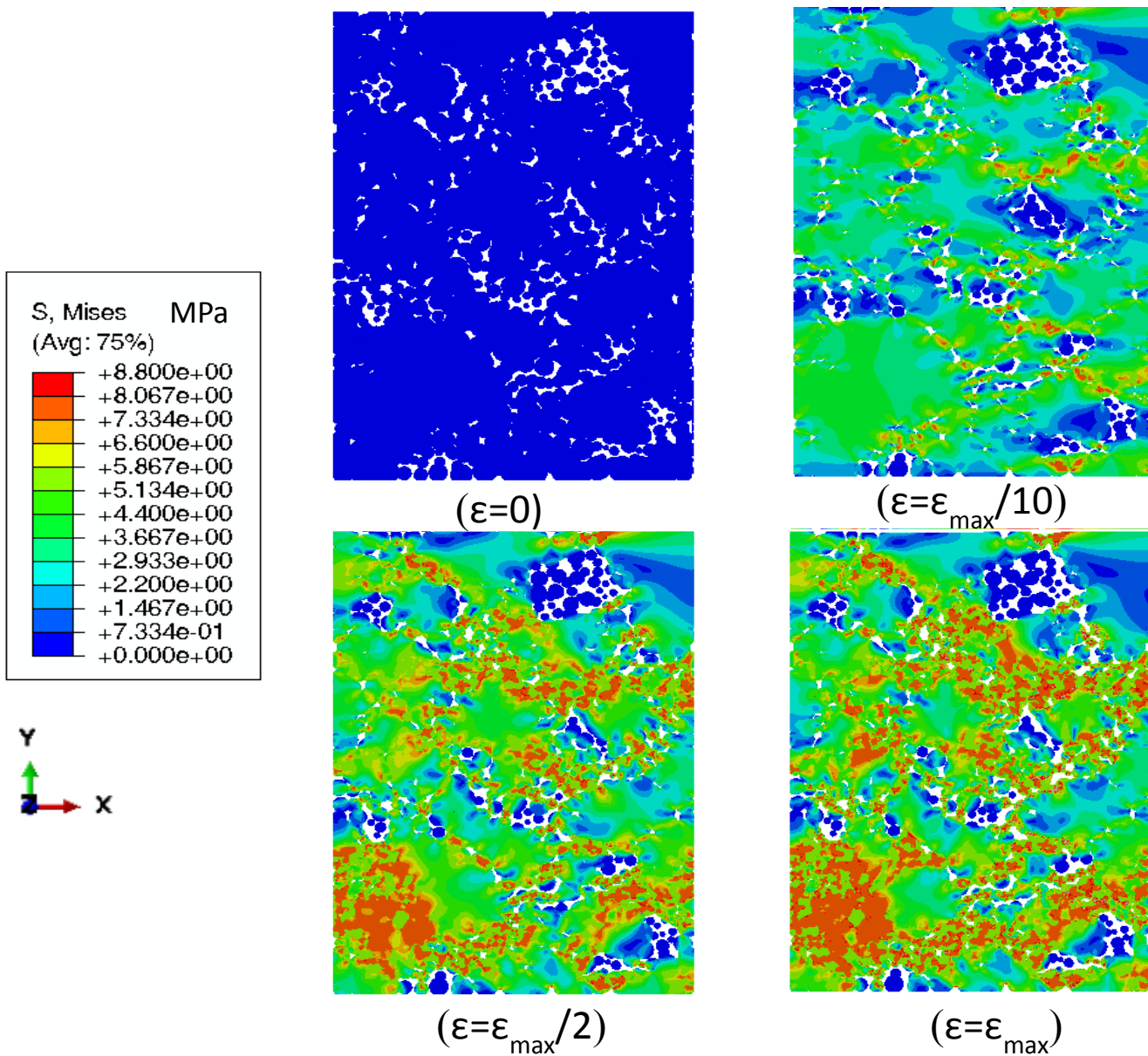


Figure 6.38 Contour plots of the Von Miss in MPa for tensile deformation of the unfeedable A356 microstructure model at $f_s=0.95$ at $\epsilon=0$, $\epsilon=\epsilon_{\max}/10$, $\epsilon=\epsilon_{\max}/2$ and the final state $\epsilon=\epsilon_{\max}$

The average pressure drop at each time step was calculated and plotted versus strain for different fraction solids as shown in Figure 6.39. The pressure drop in the liquid is highly fraction solid dependent. At fraction solids of 0.85 and 0.90, the amount of pressure drop is small which results in large maximum strains (ϵ_{\max}). ϵ_{\max} values are larger for fraction solids of 0.90 and 0.95. The unfeedable A356 microstructure domain has highest pressure drop (around 100 kPa) at fraction solid of 0.85.

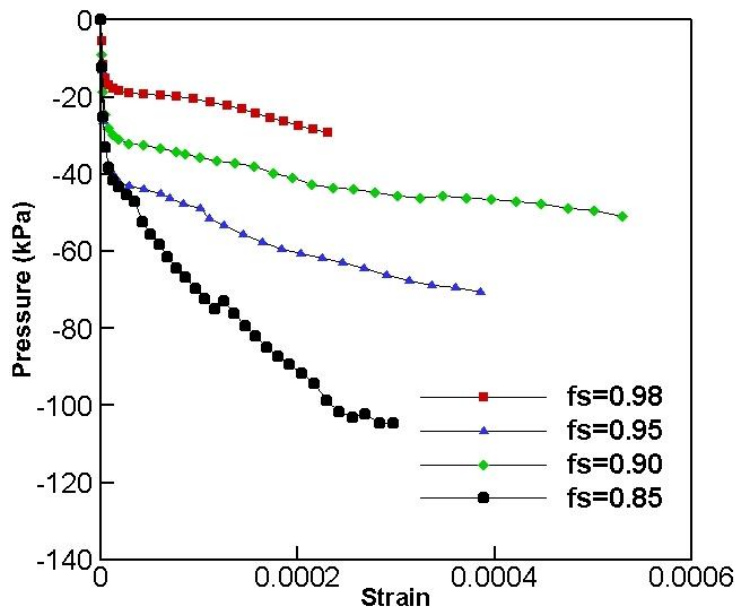


Figure 6.39 Effect of strain and fraction solid on the average pressure drop in the unfeedable A356 microstructure model domains

Figure 6.40 shows the effect of the applied strain on the semi-solid bulk stress values for the unfeedable A356 microstructure. As can be seen, at all fraction solids, by increasing the strain, the stress increases and after reaching a maximum value (semi-solid yield stress), increases gradually as a result of geometrical strain hardening. As expected, by increasing the fraction solid, the semi-solid yield stress increases. For example, by increasing the fraction solid from 0.85 to 0.98, the calculated yield stress increases from 0.48 to 8.46 MPa.

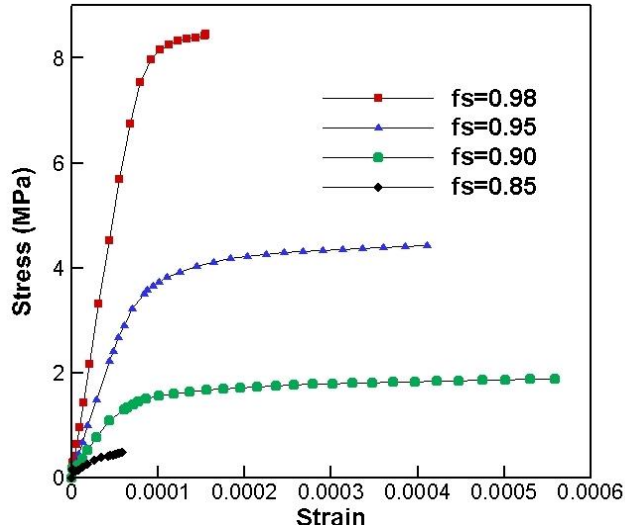


Figure 6.40 Effect of strain and fraction solid on the stress-strain curves of the unfeedable A356 microstructure model domain

6.2.3 Discussion of the Numerical Results

In this section, the microstructure model results are compared and discussed. First, in order to show the effect of feeding, the pressure drop and corresponding maximum strain of the feedable and unfeedable globular B206 domains are compared and contrasted. Then, with the intention of studying the effect of microstructure and liquid channel morphology, the two unfeedable microstructure model domains, globular and dendritic B206, are compared. Finally, the dendritic B206 and A356 microstructures are examined in order to address the effect of the eutectic constituent.

Feedable and Unfeedable Globular B206 microstructure models Comparison: Table 6.7 summarizes the final state of the feedable and unfeedable globular B206 microstructure models, specifically, the maximum bulk strain (ϵ_{\max}) and the corresponding average final pressure drop at fraction solids between 0.85-0.98.

Examining the table, it can be seen that the pressure drop is quite small in the feedable domain, due to the existence of a liquid source that provides fluid to respond to the

pressure drop. However, in the unfeedable domain, with all surfaces closed, there is no external feeding and as a result, the pressure drops significantly during tensile deformation. During the simulation, the flow and redistribution of the liquid to compensate the deformation are hindered by the morphology of the liquid channels and the dense packing of the grain structure. Comparing the two sets of simulations, the table shows that the predicted pressure drop values in the feedable cases are 1 or 2 orders of magnitude smaller than the pressure drop in the unfeedable cases. The pressure drop is also seen to be dependent on the fraction solid. In the feedable domain, the pressure drop is very small at lower fraction solids such as 0.85. With an increase in the fraction solid, the liquid channels get narrower, as a result, the permeability becomes limited and pressure drop increases. In the unfeedable case, the thickness of the liquid channel and the number of the percolated grains both affect the pressure drop. In the unfeedable globular domain, there is a similar trend that by increasing the fraction solid from 0.85 to 0.95, and 0.98, the pressure drop increases. However, it increases much more rapidly than the feedable case, and becomes quite large at a fraction solid of 0.95. Interestingly, the pressure drop then decreases at a fraction solid of 0.98. This is due to the fact that the solid structure has now largely percolated.

In the feedable case, at relatively low fraction solids such as 0.85 and 0.90, the permeability of the domain is high which results in high maximum strains (8×10^{-3} and 2.5×10^{-3} , respectively). In these cases, the continuous liquid compensates the deformation. The maximum strains for the unfeedable case at same values of fraction solid are 6×10^{-3} and 1.1×10^{-3} , respectively. However, at high fraction solids (0.95 and 0.98), the unfeedable cases have much higher maximum strains. This is because the percolated solid grains connect one side of the domain to the other, allowing for significant solid grain deformation

Microstructure model	Fraction solid	Average pressure drop (kPa)	Maximum bulk strain ($\times 10^{-3}$)
Feedable globular B206	0.85	0.07	8.0
	0.90	0.93	2.5
	0.95	1.22	0.8
	0.98	1.84	0.5
Unfeedable globular B206	0.85	31.54	6.0
	0.90	9.41	1.1
	0.95	268.84	2.3
	0.98	103.99	6.6

Table 6.7 Comparison of the feedable and unfeedable globular B206 microstructure model results

Unfeedable Globular and Dendritic B206 Microstructure Model Comparison: Table 6.8 shows unfeedable globular and dendritic B206 microstructure model results including the average pressure drop in the domains, the maximum bulk strain (ϵ_{\max}), and the calculated bulk semi-solid yield stress.

Microstructure model	Fraction solid	Yield stress (MPa)	Average pressure drop (kPa)	Maximum bulk strain ($\times 10^{-3}$)
Unfeedable globular B206	0.85	0.49	31.54	6.0
	0.90	0.63	9.41	1.0
	0.95	2.52	268.84	2.3
	0.98	10.47	103.99	6.6
Unfeedable dendritic B206	0.85	0.79	1233.24	0.01
	0.90	4.31	208.42	0.5
	0.95	7.45	490.21	0.11
	0.98	15.21	199.43	1.8

Table 6.8 Comparison of the unfeedable globular and dendritic B206 microstructure model results

The microstructure model simulations predict higher pressure drops to occur at all fraction solids, especially at $f_s=0.85$, for the unfeedable dendritic B206 in comparison with the unfeedable globular B206. The maximum bulk strain of the dendritic microstructure was shown to be lower than the maximum bulk strain of the globular microstructure, specifically at $f_s=0.95$ and $f_s=0.98$. When the deformation is applied, the B206 globular grains move easily past one another, causing the pressure drop to remain small which results in larger bulk strain. In contrast, when deformation is applied on the B206 dendrite microstructures, the liquid is trapped between dendrite arms as shown in Figure 6.31 which prevents the liquid from flowing freely, thus increasing the pressure drop. For both microstructures, the semi-solid yield stress is seen to increase with increasing fraction solid, although the values for the dendritic cases are higher than the values for the globular cases. For example, the globular and the dendritic structure at fraction solid of 0.95, have different yield stresses (2.52 and 7.45 MPa, respectively) in spite of having the same input material properties (refer to Figure 5.9). This confirms the fact that in the globular structure, due to the large and elongated liquid pockets, a significant amount of applied deformation is compensated by liquid flow and redistribution. But with dendritic microstructure, since the liquid pockets are smaller and more evenly distributed, stress is developed over a larger area of the solid. Some experimental research, such as [88], showed that a dendritic semi-solid can sustain higher stress values in comparison with a globular structure.

Unfeedable Dendritic B206 and A356 Microstructure Model Comparison: Table 6.9

compares the unfeedable dendritic B206 and A356 microstructure model results. The pressure drop values for A356 cases are lower than the pressure drop values for the unfeedable dendritic B206 cases. This is related to the shape and size of the liquid channels in dendritic B206 which are quite a bit different than in A356. In the case of dendritic B206, as shown in Figure 6.31 the liquid channel shape is irregular and the liquid pockets are smaller and more isolated due to the existence of entangled dendrites branches. However, in the case of A356, the dendritic arms of the primary phase are covered with spherical eutectic parts which change the liquid channel shape from irregular to smooth. The influence of the liquid channel shape on the pressure drop has been studied by several researchers [89, 90]. It was shown that by changing the shape of the liquid channel from smooth edges to irregular shapes with many branches, pressure drop increases. In a study by Khajeh [91], the geometry of liquid channels undergoes a transition from dendritic to globular during the growth of eutectic grains. This creates smoother liquid channels and more elongated liquid pockets, especially at low fraction solids, as shown in Figure 6.36. As a result, fluid flow and permeability would be improved because of the formation of eutectic microconstituent. This previous finding is reinforced by the present microstructure model simulations. In terms of the calculated yield stress, it can be seen that B206 has a higher yield stress at all fraction solids due to the higher input yield stress of the solid grains, the input material properties are presented in Figure 5.9.

microstructure model	Fraction solid	Yield stress (MPa)	Average pressure drop (kPa)	Maximum bulk strain ($\times 10^{-3}$)
Unfeedable dendritic B206	0.85	0.79	1233.24	0.01
	0.90	4.31	208.42	0.5
	0.95	7.45	490.21	0.11
	0.98	15.21	199.43	1.8
Unfeedable A356	0.85	0.48	104.79	0.29
	0.90	1.88	50.92	0.55
	0.95	4.42	70.54	0.38
	0.98	8.41	29.33	0.23

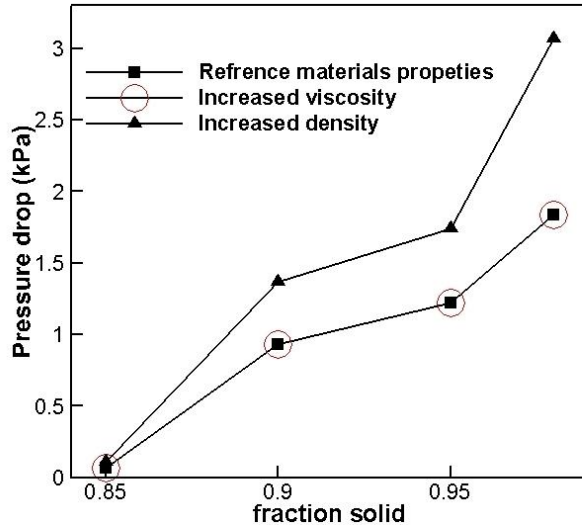
Table 6.9 Comparison of the unfeedable dendritic B206 and A356 microstructure model results

In summary, the different microstructure model simulations results were compared and contrasted in this section. It was shown that the feedable domain can sustain larger deformations and the pressure drop is quite a bit smaller as compared to the unfeedable domain. Changing the microstructure from globular to dendritic was shown to significantly increase pressure drop. The formation of the eutectic was demonstrated to be effective in decreasing the pressure drop by changing the shape of the micro liquid channels. Thus, hot tearing susceptibility would be enhanced in materials having dendritic microstructure and limited eutectic fraction.

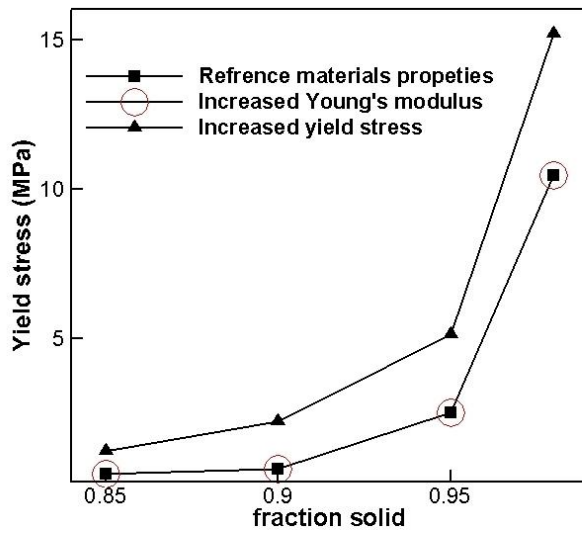
Model Sensitivity: In this section, the sensitivity of the model to input material properties is discussed. The feedable microstructure model was used to characterize the effect of liquid properties such as viscosity and density on the predicted semi-solid pressure drop. The unfeedable globular B206 microstructure model was used to characterize the effect of the solid grain material properties, Young's modulus, and yield stress, on the predicted semi-solid yield stress. The approach is to vary each property individually in order to assess their effect on the semi-solid pressure drop and yield stress at different fraction solids.

First, the feedable globular B206 microstructure model was considered as a reference. The input viscosity and density were increased by 50% from the baseline values. Second, the unfeedable globular B206 microstructure model was considered as a reference. The input Young's modulus and yield stress were then increased by 50% from the baseline values.

The results of this sensitivity analysis are shown in Figures 6.41 (a) and (b), respectively. As can be seen in Figure 6.41 (a) the semi-solid pressure drop did not change with the viscosity but did change with the input density. It can also be seen in Figure 6.41 (b) that the semi-solid yield stress did not change with changing Young's modulus, but did change with an increase in the input yield stress. For both the feedable and unfeedable cases, the effect of the input material properties is more significant at higher solid fractions, such as 0.98 and 0.95, in comparison with low fraction solids such as 0.85. This is because of the differences in fluid flow behaviour as previously discussed.



(a)

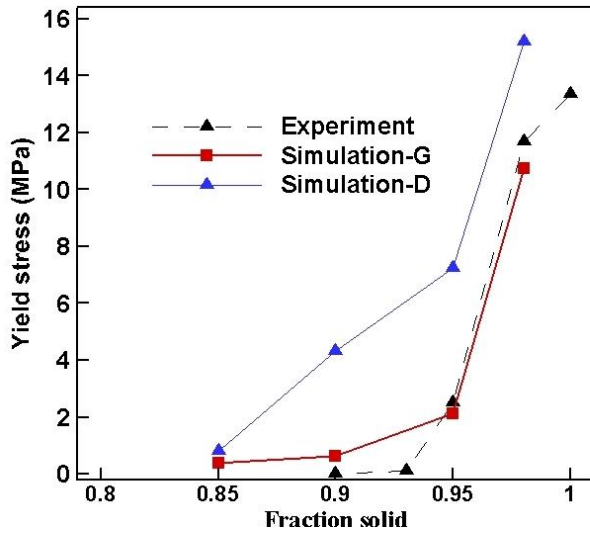


(b)

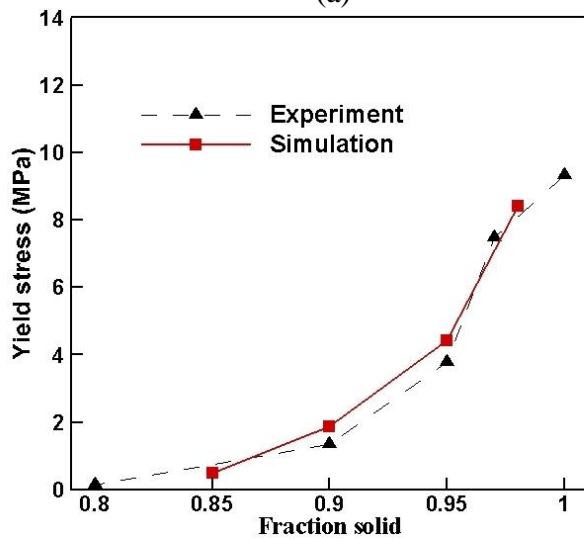
Figure 6.41 (a) Feedable globular B206 microstructure model and (b) Unfeedable globular B206 microstructure model sensitivity to the input yield stress and viscosity

Model Verification and Comparison with the Published Data: In order to verify the semi-solid multi-physics meso-scale model, the model predictions have been compared to experimentally obtained semi-solid yield stress data for B206 and A356 from the current work as well as numerically obtained semi-solid yield-stress and pressure drop from previously published data. To examine this data, unfeedable globular and dendritic

microstructure model results at four different fraction solids, corresponding to $f_s = 0.85, 0.90, 0.95$ and 0.98 , were conducted and compared to experimental data taken from the middle of the wedge. The results are shown in Figures 6.42 (a) and (b). As discussed in section 6.1.1, the B206 microstructure is globular so equiaxed-globular microstructure model results, shown as simulation-G, were plotted versus fraction solid and compared with the experimental results. As can be seen, there is good agreement between the simulation results and the experimental data. The dendritic microstructure model results (simulation-D) are also presented for comparison. A356 microstructure model results are shown and compared with the experimental data in Figure 6.42 (b). It can be seen that there is also good agreement with experimental data and the simulation results for this case.



(a)



(b)

Figure 6.42 Comparison of the model results with experiments for a) B206 and b) A356

Several researchers have numerically studied a partially solidified semi-solid behavior of Al alloys during the tensile test and during solidification (e.g. [92, 93, 66, 68]). Although there is similar work, the effects of microstructure type and eutectic constitute on semi-solid tensile properties of a partially re-melted Al alloys by using a commercial software have not been previously studied.

In the research presented by Sistaninia et. al [66], the mechanical behavior of partially solidified Al–Cu alloys was simulated. They proposed a coupled hydromechanical granular model for equiaxed globular grains. They showed that in a feedable domain the maximum pressure drop at $f_s = 0.98$ and strain rate of 0.002 s^{-1} is below 5 kPa which is very low and does not affect the solid grains deformation. The current study also shows that in the feedable domain by increasing the fraction solid from 0.80 to 0.98, at a strain rate of 0.001 s^{-1} the pressure drop increases from 0.07 to 1.84 kPa. The findings of the current study are in a good agreement with Sistaninia's work. They also studied the fluid flow and mechanical behaviour of an unfeedable solidifying domain as well. The comparison between their findings and the current study for a globular domain has been shown in Figure 6.43.

It can be seen that the results obtained from the current study and Sistaninia's model exhibit similar trends. The presented model goes beyond the past work by extending the fraction solid range and considering the effect of the microstructure on the response of the semi-solid material to an applied displacement. It also observed that at all fraction solid the current model calculated higher yield stress. The main reason is that the alloy compositions are different and there is a discrepancy in fraction solid.

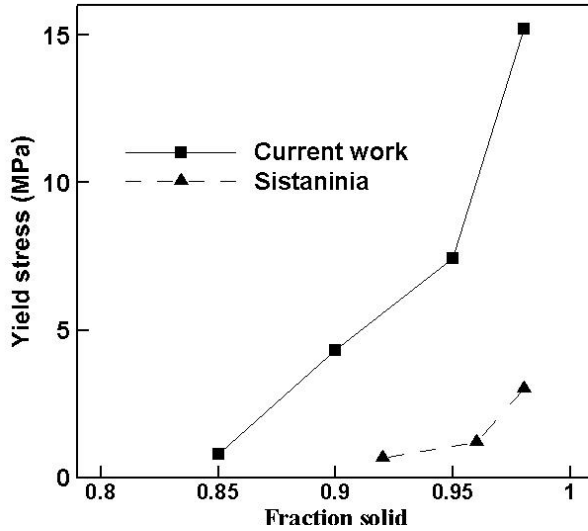


Figure 6.43 Comparison of semi-solid yield stress obtained from the unfeedable globular microstructure model and calculated by Sistaninia [66]

6.2.4 Numerically-based Assessment of the Hot Tearing Sensitivity

Since the primary goal of this study was to compare and contrast the hot tearing tendency of two commercial foundry alloys, the new numerical results, are used in this section to predict the hot tearing tendency of the mentioned alloys. In order to relate the microstructure model predictions to hot tearing, a criterion for this defect formation is needed. Taking into account the contact between the liquid and atmosphere at the surface of a casting or a semi-solid tensile test sample, the criterion can be established from the overpressure required to overcome capillary forces between the liquid and surrounding solid surfaces [9]. The Young-Laplace equation describes the force balance for the mentioned situation:

$$p_a - p_l = \frac{\lambda \cos \theta}{h} \quad (6.2)$$

where p_a and p_l are the atmospheric and liquid pressures, respectively. λ is the surface tension at the liquid-void interface and θ is the dihedral angle. Hot tearing was assumed to

initiate when the liquid pressure follows the below equation [9]. Following Sistaninia et al. [9], the term $\lambda \cos\theta$ was assumed to be $\sim 2 \text{ Jm}^{-2}$.

$$p_l < p_a - \frac{\lambda \cos\theta}{h} \quad (6.3)$$

It was assumed that hot tearing most-likely occurs at fraction solids of 0.90 and 0.95. Table 6.10 shows the average liquid channel average thicknesses and the critical pressure for these fraction solids based on Equation 6.3.

Fraction solid	h (μm)	p_l (kPa)
0.90	10	200
0.95	5	400

Table 6.10 Average liquid channel size and critical liquid pressure drop at different fraction solids

microstructure model	Fraction solid	Average pressure drop at $\varepsilon=0.5 \times 10^{-3}$ (kPa)	Average pressure drop at $\varepsilon=\varepsilon_{\max}$ (kPa)	Hot tearing initiation
Feedable	0.90	0.84	0.93	N
	0.95	0.46	1.22	N
Unfeedable globular B206	0.90	4.78	9.41	N
	0.95	1.69	268.84	N
Unfeedable dendritic B206	0.90	8.53	208.42	Y
	0.95	100.27	490.21	Y
Unfeedable A356	0.90	34.66	50.92	N
	0.95	46.12	70.54	N

Table 6.11 Numerically obtained pressure drop for different microstructure model at different fraction solids

Table 6.11 shows average pressure drop at $\varepsilon=0.5 \times 10^{-3}$ and $\varepsilon=\varepsilon_{\max}$, for fraction solids of 0.90 and 0.95 calculated from the microstructure model simulations. This average pressure is then compared with the critical pressure drop values given in Table 6.10; the initiation of hot tearing is indicated with a “Y” and “N” based on this criterion. As shown in Table 6.11 the average pressure drop in the feedable simulations, the unfeedable globular B206

simulations, and the unfeedable A356 simulations is seen to be smaller than the critical pressure drop, so it is expected that hot tears would be unlikely to initiate in these combinations of microstructures and liquid feedability. However, hot tearing would initiate at both fraction solids of the dendritic B206 microstructure model. As a result, the dendritic B206 would be expected to be considerably more susceptible to hot tearing.

In summary, the different microstructure models simulations results were compared and contrasted in this section. It was shown that in the feedable domain the pressure drop as a result of the deformation is smaller than the unfadeable domain. However, for both cases the pressure drop is smaller than the critical pressure drop, so hot tearing does not occur. Changing the microstructure from globular to dendritic was shown to significantly increase hot tearing susceptibility. The formation of the eutectic was demonstrated to be effective in decreasing the pressure drop by changing the shape of the micro liquid channels, which indicates lower hot tearing susceptibility. Thus, hot tearing susceptibility would be enhanced in materials having dendritic microstructure and limited eutectic fraction.

6.3 Summary

In this chapter, the experimental and multi-physics meso-scale simulation results characterizing the constitutive behaviour of B206 and A356 alloys in the semi-solid state were presented, and discussed with reference to the hot tearing defect. First, the experimental results from the microstructure analysis along with thermo-mechanical tests analysis were shown. The results showed that semi-solid tensile properties of both alloys are microstructure feature size dependent. Decreasing the grain size/SDAS is shown to improve semi-solid tensile properties especially at high fraction solids such as $f_s=0.95$ and $f_s=0.99$. The effect of microstructure features size is more dominant in B206 than A356. By decreasing the fraction solid yield stress and ductility of the semi-solid B206 and A356 decrease. The decrease in the yield stress and ductility with temperature is more uniform in the A356 alloy; however, there is a sudden drop of the mechanical properties of B206 samples at $f_s=0.93$. Then, multi-physics simulations were performed on a simple geometry domain (exploratory) as well as microstructure domains to investigate semi-solid deformation. It was demonstrated that the combination of Abaqus/Standard and Abaqus/CFD can be used to couple solid deformation and liquid flow and determine the respond of the semi-solid to the applied deformation. It was shown that the meso-scale model adequately described the pressure drop and semi-solid deformation behaviour of foundry alloys. The important finding of the meso-scale model was the dependency of the semi-solid yield stress on the domain feedability, microstructure type, and eutectic formation. The pressure drop in the liquid channels of a feedable domain predicted to be lower than the pressure drop in the unfeedable domain. Globular and dendritic B206 showed different semi-solid yield stress at each fraction solid even though the input material properties were the same. It was shown that the existence of eutectic in the

microstructure of an alloy with relatively high amount of eutectic, such as A356, decreases pressure drop as a result of creating a smooth liquid/solid interface. The pressure drop in a dendritic domain was reported to be very high due to the highly entangled dendrite branches and isolated liquid pockets. It was shown that as long as the pressure drop and deformation are small, the hot tearing will not occur.

Chapter 7: Conclusions and Future Work

This Ph.D. research has focused on characterizing the semi-solid constitutive behaviour of two aluminum foundry alloys, B206 and A356, with the goal of understanding and comparing their hot tearing sensitivity from experimental and numerical perspectives. Two main studies were carried out. First, using a Gleeble thermo-mechanical simulator, the effects of temperature, grain size/SDAS, and micro-segregation on semi-solid yield stress and ductility were quantified. For these experiments, wedge castings were produced having known and consistent microstructure. Second, a multi-physics meso-scale model, named as microstructure model, was developed to simulate a material's response to an applied deformation in the semi-solid state at high fraction solid. Using feedable and unfeedable microstructure models, the effect of feeding of the semi-solid pressure drop was studied. Unfeedable domains with different microstructures were created and effect of the microstructure on the semi-solid behaviour (liquid pressure drop and semi-solid, maximum bulk strain and yield stress) was investigated. The new model is capable of accommodating a semi-solid's nonlinear stress/strain response by coupling fluid flow and solid-state deformation. The model was used to simulate temperature/fraction solid and microstructure-dependent semi-solid behaviour. This model was validated against the experimental measurements and previously published data, showing a good agreement. The overall results of the experimental and numerical analysis demonstrate that B206 is more susceptible to hot tearing. However, it should be noted that hot tearing could also occur in A356 if the feeding is limited or the deformation is large.

7.1 Conclusions

The main findings and achievements of the current thesis are as follows:

Experimental Findings

1. The semi-solid tensile properties (500-570°C) of B206 and A356 were characterized. It was indicated that, as expected, by increasing temperature, decreasing the fraction solid, B206 and A356 yield stress and ductility both decrease. It was shown that at relatively high fraction solid ($f_s=0.95-1$), B206 is stronger than A356. However, at lower fraction solids ($f_s<0.95$), A356 has been shown to have higher yield stress.

2. The effects of SDAS on semi-solid yield stress and ductility of both alloys were investigated and it was shown that in general smaller SDAS improves tensile properties. Such effect is more significant in B206 alloy than A356, especially at high fraction solids, ($f_s=0.95-1$).

3. Decreasing the microstructure size - i.e. B206 grain size - is shown to be beneficial in improving hot tearing resistance. In practice, this could be achieved by using a grain refiner or by increasing the cooling rate. The addition of a grain refiner would be the preferred options as it would avoid the potential for higher thermal stresses associated with higher cooling rates.

4. It was found that a looped thermocouple method is efficient for carrying out the test at elevated temperatures (lower fraction solids).

Numerical Findings

1. A new meso-scale multi-physics model was developed to study the effects of feeding, microstructure, and eutectic on the semi-solid deformation behavior of B206 and

A356 aluminum alloys. The model was capable of predicting, pressure drop, semi-solid bulk strain, and yield stress.

2. It was demonstrated that in an externally feedable microstructure model, the globular microstructure can sustain large deformation as a result of small pressure drop. Pressure drop was shown to increase by increasing the fraction solid.

3. The semi-solid deformation and pressure drop in unfeedable microstructure domains are shown to be strongly dependent on the type of the microstructure (globular and dendritic) and eutectic formation. Changing the microstructure from globular to dendritic was shown to increase yield stress and pressure drop.

4. The existence of the eutectic was shown to improve fluid flow and decrease the pressure drop.

5. The pressure drop was related to the hot tearing formation and it was concluded that a dendritic B206 microstructure is more prone to hot tearing than a globular B206 one, it was also indicated that the eutectic formation in A356 improves hot tearing resistance.

6. The model results were compared with the experimentally obtained data and previously published data, it was shown that there is a good agreement between the model result and experimental data and previous work

7.2 Future Work

The microstructure and semi-solid constitutive behaviour of two commercial alloys were studied using experimental and simulation approaches. It is accepted that this study has some limitations with respect to both experiments and simulations. Follow-on work is recommended in the several areas:

1. Some improvements can be applied to the experiments to better understand the relative contributions of the micro-segregation and SDAS on the semi-solid behaviour of aluminum alloys. The author suggests obtaining a larger range of SDAS and studying the effect of cooling rate on the micro-segregation.
2. To better reveal grain boundaries in the B206 alloy, the microstructure samples should first be anodizing and then examined through a polarizing filter.
3. The effect of strain rate on semi-solid behaviour should be considered and analyzed. One of the shortcomings of studying the effect of strain rate was the limited number of samples and focusing on the effect of SDAS and micro-segregation on semi-solid yield stress and ductility of two alloys.
4. The model assumes that the dendritic grains are fully solids. For future work, the effect of the interdendritic liquid on the semi-solid deformation could be considered.
4. The eutectic grains was assumed to be spherical, Further investigations are required to present an expression for the case of non-spherical eutectic grains.
6. Due to the nature of semi-solid materials which is 3-D, it would be better to model 3-D microstructure domains. One drawback of using 3-D model is more simulation time, taking into account that we got satisfactory results using a 2-D model.

Bibliography

- [1] J. G. Kaufman, E. L. Rooy, "Aluminum Alloy Castings: Properties, Processes, and Applications," 1931.
- [2] J. Campbell, R. A. Harding, "The Feeding of Castings," 1994.
- [3] D. G. Eskin, *Physical Metallurgy of Direct Chill Casting of Aluminum Alloys*, CRC press, 2008.
- [4] I. Farup, "Thermally Induced Deformations and Hot Tearing During Direct Chill Casting of Aluminium," *PROSMAT*, 2000.
- [5] D. G. Eskin, Suyitno, L. Katgerman, "Mechanical Properties in the Semi-solid State and Hot Tearing of Aluminium Alloys," *Materials Science*, vol. 49, pp. 629-711, 2004.
- [6] F. D'Elia, "A Study on Grain Refinement and Hot Tearing in Permanent Mold Cast Aluminum Alloys," Ryerson University, 2009.
- [7] M. Mathier, A. Jacot, M. Rappaz, "Coalescence of Equiaxed Grains During Solidification," *Modelling and Simulation in Materials Science and Engineering*, vol. 12, pp. 479-490, 2004.
- [8] A. B. Phillion, S. L. Cockcroft, P. D. Lee, "A New Methodology for Measurement of Semi-solid Constitutive Behavior and its Application to Examination of As-cast Porosity and Hot Tearing in Aluminum Alloys," *Materials Science and Engineering A*, vol. 491, pp. 237-247, 2008.
- [9] M. Sistaninia, J. M. Drezet, A. B. Phillion, M. Rappaz, "Prediction of Hot Tear Formation in Vertical DC Casting of Aluminum Billets Using a Granular Approach," *Journal of Materials*, vol. 65, pp. 1131-1137, 2013.
- [10] M. A. Suarez, I. Figueroa, A. Cruz, A. Hernandez, J. F. Chavez, "Study of the Al-Si-X System by Different Cooling Rates and Heat Treatment," *Materials Research*, vol. 15, pp. 763-769, 2012.

- [11] L. Y. Zhang, Y. H. Jiang, Z. Ma, S. F. Shan, "Effect of Cooling Rate on Solidified Microstructure and Mechanical Properties of Aluminium-A356 Alloy," *Journal of Materials Processing Technology*, vol. 207, pp. 107-111, 2008.
- [12] T. G. Nguyen, D. Favier, M. Su, "Theoretical and Experimental Study of the Isothermal Mechanical Behaviour of Alloys in the Semi-solid," *International Journal of Plasticity*, vol. 10, pp. 663-693, 1994.
- [13] S. Shao-chun, Y. Bo, L. Man-ping, "Effects of Moulding Sands and Wall Thickness on Microstructure and Mechanical Properties of Sr-modified A356 Aluminum Casting Alloy," *Trans. Nonferrous Met. Soc. China*, vol. 22, pp. 1884-1890, 2012.
- [14] J. Talamantes-Silva, M. A. Talamantes-Silva, A. Rodriguez, "Effect of Solidification Rate and Heat Treating on the Microstructure and Mechanical Behavior of an Aluminum-copper Alloy," *Metallurgical and Materials Transaction B*, vol. 39, pp. 911-919, 2008.
- [15] N. Haghdadi, A. B. Phillion, D. M. Maijer, "Microstructure Characterization and Thermal Analysis of Aluminum Alloy B206 During Solidification," *Metallurgical and Materials Transactions A*, vol. 46, pp. 2073-2081, 2015.
- [16] A. B. Phillion, "Hot Tearing and Constitutive Behaviour of Semi-solid Aluminum Alloys," The University of British Columbia, 2007.
- [17] V. Mathier, P. D. Grasso, M. Rappaz, "A New Tensile Test for Aluminum Alloys in the Mushy State: Experimental Method and Numerical Modeling," *Metallurgical and Materials Transactions A*, vol. 39, pp. 1399-1409, 2008.
- [18] I. Farupa, J.-M Drezet, M. Rappaz, "In Situ Observation of Hot Tearing Formation in Succinonitrile-acetone," *Acta Materialia*, vol. 49, no. 7, pp. 1261-1269, 2001.
- [19] A. K. Dahle, Y. C. Lee, M. D. Nave, P. L. Schaer, D. H. StJohn, "Development of the As-cast Microstructure in Magnesium-aluminium Alloys," *Journal of Light Metals*, pp. 61-72, 2001.

- [20] C. Monroe, C. Beckermann, "Development of a Hot Tear Indicator for Steel Castings," in *Defect Formation, Detection, and Elimination During Casting, Welding, and Solidification*, 2005.
- [21] D. G. Eskin, L. Katgerman, "A Quest for a New Hot Tearing Criterion," *Metallurgical and Materials Transactions A*, vol. 38, pp. 1511-1519, 2007.
- [22] J. Guo, J. Z. Zhu, "Prediction of Hot Tearing During Alloy Solidification," in *Proceedings of the 5th Decennial International Conference on Solidification Processing*, Sheffield, 2007.
- [23] A. R. E. Singer, P. H. Jennings, "Hot-Shortness of the Aluminium-1043 Silicon Alloys of Commercial Purity," *Journal of the Institute of Metals*, vol. 72, pp. 197-211, 1946.
- [24] W. S. Pellini, "Strain Theory of Hot-tearing," *Foundry*, vol. 80, pp. 125-199, 1952.
- [25] D. Warrington, D. G. McCartney, "Hot cracking in Aluminium Alloys 7050 and 7010- a Comparative Study," *Cast Metals*, vol. 3, pp. 202-208, 1991.
- [26] Y. F. Hunt, J. D. Guven, "Hot Tearing in Aluminum Copper Alloys," *Cast Metals*, vol. 1, pp. 104-111, 1988.
- [27] M. O. Pekguleryuz, X. Li, C. A. Aliravci, "In-Situ Investigation of Hot Tearing in Aluminum Alloy AA1050 via Acoustic Emission and Cooling Curve Analysis," *Metallurgical and Materials Transactions A*, pp. 129-138, 2009.
- [28] M. Braccini, M. Suéry, C. Laguerre, M. Stucky, "Influence of Grain Refinement on Hot Tearing in Aluminium-copper Alloys Used in Foundry industries," *Revue de Métallurgie*, vol. 100, pp. 157-164, 2003.
- [29] M. Rappaz, J. M. Drezet, M. Gremaud, "A New Hot-Tearing Criterion," *Metallurgical and Materials Transactions A*, vol. 30, pp. 449-455, 1999.
- [30] T. W. Clyne, G. J. Davies, "The Influence of Composition on Solidification Cracking Susceptibility in Binary Alloy Systems," *The British Foundryman*, vol. 74, pp. 65-73, 1981.

- [31] H. F. Bishop, C. G. Ackerlind, W. S. Pellin, "Investigation of Metallurgical and Mechanical Effects in the Development of Hot Tearing," *Transaction of American Foundry Society*, vol. 65, pp. 247-258, 1957.
- [32] S. Li, K. Sadayappan, D. Apelian, "Characterisation of Hot tearing in Al-cast Alloys: Methodology and Procedures," *International Journal of Cast Metals Research*, vol. 24, pp. 354-359, 2011.
- [33] S. Li, "Hot Tearing in Cast Aluminum Alloys," Worcester Polytechnic Institute, 2010.
- [34] J. B. Sutton, "Solidification Behavior and Hot Cracking Susceptibility of High Manganese Steel Weld Metals," The Ohio State University, 2013.
- [35] C. Puncreobutr, P. D. Lee, K. M. Kareh, T. Connolley, J. L. Fife, A. B. Phillion, "Influence of Fe-rich Intermetallics on Solidification Defects in Al-Si-Cu Alloys," *Acta Materialia*, vol. 68, pp. 42-51, 2014.
- [36] I. C. Lippold, E. F. Nippes, W. F. Savage, "An Investigation of Hot Cracking in 5083-O Aluminum Alloy Weldments," *Welding Research Supplements*, pp. 171-178, 1977.
- [37] V. Shankar, T. P. S. Gill, S. L. Mannan, S. Sundaresan, "Solidification Cracking in Austenitic Stainless Steel Welds," *Sadhana*, vol. 28, pp. 359-382, 2003.
- [38] B. Magnin, L. Maenner, L. Katgerman, S. Engler, "Ductility and Rheology of an Al-4.5Cu Alloy from Room Temperature to Coherency Temperature," *Materials Science Forum*, Vols. 1209-1214, pp. 217-222, 1996.
- [39] M. J. Roy, D. M. Maijer, L. Dancoine, "Constitutive Behavior of As-cast A356," *Materials Science and Engineering A*, vol. 548, pp. 195-205, 2012.
- [40] J. Drezet, G. Eggeler, "High Apparent Creep Activation-Energies in Mushy Zone Microstructures," *Scripta Metallurgica Et Materialia*, vol. 31, pp. 757-762, 1994.
- [41] W. M. Haften, W. H. Kool, L. Katgerman, "Tensile Behaviour of Semi-solid Industrial Aluminum Alloys AA3104 and AA5182," *Materials Science and Engineering A*, vol. 336, pp. 1-6, 2002.
- [42] C. L. Martin, M. Braccini, M. Suery, "Rheological Behavior of the Mushy Zone at Small Strains," *Materials Science and Engineering A*, vol. 325, pp. 292-301, 2002.

- [43] A. R. E. Singer, S. A. Cottrell, "Properties of the Aluminium-silicon Alloys at Temperatures in the Region of the Solidus," *Institute of Metals*, vol. 73, pp. 33-54, 1947.
- [44] A. B. Phillion, S. Thompson, S. L. Cockcroft, M. A. Wells, "Tensile Properties of As-cast Aluminum Alloys AA3104, AA6111 and CA31218 at Above Solidus Temperatures," *Materials Science and Engineering A*, vol. 497, pp. 124-130, 2008.
- [45] D. Fabre`gue, A. Deschamps, M. Sue`ry, W. J. Poole, "Rheological Behavior of Al-Mg-Si-Cu Alloys in the Mushy State Obtained by Partial Remelting and Partial Solidification at High Cooling Rate," *Metallurgical and Materials Transactions*, vol. 37A, pp. 1459-1467, 2006.
- [46] W. M. Haften, W. H. Kool, L. Katgerman, "Tensile Behaviour of Semi-solid Industrial Aluminum Alloys AA3104 and AA5182," *Materials Science and Engineering A*, vol. 336, pp. 1-6, 2002.
- [47] L. J. Colley, M. A. Wells, D. M. Maijer, "Tensile Properties of As-cast Aluminum Alloy AA5182 Close to the Solidus Temperature," *Materials Science and Engineering A*, vol. 386, pp. 140-148, 2004.
- [48] D. Fabre`gue, A. Deschamps, M. Suery, J. M. Drezet, "Non-isothermal Tensile Tests During Solidification of Al-Mg-Si-Cu Alloys: Mechanical Properties in Relation to the Phenomenon of Hot Tearing," *Acta Materialia*, vol. 54, pp. 5209-5220, 2006.
- [49] P. Ackermann, W. Kurz, "In Situ Tensile Testing of Solidifying Aluminium and Al-Mg Shells," *Materials Science and Engineering*, vol. 75, pp. 79-86, 1985.
- [50] A. K. Dahle, S. Instone, T. Sumitomo, "Relationship Between Tensile and Shear Strengths of the Mushy Zone in Solidifying Aluminum Alloys," *Metallurgical and Materials Transactions A*, vol. 34A, pp. 105-113, 2003.
- [51] J. B. Mitchell, S. L. Cockcroft, D. Viano, C. Davidson, D. Stjoh, "Determination of Strain during Hot Tearing by Image Correlation," *Metallurgical and Materials Transactions A*, vol. 38, pp. 2503-2512, 2007.

- [52] T. G. Nguyen, D. Favier, M. Su, "Theoretical and Experimental Study of the Isothermal Mechanical Behaviour of Alloys in the Semi-solid," *International Journal of Plasticity*, vol. 10, pp. 663-693, 1994.
- [53] S. Benke, S. Dziallach, G. Laschet, U. Prah, W. Bleck, "Modeling of the Uniaxial Tensile and Compression Behavior of Semi-solid A356 Alloys," *Computational Materials Science*, vol. 45, pp. 633-637, 2009.
- [54] A. Bolouri, X. G. Chen, "Tensile Deformation Behavior of Al-Cu 206 Cast Alloys Near the Solidus Temperature," *Materials Science Forum*, vol. 877, pp. 90-96, 2017.
- [55] M. C. Flemings, G. Nereo, "Macro-segregation: Part I," *Transactions of the Metallurgical Society of AIME*, vol. 239, pp. 1449-1461, 1967.
- [56] S. Vernède, M. Rappaz, "A simple and Efficient Model for Mesoscale Solidification Simulation," *Acta Materialia*, vol. 55, pp. 1703-1710, 2007.
- [57] J. A. Ferrez, "Dynamic Triangulations for Efficient 3D Simulation of Granular Materials," EPFL, 2001.
- [58] C. Martin, D. Bouvard, G. Delette, "Discrete Element Simulations of the Compaction of Aggregated Ceramic Powders," *Journal of American Ceramic Society*, vol. 89, pp. 3379-3387, 2006.
- [59] W. O. Dijkstra, C. Vuik, L. Katgerman, "Network Model of Fluid Flow in Semi-solid Aluminum Alloys," *Computational Materials Science*, vol. 38, pp. 67-74, 2006.
- [60] D. J. Lahaie, M. Bouchard, "Physical Modeling of the Deformation Mechanism of Semisolid Bodies and a Mechanical Criterion for Hot Tearing," *Metallurgical & Materials Transaction B*, vol. 32, pp. 697-705, 2001.
- [61] S. Vernède, P. Jarry, M. Rappaz, "A Granular Model of Equiaxed Mushy Zones: Formation of a Coherent Solid and Localization of Feeding," *Acta Materialia*, vol. 54, pp. 4023-4034, 2006.
- [62] L. Yuan, C. O'Sullivan, C. M. Gourlay, "Exploring Dendrite Coherency with the Discrete Element Method," *Acta Materialia*, vol. 60, pp. 1334-1345, 2012.

- [63] A. B. Phillion, P. D. Lee, E. Maire, And S. L. Cockcroft, "Quantitative Assessment of Deformation-induced Damage in a Semisolid ALuminum Alloy via X-ray Microtomography," *Metallurgical and Materials Transactions A*, vol. 39, pp. 2459-2469, 2008.
- [64] K. M. Kareh, P. D. Lee, R. C. Atwood, T. Connolley, C. M. Gourlay, "Revealing the Micromechanisms Behind Semi-solid metal Deformation with Time-resolved X-ray Tomography," *Nature Communications*, 2014.
- [65] J. F. Zaragoci, L. Silva, M. Bellet, C. A. Gandin, "Numerical Tensile Test on a Mushy Zone Sample," in *IOP Conference Series: Materials Science and Engineering*, 2012.
- [66] M. Sistaninia, A. B. Phillion, J. M. Drezet, M. Rappaz, "A 3-D Coupled Hydromechanical Granular Model for Simulating the Constitutive Behavior of Metallic Alloys During Solidification," *Acta Materialia*, vol. 60, pp. 6793-6803, 2012.
- [67] M. Sistaninia, A. B. Phillion, J.-M. Drezet, M. Rappaz, "Simulation of Semi-Solid Material Mechanical Behavior Using a Combined Discrete/Finite Element Method," *Metallurgical and Materials Transactions A*, vol. 42, pp. 239-248, 2011.
- [68] A. B. Phillion, S. L. Cockcroft, P. D. Lee, "A Three-phase Simulation of the Effect of Microstructural Features on Semi-solid Tensile Deformation," *Acta Materialia*, vol. 56, pp. 4328-4338, 2008.
- [69] A. T. Dinsdale, P. N. Quested, "The Viscosity of Aluminium and Its Alloys—A Review of Data and Models," *Journal of Materials Science*, vol. 39, pp. 7221-7228, 2004.
- [70] A.B. Phillion, S.L. Cockcroft, P.D. Lee, "A three-phase Simulation of the Effect of Microstructural Features on Semi-solid Tensile Deformation," *Acta Materialia*, vol. 56, pp. 4328-4338, 2008.
- [71] S. Thompson, "Effect of Cooling Rate on Solidification Characteristics of Aluminum Alloys A356 and AA5182," UBC, 2003.
- [72] M. Nyg°ards, "Microstructural Finite Element Modeling of Metals," Royal Institute of Technology, 2003.

- [73] H. Bayani, "Simulation of Unconstrained Solidification of A356 Aluminum Alloy on Distribution of Micro/macro Shrinkage," *Journal of Materials Research and Technology*, vol. 3, pp. 55-70, 2014.
- [74] B. J. Yang, D. M. Stefanescu, J. Leon-Torres, "Modeling of Microstructural Evolution with Tracking of Equiaxed Grain Movement for Multicomponent Al-Si Alloy," *Metallurgical and Materials Transactions A*, vol. 32, pp. 3065-3076, 2001.
- [75] "<http://www.skirt.ugent.be/skirt/voro.html>," [Online]. 12/02/2014
- [76] S. M. Mohseni, "Constitutive Behaviour of Aluminium Alloy B206 in the As-cast and Artificially Aged Stages," UBC, 2015.
- [77] A. Bolouri, X. G. Chen, "Tensile Deformation Behavior of Al-Cu 206 Cast Alloys Near the Solidus Temperature," *Materials Science Forum*, vol. 877, pp. 90-96, 2016.
- [78] M. A. Suarez, I. Figueroa, A. Cruz, A. Hernandez, J. F. Chavez, "Study of the Al-Si-X System by Different Cooling Rates and Heat Treatment," *Materials Research*, vol. 5, pp. 763-769, 2012.
- [79] F. D'Elia, "A Study of Hot Tearing During Solidification of B206 Aluminum Alloy," Ryerson University, 2015.
- [80] M. C. Flemings, "Solidification Processing," *Metallurgical and Materials Transactions B*, pp. 2121-2134, 1974.
- [81] N. Chen, C. Luo, Y. Huo, F. Bai, Y. Zhao, X. MA, "Effect of Cu Concentration on the Semi-Solid Deformation Behavior and Microstructure of Ti-Cu Alloy Y," *Advances in Mechanical Engineering*, vol. 7, pp. 1-10, 2015.
- [82] J. T. Staley, M. Tiryakioğlu, J. Campell, "The Effect of Increased HIP Temperatures on Bifilms and Tensile Properties of A206-T71 Aluminum Castings," *Materials Science and Engineering: A*, Vols. 460-461, pp. 324-334, 2007.
- [83] M. Ganesan, D. Dye, P. D. Lee, "A Technique for Characterizing Microsegregation in Multicomponent Alloys and Its Application to Single-Crystal Superalloy Castings," *Metallurgical and Materials Transactions A*, vol. 36, pp. 2191-2204, 2005.

- [84] O. Ludwig, J-M. Drezet, C. L. Martin, M. Suéry, "Rheological Behavior of Al-Cu Alloys during Solidification: Constitutive Modeling, Experimental Identification, and Numerical Study," *Metallurgical and Materials Transactions A*, vol. 36, pp. 1525-1535, 2005.
- [85] S. Benke, S. Dziallach, G. Laschet, U. Prahl, W. Bleck, "Experimental Characterization of a Semi-solid A356 Alloy During Solidification and Remelting," *International Journal of Cast Metals Research*, vol. 22, pp. 248-251, 2009.
- [86] J. Langlais, J. E. Gruzleski, "A Novel Approach to Assessing the Hot Tearing Susceptibility of Aluminum Alloys," *Materials Science Forum*, Vols. 331-337, pp. 167-172, 2000.
- [87] A. B. Phillion, S. L. Cockcroft, P. D. Lee, "Predicting the Constitutive Behavior of Semi-solids via a Direct Finite Element Simulation: Application to AA5182," *Modeling and Simulation in Materials Science and Engineering*, vol. 17, pp. 1-15, 2009.
- [88] M. N. Mohammed, M. Z. Omar, M. S. Salleh, K. S. Alhawari, P. Kapranos, "Semisolid Metal Processing Techniques For Nondendritic Feedstock Production," *Scientific World Journal*, vol. 11, pp. 1-16, 2013.
- [89] M. I. Hasana, A. A. Rageb, M. Yaghoubib, H. Homayoni, "Influence of Channel Geometry on the Performance of a Counter Flow Microchannel Heat Exchanger," *International Journal of Thermal Sciences*, vol. 48, pp. 1607-1618, 2009.
- [90] T. S. Ravigururajan , "Impact of Channel Geometry on Two-Phase Flow Heat Transfer Characteristics of Refrigerants in Microchannel Heat Exchangers," *Journal of Heat Transfer*, vol. 120, pp. 485-491, 1998.
- [91] E. Khajeh, "Permeability of Hypoeutectic Aluminum Alloys," *UBC*, 2011.
- [92] J.-L. D. M. R. A.B. Phillion, "A 3D granular model of Equiaxed-granular Solidification," *Modeling of Casting, Welding and Advanced Solidification Processes–XII, TMS (The Minerals, Metals & Materials Society)*, pp. 353-360, 2009.

- [93] S. Vernède, P. Jarry, M. Rappaz, “A granular Model of Equiaxed Mushy Zones: Formation of a Coherent Solid and Localization of Feeding.,” *Acta Materialia*, vol. 54, pp. 4023-4034, 2006.
- [94] E. Tillová, M. Chalupová, L. Hurtalová, Evolution of Phases in a Recycled Al-Si Cast Alloy During Solution Treatment, Scanning Electron Microscopy, InTech, 2012.

Appendices

Appendix A

In this section, all the results which obtained from the Gleeble tests are presented. Table A.1 and Table A.2 show Gleeble test results of the as-cast B206 and A356 samples, taken from the bottom, middle, and top of the wedges. Table A.3 and Table A.4 show Gleeble test results of the HIP B206 and A356 samples, taken from the bottom, middle, and top of the wedges. Each table includes the test conditions including the location of the samples, test temperatures, and corresponding fraction solids as well as the tests results including the yield stress and ductility. It should be noted that it was assumed that the evolution of fraction solid with temperature is independent of the cooling rate and micro-segregation.

material	Location in the wedges	Temperature (°C)	Fraction solid	Yield stress (MPa)	Ductility
B206	Bottom	500	1	15.63	0.28
		520	0.98	12.9	0.14
		540	0.95	5.23	0.01
		550	0.93	0.93	0.008
		570	0.90	0.41	0.005
	Middle	500	1	13.37	0.18
		520	0.98	11.68	0.1
		540	0.95	2.5	0.003
		550	0.93	0.1	0.001
		570	0.90	0	0
	Top	500	1	10.66	0.064
		520	0.98	9.29	0.056
		540	0.95	1.14	0.008
		550	0.93	0.67	0
		570	0.90	0	0

Table A.1 Gleeble test results of as-cast B206

Material	Location in the wedges	Temperature (°C)	Fraction solid	Yield stress (MPa)	Ductility
A356	Bottom	500	1	13.25	0.44
		520	1	11.3	0.36
		540	0.97	7.8	0.26
		550	0.95	5.0	0.13
		560	0.90	2.1	0.03
		570	0.80	0.3	0.01
	Middle	500	1	12.75	0.40
		520	1	9.33	0.32
		540	0.97	7.47	0.23
		550	0.95	3.77	0.08
		560	0.90	1.34	0.02
		570	0.80	0.15	0.01
	Top	500	1	11.25	0.43
		520	1	8.61	0.28
		540	0.97	6.99	0.25
		550	0.95	4.63	0.09
		560	0.90	1.09	0.02
		570	0.80	0.5	0.006

Table A.2 Gleeble test results of as-cast A356

Material	Location in the wedges	Temperature (°C)	Fraction solid	Yield stress (MPa)	Ductility
B206	Bottom	500	1	17.12	0.35
		520	0.98	15.13	0.25
		540	0.95	11.59	0.09
		550	0.93	3.23	0.03
		570	0.90	1.25	0.01
	Middle	500	1	18.98	0.32
		520	0.98	12.97	0.25
		540	0.95	10.45	0.02
		550	0.93	2.67	0.09
		560	0.90	1.99	0.01
	Top	500	1	16.16	0.35
		520	0.98	14.37	0.13
		540	0.95	11.49	0.01
		550	0.93	3.02	0.01
		570	0.90	1.93	0.03

Table A.3 Gleeble test results of HIP B206

Material	Location in the wedges	Temperature (°C)	Fraction solid	Yield stress (MPa)	Ductility
A356	Bottom	500	1	15.83	0.46
		520	1	13.39	0.40
		540	0.97	11.27	0.31
		550	0.95	9.88	0.15
		560	0.9	6.29	0.11
		570	0.8	3.17	0.02
	Middle	500	1	14.27	0.44
		520	1	11.59	0.29
		540	0.97	9.39	0.14
		550	0.95	8.27	0.17
		560	0.9	5.98	0.12
		570	0.8	3.76	0.08
	Top	500	1	13.97	0.42
		520	1	12.11	0.30
		540	0.97	9.73	0.14
		550	0.95	7.45	0.07
		560	0.9	6.12	0.12
		570	0.8	3.29	0.09

Table A.4 Gleeble test results of HIP A356